LEVEL II

ADA067993

# COMBUSTION NOISE PREDICTION: ENTROPY/VORTICITY EFFECTS

Warren C. Strahle
M. Muthukrishnan
Douglas H. Neale
Suresh K. Aggarwal

School of Aerospace Engineering
Georgia Institute of Technology
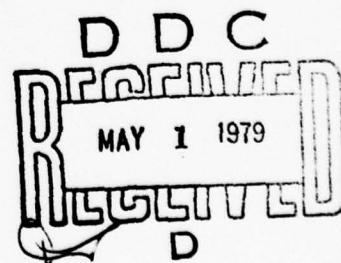Atlanta, Ga.

DDC FILE COPY.

Final Report

March 1979

DDC
RECEIVED
MAY 1 1979
D

Prepared for

## U.S. DEPARTMENT OF TRANSPORTATION
FEDERAL AVIATION ADMINISTRATION
Systems Research & Development Service
Washington, D.C. 20590

79 04 26 049

NOTICE

This document is disseminated under the sponsorship of the
Department of Transportation in the interest of information
exchange. The United States Government assumes no liability
for its contents or use thereof.

| 1. Report No. FAA-RD-79- 1 | 2. Government Accession No. | 3. Recipient's Catalog No. |
|---|---|---|
| 4. Title and Subtitle Combustion Noise Prediction:  Entropy/Vorticity Effects | | 5. Report Date March 1979 |
| | | 6. Performing Organization Code |
| 7. Author's) Warren C. Strahle, M. Muthukrishnan, Douglas H. Neale, Suresh K. Aggarwal | | 8. Performing Organization Report No. |
| 9. Performing Organization Name and Address School of Aerospace Engineering Georgia Institute of Technology Atlanta, Georgia | | 10. Work Unit No. |
| | | 11. Contract or Grant No. DOT-FA77WA-4077 |
| 12. Sponsoring Agency Name and Address U.S. Department of Transportation Federal Aviation Administration Systems Research and Development Service Washington, D.C.   20591 | | 13. Type of Report and Period Covered Final Report, Sept. 1977—Jan. 1979 |
| | | 14. Sponsoring Agency Code ARD-550 |

15. Supplementary Notes

16. Abstract

An experimental and theoretical program was conducted to see if entropy noise and vorticity-nozzle interaction noise, as well as direct combustion noise, could be isolated in gas turbine combustor tests.  Moreover, a unified correlation, with a rational theoretical basis, was developed for direct noise from combustor rig tests.  It was found that  (a) vorticity noise was at least as large as combustion noise,  (b) entropy noise is minor but is large only at low frequency, (c) all noise sources are coherent with each other over various frequency ranges, (d) with a choked nozzle termination the noise is higher frequency ($\approx$2000 Hz) than heretofore believed,  (e) some other unexplained noise source contaminated the results at low frequency and  (f) the diffuser used caused additional coherent noise, probably through the vorticity source.  A method for accounting for the vorticity and entropy sources in combustor rig tests was indicated.

| 17. Key Words Noise Prediction Combustion Noise Entropy Noise Vorticity Noise | 18. Distribution Statement Document is available to the public through the National Technical Information Service, Springfield, Virginia  22161. | |
|---|---|---|
| 19. Security Classif. (of this report) UNCLASSIFIED | 20. Security Classif. (of this page) UNCLASSIFIED | 21. No. of Pages 152 | 22. Price |

Form DOT F 1700.7 (8-69)

# METRIC CONVERSION FACTORS

## Approximate Conversions to Metric Measures

### LENGTH

| Symbol | When You Know | Multiply by | To Find | Symbol |
|---|---|---|---|---|
| in | inches | *2.5 | centimeters | cm |
| ft | feet | 30 | centimeters | cm |
| yd | yards | 0.9 | meters | m |
| mi | miles | 1.6 | kilometers | km |

### AREA

| Symbol | When You Know | Multiply by | To Find | Symbol |
|---|---|---|---|---|
| in² | square inches | 6.5 | square centimeters | cm² |
| ft² | square feet | 0.09 | square meters | m² |
| yd² | square yards | 0.8 | square meters | m² |
| mi² | square miles | 2.6 | square kilometers | km² |
|  | acres | 0.4 | hectares | ha |

### MASS (weight)

| Symbol | When You Know | Multiply by | To Find | Symbol |
|---|---|---|---|---|
| oz | ounces | 28 | grams | g |
| lb | pounds | 0.45 | kilograms | kg |
|  | short tons (2000 lb) | 0.9 | tonnes | t |

### VOLUME

| Symbol | When You Know | Multiply by | To Find | Symbol |
|---|---|---|---|---|
| tsp | teaspoons | 5 | milliliters | ml |
| Tbsp | tablespoons | 15 | milliliters | ml |
| fl oz | fluid ounces | 30 | milliliters | ml |
| c | cups | 0.24 | liters | l |
| pt | pints | 0.47 | liters | l |
| qt | quarts | 0.95 | liters | l |
| gal | gallons | 3.8 | liters | l |
| ft³ | cubic feet | 0.03 | cubic meters | m³ |
| yd³ | cubic yards | 0.76 | cubic meters | m³ |

### TEMPERATURE (exact)

| Symbol | When You Know | Multiply by | To Find | Symbol |
|---|---|---|---|---|
| °F | Fahrenheit temperature | 5/9 (after subtracting 32) | Celsius temperature | °C |

*1 in = 2.54 (exactly). For other exact conversions and more detailed tables, see NBS Misc. Publ. 286, Units of Weights and Measures, Price $2.25, SD Catalog No. C13.10:286.

## Approximate Conversions from Metric Measures

### LENGTH

| Symbol | When You Know | Multiply by | To Find | Symbol |
|---|---|---|---|---|
| mm | millimeters | 0.04 | inches | in |
| cm | centimeters | 0.4 | inches | in |
| m | meters | 3.3 | feet | ft |
| m | meters | 1.1 | yards | yd |
| km | kilometers | 0.6 | miles | mi |

### AREA

| Symbol | When You Know | Multiply by | To Find | Symbol |
|---|---|---|---|---|
| cm² | square centimeters | 0.16 | square inches | in² |
| m² | square meters | 1.2 | square yards | yd² |
| km² | square kilometers | 0.4 | square miles | mi² |
| ha | hectares (10,000 m²) | 2.5 | acres |  |

### MASS (weight)

| Symbol | When You Know | Multiply by | To Find | Symbol |
|---|---|---|---|---|
| g | grams | 0.035 | ounces | oz |
| kg | kilograms | 2.2 | pounds | lb |
| t | tonnes (1000 kg) | 1.1 | short tons |  |

### VOLUME

| Symbol | When You Know | Multiply by | To Find | Symbol |
|---|---|---|---|---|
| ml | milliliters | 0.03 | fluid ounces | fl oz |
| l | liters | 2.1 | pints | pt |
| l | liters | 1.06 | quarts | qt |
| l | liters | 0.26 | gallons | gal |
| m³ | cubic meters | 35 | cubic feet | ft³ |
| m³ | cubic meters | 1.3 | cubic yards | yd³ |

### TEMPERATURE (exact)

| Symbol | When You Know | Multiply by | To Find | Symbol |
|---|---|---|---|---|
| °C | Celsius temperature | 9/5 (then add 32) | Fahrenheit temperature | °F |
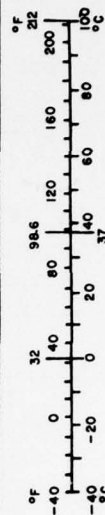
## Summary

This program was undertaken because of some relatively divergent results in the literature concerning combustion noise from gas turbine combustors. Especially in regard to sound power output the results of several workers could not be reconciled and there was question concerning the actual sources of noise which were present in various experiments. The purposes here were unification of past results, development of a rational foundation for the results and noise source identification.

A theory was developed here for the behavior of the combustor interior acoustics which clearly shows that the interior pressure fluctuations are related to at least three causal mechanisms - direct combustion noise, entropy noise and vorticity - nozzle interaction noise. After correcting the results of many past experiments through use of the theory it is shown that a unified correlation of sound power output from combustor rigs can indeed be developed, and, moreover, that it has a rational theoretical basis. It was shown that most past tests were in configurations which precluded appearance of entropy and vorticity noise. Theoretically, however, it was shown that there is a reasonable expectation that if the _level_ of these two sources could be predicted or measured the _scaling_ could be expected to follow the same laws as direct combustion noise.

Experimentally, the situation found in engines was simulated - the combustor terminated by a choked nozzle. Here, vorticity and entropy noise would be expected to appear and, indeed, were found. By

use of cross spectral density and multiple coherence techniques it
was found for the combustor tested that a) vorticity noise was at
least as large as combustion noise, b) entropy noise is minor insofar
as overall sound output is concerned and appears mainly at low fre-
quency, c) all noise sources are coherent with each other over various
frequency ranges so that an unambiguous separation could not be made,
d) due to the choked nozzle impedance and transmittance properties
the noise is higher frequency ($\approx$ 2000 Hz) than heretofore believed
and e) some other unexplained noise source or nonlinear behavior con-
taminated the results at low frequency.

It was additionally found that the overall noise output was
higher than expected in the configuration used, which employed a dif-
fuser terminating the choked nozzle. It is conjectured that the addi-
tional noise, which was coherent with combustor interior events, was
due to vorticity interaction with the decelerating diffuser flow. It
was also experimentally found that the theoretical expectation was
borne out that the total noise scaled in accordance with the direct
combustion noise scaling laws.

Some effort was expended in direct measurement of the nozzle
impedance properties through use of a separate entropy tube facility
and the use of cooled film probes in the combustor. These efforts
were of marginal success. In the end, theoretical impedance values
were used for the source identification portion of the program.

The correlation techniques of Pratt & Whitney and General Electric
for combustor rigs and engines were reviewed and some suggestions for
incorporating the results of this program were made.

Table of Contents

List of Illustrations

List of Tables

## Nomenclature

a      combustor radius or specific acoustic admittance for isentropic waves

A      area or fractional heat release rate fluctuation,

$$\int\limits_V Q' \cos \mathcal{K} x \, dV \Big/ \int\limits_V \bar{Q} \, dV$$

b      specific acoustic admittance for non-isentropic waves

c      speed of sound

$c_p$      specific heat at constant pressure

C      circumference

D      denominator defined in Eqs. (12)

f      function defined in Eq. (1)

F      fuel/air ratio

$H_{ij}$      transfer function between signal i and signal j

i      $(-1)^{1/2}$

k      wavenumber, $\omega/\bar{c}$

l      combustor length

M      Mach number

$\underrightarrow{n}$      unit outward normal vector

p      pressure

P      acoustic power

Q      heat release rate per unit volume

$\underrightarrow{r}$      position vector

R      gas constant

s      entropy

$S_i$      auto spectrum of signal i

$S_{ij}$      cross spectral density of signal i and signal j

$t$      temperature

$t_o$      sample time in Fourier transform operation

$T$      temperature

$u$      axial velocity

$u_{ref}$      reference velocity

$\vec{v}$      velocity vector

$V$      $\frac{1}{A_e} \int_A (u_v/\Delta\bar{u})\, dA$

$x$      axial distance

$y,z$      transverse dimensions

$< >$      time average

$\alpha_e$      defined in Eqs. (12)

$\beta_w$      specific acoustic wall admittance

     ratio of specific heats

$\Delta$      change across combustor

$\eta$      coordinate or coefficients in Eq. (26)

$\varkappa$      complex wavenumber

$\rho$      density

$\sigma$      $\frac{1}{A_e} \int_A (s'/\Delta\bar{s})\, dA$

$\Sigma$      $\frac{1}{A_e} \int_A (s'/c_p)\, dA$

$\tau$      $\frac{1}{A_e} \int_A (t'/\bar{t})\, dA$

$\omega$       circular frequency

## Subscripts

a       acoustic part of fluctuations

av       representative average value

e       exit of combustor

$e_q$       equivalent reflection free

i       inlet to combustor or incident waves

o       microphone at $x = \ell$

ref       reference conditions

v       vortical part of fluctuation

x       microphone at interior x-position

$\infty$       exterior condition

1       exterior microphone

$\omega$       Fourier-transformed quantity

## Superscripts

$\wedge$       cross section area average

$-$       steady state or mean

$'$       fluctuation about mean

## I.  Introduction

During the past decade there has been rather intense research on the question of "core engine", "core", or "excess" noise from aircraft gas turbine units.  This is noise which emanates from the core (working part of the airflow which passes through the turbine) of the engine.  All noise due to the fan (on a turbofan engine) or the jet exhaust is excluded; moreover, turbine noise, which is identifiable by itself, is excluded.  For several reasons, it has been suspected for some time  that processes taking place within the combustor are responsible for core noise, but there has been controversy over the exact nature of the processes.

Pratt & Whitney[1] claim correlation of combustor rig and core noise data on the basis of direct combustion noise as the dominant noise source.  Direct combustion noise is a dilation of the flow, and consequent acoustic wave production, due to fluctuations in the aggregate heat release rate in the combustor. On the other hand, Cumpsty[2] claims correlation of core noise results based on the mechanism of entropy noise.  Entropy noise is noise produced by hot or cold spots traversing a pressure gradient such as exists in the nozzle guide vanes preceeding the turbine.  Moreover, combustor rig tests on a single combustor[3] have recently shown that under conditions of such a pressure gradient entropy noise tends to dominate direct combustion noise.  Calculations in Ref. (1), however, based upon a particular theory of entropy noise, do not

support the  contention that entropy noise is a strong noise source in engines.

These controversies are compounded by the facts that recent combustor rig and core noise data, correlated without any theoretical basis, for General Electric devices[4] do not agree with the correlations of Ref. (1).  It has furthermore been noted in Ref. (3) that there may be another noise source which has not been considered or measured as yet.  This new source, called vorticity noise, is caused by mass flow fluctuations, due to the turbulence, entering the choked or nearly choked flow of the nozzle guide vanes.  Order of magnitude calculations suggest that this source is at least as large as entropy noise.

Consequently, this program was undertaken to see if  a) the results of Refs. (1) and (4) are, in fact, compatable,  b) the three sources of vorticity, entropy and direct combustion noise can be separated and quantified and  c) a unified core noise correlation could be developed.

## II.  Theory

### General Formulation

The general aeroacoustics formalism to be used for the theory of combustor noise is the linearized vorticity-acoustic field approach.  This was used in Ref. (3) but some of the details were omitted there and some modifications are necessary to account for vorticity noise.  The approach has a particular simplicity (and is, in fact, only valid) for low frequency noise so that the plane wave mode is the only important acoustic mode.  The approach is detailed in Ref. (5) for a constant property mean flow, but substantial modifications are necessary in the case of combustors with variable velocity and thermodynamic properties.

The approach consists of letting the perturbation velocity, $\underline{v}'$, and the perturbation pressure, $p'$, be split into a vortical part, associated with the turbulence, and a dilational part, associated with the acoustic wave motion.  That is

$$\underline{v}' = \underline{v}'_v + \underline{v}'_a \quad , \quad p' = p'_v + p'_a$$

where the velocity components have the property that $\nabla \times \underline{v}'_a = \nabla \cdot \underline{v}'_v = 0$.  These forms are placed in the inviscid equations of gasdynamics with chemical heat release and then split into a set of  a) steady state equations,  b) perturbation equations for the acoustic components and  c) perturbation equations for the

vortical components. This is done in Ref. (3). However, it is found that such a split is only rigorously possible if the condition

$$\nabla p_a' \times \nabla \bar{\rho} = 0$$

is met. That is, the gradient of the acoustic pressure must be parallel to the gradient of mean density. The only reasonable flow and acoustic situation which will satisfy this requirement is a nearly one-dimensional mean flow upon which is superimposed plane wave acoustic motion. This will be assumed.

The limit of low Mach number will also be assumed, in which case the differential equations for the Fourier transform of the acoustic pressure becomes[3]

$$\nabla^2 p_\omega + k^2 p_\omega = - f_\omega = - \frac{i_\omega Q_\omega}{\bar{c}^2} (\gamma - 1) \tag{1}$$

Also assumed in Eq. (1) is that the speed of sound is roughly constant through the combustor (an average value has been used). The "a" subscript has been dropped for clarity in Eq. (1) but it is understood that the acoustic pressure obeys Eq. (1). Also, to be consistent with the splitting requirement the transverse derivative in Eq. (1) must be weak compared with the longitudinal derivative.

The neglect of terms proportional to the Mach number in Eq. (1) is permissable because there are no essential physics omitted. That is, the effect of the flow terms is minor and is primarily

felt in the wave propagation speed so that resonant frequencies are only slightly shifted from their no-flow values. This is also the primary effect of variable speed of sound. The same is not true when one considers the boundary conditions to Eq. (1), where flow terms are essential to a proper description of acoustic damping and noise generation, as will be seen. Consequently, more care is necessary in the boundary conditions formulation. It has furthermore been assumed in Eq. (1) that liquid-gas momentum (drag) interactions are unimportant. This has justification in numerous studies of combustion instability,[6] where the drag effect is of the same order of magnitude as the flow terms.

Cross-section averages of terms will be denoted by a hat superscript. That is, for example,

$$\hat{p}_\omega = \frac{1}{A} \int dA \, p_\omega \, (\underline{r}) = \hat{p}_\omega(x)$$

$$\hat{f}_\omega = \frac{1}{A} \int dA \, f_\omega \, (\underline{r})$$

These are the effective plane wave values of quantities. Taking the cross-section average of Eq. (1) and assuming a constant area combustor

$$\frac{d^2 \hat{p}_\omega}{dx^2} + k^2 \hat{p}_\omega + \frac{1}{A} \int_C \nabla p_\omega \cdot \underline{n} \, dC = - \hat{f}_\omega \qquad (2)$$

where the divergence theorem has been used.

The linearized momentum equation for the acoustic parts of $p_\omega$ and $\underset{\rightarrow}{v}_\omega$ is [3]

$$i \omega \underset{\rightarrow}{v}_\omega + \nabla(\bar{u} \underset{\rightarrow}{v}_\omega = - \frac{\nabla p_\omega}{\bar{\rho}} \tag{3}$$

where the "a" subscript has been dropped. In the outward normal direction this becomes

$$\bar{\rho} \, i \, \omega \, \underset{\rightarrow}{v}_\omega \cdot \underset{\rightarrow}{n} = - \nabla p_\omega \cdot \underset{\rightarrow}{n}$$

Defining the specific wall admittances as

$$\beta_w = \frac{\underset{\rightarrow}{v}_\omega \cdot \underset{\rightarrow}{n} \, \bar{\rho} \, \bar{c}}{\hat{p}_\omega}$$

and assuming $\beta_w$ is uniform along and around the walls Eq. (2) becomes

$$\frac{d^2 \hat{p}_\omega}{dx^2} + k^2 \hat{p}_\omega - i \, k \, \hat{p}_\omega \, \beta_w \frac{C}{A}$$

$$= \frac{d^2 \hat{p}_\omega}{dx^2} + \varkappa^2 \hat{p}_\omega = - \hat{f}_\omega \tag{4}$$

The effect of $\beta_w$, if positive and real, is to introduce damping at the wall. In leading to Eq. (4) the flow term in Eq. (3) has been dropped. While it may sometimes be of the same order as the first term, what is really being done here is to introduce an effective

$\beta_w$ which will later be experimentally determined, but contains the wall damping effect. In Eq. (4), therefore, the wall boundary condition is already incorporated.

At the combustor head end it is assumed the wall (even if there are air entrance slots) is acoustically hard so that $u_\omega(0,y,z) = \hat{u}_\omega(0) = 0$. Equation (3) then yields

$$\frac{d\,\hat{p}_\omega}{dx}\Bigg)_{x=0} = 0 \tag{5}$$

At the nozzle end an admittance condition is involved for the plane wave quantities that

$$\frac{\hat{u}_{\omega_a} + \hat{u}_{\omega_v}}{\bar{c}} + a_\omega\,\frac{\hat{p}_{\omega_a}}{\bar{p}} + b_\omega\,\Sigma_\omega = 0 \tag{6}$$

In several limits the admittance coefficients, $a_\omega$ and $b_\omega$ may be calculated. For example, if the nozzle is choked and the frequency is low[7] $a_\omega \rightarrow -(\gamma-1)\,M_e/2\gamma$ and $b_\omega \rightarrow -M_e/2$ ; if the nozzle is a pipe, open to free space, and the Mach number is low, the Levine-Schwinger problem[8] is the appropriate limit, whereby as frequency tends toward zero $a_\omega \rightarrow \infty$ and $b_\omega = 0$. In general, however, $a_\omega$ and $b_\omega$ must be measured.

Taking the axial component of Eq. (3) and averaging over the cross section,

$$i \, \omega \, \hat{u}_{\omega_a} + \bar{u}_e \, \frac{d \, \hat{u}_{\omega_a}}{dx} = - \frac{1}{\rho} \, \frac{d \, \hat{p}_{\omega_a}}{dx} \tag{7}$$

at the exit plane where $d\bar{u}/dx = 0$ has been assumed. The linear-ized continuity equation at the exit plane is,[3] when averaged over the exit plane

$$i \, \omega \, \hat{\rho}_\omega + \bar{u}_e \, \frac{d\hat{\rho}_\omega}{dx} + \bar{\rho}_e \, \widehat{\nabla \cdot \vec{v}_{\omega_a}} = 0 \tag{8}$$

Next the perfect gas equation of state is introduced, and, when averaged over the exit plane

$$\frac{\hat{\rho}_\omega}{\bar{\rho}_e} = \frac{1}{\gamma} \, \frac{\hat{p}_\omega}{\bar{p}} - \Sigma_\omega \tag{9}$$

Applying the divergence theorem to $\nabla \cdot \vec{v}_{\omega_a}$, using the wall admittance condition, and combining Eqs. (7) - (9), there results

$$\frac{d\hat{p}_{\omega_a}}{dx} - i \, k \, \hat{p}_{\omega_a} \left[ M_e + \gamma \, a_\omega + \frac{C}{A} \, \frac{M_e \, \beta_w}{ik} \right] =$$

$$\gamma \bar{p} \left[ \frac{\hat{u}_{\omega_v}}{\bar{c}_e} \, i \, k + \Sigma_\omega \, i \, k \, (b_\omega - M_e) - M_e^2 \, \frac{d \, \Sigma_\omega}{dx} \right] \tag{10}$$

as the exit plane boundary condition. However, the energy equation,

written in the form of the second law of thermodynamics, demands
that the entropy fluctuations be convected with the fluid.  Hence,

$$M_e \frac{d \Sigma_\omega}{dx} + i k \Sigma_\omega = 0$$

at the exit plane and Eq. (10) simplifies to

$$\frac{d\hat{p}_{\omega_a}}{dx} - i k \hat{p}_{\omega_a} \left[ M_e + \gamma a_\omega + \frac{C}{A} \frac{M_e \beta_w}{ik} \right] =$$

$$ik\gamma\bar{p} \left[ \frac{\hat{u}_{\omega_v}}{\bar{c}_e} + b_\omega \Sigma_\omega \right] \tag{11}$$

The second term in brackets is generally of the order of  $M_e$  and
would ordinarily be neglected if the procedure used to derive
Eq. (1) were used.  However, this term provides damping and prevents
unbounded resonances.  It is important to retain mean flow-dependent
terms when they add damping, whereas in Eq. (4) the flow terms neglected
only shift resonant frequencies a slight amount.

The right hand side of Eq. (11) contains two source terms -
vorticity and entropy at the combustor termination.  The combustion
noise source term occurs in the differential Eq. (4).  Damping is
provided by the wall impedance in Eqs. (4) and (11), by the nozzle
through  $a_\omega$  in Eq. (11) and by convection of acoustic energy by
the mean flow in Eq. (11).  Hence, all of the basic physics are

included, although some approximations have been introduced.

## Solution and Orders of Magnitude

Now dropping the "hat" superscript and "a" subscript; the solution to Eq. (4) subject to Eqs. (5) and (11) may readily be obtained. It is

$$\frac{p_\omega(x)}{\bar{p}} = A_\omega H_{Ap} + V_\omega H_{vp} + \sigma_\omega H_{\sigma p}$$

$$H_{Ap} = \left\{ \cos \mathcal{K}(x-\ell) + \frac{\alpha_e}{\mathcal{K}} \sin \mathcal{K}(\ell-x) \right.$$

$$H_{vp} = \left( \frac{i\, k\, \gamma\, M_e\, \Delta T/T_e}{D} \right) \quad \cos \mathcal{K} x$$

$$H_{\sigma p} = \left. \frac{b_\omega}{M_e} \cos \mathcal{K} x \right.$$

$$D = \alpha_e \cos \mathcal{K}\ell - \mathcal{K} \sin \mathcal{K}\ell$$

$$\alpha_e = -\, i\, k\, (M_e + \gamma a_\omega + \frac{C}{A} \frac{M_e\, \beta_w}{i\, k}) \qquad (12)$$

The three source terms, $A_\omega$, $V_\omega$ and $\sigma_\omega$ are defined in the Nomenclature and are basically the Fourier transforms of the _fractional_ heat release rate, exit plane vorticity and exit plane entropy fluctuation. From the first of Eqs. (12) the pressure transform is linearly related to the three causal processes.

It is desirable to gain an idea of some orders of magnitude from Eqs. (12). Assume, for the moment that $V_\omega = \sigma_\omega = 0$ so that only combustion noise is present. Furthermore, assume that a combustor is terminated by an impedance matching device so that only downstream acoustic waves are propagating (no reflections). In such a case $a_\omega \approx 1/\gamma$ and if $M_e << 1$ then $\alpha_e \approx -ik$. Moreover, for low $\beta_w$, $k \approx \mathcal{K}$. With these approximations, at $x = \ell$,

$$\frac{p_\omega(\ell)}{\bar{p}} = \frac{\gamma i\, M_e\, \Delta T/T_e}{-i\cos k\ell + \sin k\ell} A_\omega$$

Constructing a spectral density from the Fourier transform[9]

$$2\pi \frac{p_\omega p_\omega{}^*}{t_o} = \frac{S_p}{\bar{p}^2} = (\gamma\, M_e\, \Delta T/T_e)^2\, S_A$$

The acoustic power is given by

$$P = A_e \int_{-\infty}^{\infty} \frac{S_p}{\bar{\rho}_e\, \bar{c}_e}\, d\omega = \frac{A_e\, \bar{p}^2}{\bar{\rho}_e\, \bar{c}_e} (\gamma\, M_e\, \Delta T/T_e)^2 \int_{-\infty}^{\infty} S_A\, d\omega$$

$$= A_e\, \bar{c}_e{}^3\, \bar{\rho}_e\, (M_e\, \Delta T/T_e)^2 <A^2>$$

It is to be noted that a reference inlet velocity may be defined by $\bar{\rho}_i\, \bar{u}_{ref} = \bar{\rho}_e\, \bar{u}_e$ and $\bar{\rho}_i/\bar{\rho}_e = \bar{T}_e/\bar{T}_i$. Consequently, the grouping on the right above may be written in terms of more convenient design variables as

$$P = <A^2> A_e u_{ref}^2 \ \bar{p} \left(\frac{\Delta T}{T_i}\right)^2 \ \frac{\gamma}{R(T_i + \Delta T)} \tag{13}$$

Now, a correlation formula is to be presented later in this report, which accurately predicts combustion noise experiments which closely meet the requirements of the assumptions above, has been applied to a particular run from Ref. (4). The numbers are

$u_{ref}$ = 276 ft/sec     $A_e$ = 225 in$^2$          $\bar{p}$ = 65.5 psia

$\Delta T$ = 910 $^\circ$R     $T_i$ = 1635 $^\circ$R          $P$ = 152.4 w

When introduced into the formula above $<A^2> = 8.9 \times 10^{-4}$ results. Consequently the rms value of $A$ is roughly 0.03. Another way of saying this is that the fluctuation level in the total heat release rate is about 3% of the mean heat release rate.

Now assume that this heat release rate fluctuation remains at the same level in an installed configuration where the combustor is terminated by a choked or nearly choked nozzle. In such a case $b_\omega \approx -\frac{M_e}{2}$ for short nozzles.[7] Consequently in looking at $H_{Vp}$, $H_{\sigma p}$ and $H_{Ap}$ in Eqs. (12), all three terms in the equation for $p_\omega/\bar{p}$ scale almost exactly the same and in fact are of the same order of magnitude if $<A^2>$, $<V^2>$ and $<\sigma^2>$ are of the same order of magnitude. This is expected to be so, since relative intensities of turbulence are high in a combustor[10] and temperature fluctuation levels are also high.[3] Of course $\sigma$ and $V$

are cross-section averages which will depress them in magnitude compared with their point magnitudes. But it is expected that these quantities will be of the order of 1 to 3%. The conclusion is that for the interior pressure fluctuation, it may be expected to be strongly influenced by all three mechanisms.

This does not say anything about the noise that gets out, since a) there are transmission properties of the combustor termination to worry about and b) the nozzle generates additional downstream noise by the entropy and vorticity mechanisms.

Using Equation (7) one can calculate the acoustic velocity. Upon so doing one discovers the highly important fact that the velocity due to the vorticity source is $90^\circ$ out of phase with the pressure. Consequently, if there is no acoustic termination downstream of the combustor exit plane to interact with $V$ to produce noise no sound power output can result from $V$. Moreover, $b_\omega = 0$ in cases where no pressure gradient terminates the combustor flow so that these are experimental situations where combustion noise is the only noise source.

Returning to Equation (13), this equation gives an idea of scaling laws to be expected in the absence of entropy and vorticity noise. The only major problem is in the estimation of the scaling of $<A^2>$. For order of magnitude purposes the $\cos K x$ term in the definition of $A$ can be omitted and

$$< A^2 > = \frac{\left( \int Q' \, dV \right)^2}{\left( \int \bar{Q} \, dV \right)^2} \ .$$

Estimation of the square of stochastic variables like $Q'$ when integrated over space yields

$$< A^2 > \propto V\, V_{cor}\, \frac{< Q'^2 >_{av}}{\left(\int \bar{Q}\ dV\right)^2} = \frac{V_{cor}}{V}\ \frac{< Q'^2 >_{av}}{\bar{Q}^2_{av}}$$

Mathews[1] assumed that the correlation volume was the entire volume of reactants produced around a single fuel nozzle. While it may be plausible that there is a certain degree of correlation within the volume served by a single fuel nozzle, since there are many uncorrelated turbulent eddies within such a volume, there cannot be perfect correlation. Moreover, the turbulence size scale is probably most closely linked to a transverse combustor dimension, as in pipe flow. Consequently, $V_{cor}/V \propto (A_e^{1/2}/\ell)N_f^{-a}$ seems reasonable to assume with $0 < a < 1$. Then if it is argued that the mean fluctuation level of $Q'$ is proportional to the mean heat release rate, an assumption which frequently is borne out as true in turbulence,

$$< A^2 > \propto (A_e^{1/2}/\ell)N_f^{-a}$$

results. When this is placed back into Eq. (13)

$$P \propto N_f^{-a}\ (A_e^{1/2}/\ell)\ A_e\ u_{ref}^2\ \bar{p}\ \left(\frac{\Delta T}{T_i}\right)^2\ \frac{1}{T_i + \Delta T} \qquad (14)$$

results. This suggests the variables against which to test and

correlate the data. Moreover, it suggests that a power law type correlation fit may be adequate.

## Inversion for the Source Quantities

The two types of x-wise variation in the H's of Eqs. (12) suggest that, if a third independent measurement is made, two different pressure measurements will allow an inversion to the source quantities. In fact, taking positions x and $x = \ell$ and denoting the pressure transforms there as $p_x$ and $p_o$, there results

$$A_\omega = \frac{i \, \varkappa \, T_e \, (p_x \cos \varkappa \ell - p_o \cos \varkappa x)}{\gamma \, k \, \Delta T \, M_e \, \sin \varkappa(\ell - x)} \tag{15}$$

This highly important result states that the <u>combustion rate fluctuation may be obtained by a two point pressure measurement, and is independent of the admittance relations</u>.

The third independent measurement which will be made is the cross section average of the temperature fluctuation at the exit plane. This is

$$\tau_\omega = \frac{1}{A_e} \int dA \, \frac{t_\omega}{\bar{t}} = \sum_\omega + \frac{\gamma-1}{\gamma} \, \frac{p_o}{\bar{p}} \tag{16}$$

It should be noted that $\sum_\omega$ and $\sigma_\omega$ are related by $\sum_\omega = (\Delta T/T_e) \, \sigma_\omega$. Then Eqs. (12) may also be inverted for $V_\omega$. The result will not be stated here, but $V_\omega$ does depend upon

$a_\omega$ and $b_\omega$, <u>but</u> <u>it</u> <u>is</u> <u>the</u> <u>only</u> <u>one</u> <u>of</u> <u>the</u> <u>three</u> <u>source</u> <u>terms</u> <u>that</u> <u>does,</u> <u>using</u> <u>this</u> <u>measurement</u> <u>scheme</u>.

It is to be noted in Eq. (15) that the inversion process becomes singular (0/0) as $\omega$, k and $\varkappa \rightarrow 0$. This is the consequence of the fact in Eqs. (12) that there is no wave structure as frequency tends towards zero; only a bulk mode oscillation results and $p_o = p_x$. This fact will be used to advantage later in transducer calibration.

A contaminant, not accounted for in the above theory, is hydrodynamic noise. It is non propagational pseudosound which sometimes makes its appearance in the combustor to be used at low frequency[3]. It can be detected, so that if it appears the frequency ranges where it appears will be excluded from the data reduction process. Otherwise, it is assumed that the theory is valid and A, V and $\sigma$ may be extracted from the internal measurements.

## Comparison between Experiments on Different Rigs

Often in the literature "apples and oranges" have been compared when comparing combustor noise results. The solution of Eqs. (12) clearly shows that the combustor termination (through $\alpha_e$) plays a strong role in the interior pressure fluctuation. Consequently, it may be expected to play a strong role in the noise output also. Different terminations have been used on different experiments. In order to make valid comparisons between experiments,

the results must be corrected to equivalent terminations.

Three cases will be considered. These are a) a combustor terminated by an open unflanged end, open to the atmosphere, b) a termination by a short, choked nozzle and c) a termination by either a perfect impedance matching device, or, what is equivalent, an infinite extension to the pipe at the exit plane. Where necessary it is assumed that the combustor is a right circular cylinder. Direct combustion noise is the only noise source under consideration and it is assumed that $A_\omega$ is unaffected by the termination, for the same operating conditions (there is no reason to suspect otherwise). The exit Mach number is assumed low and $ka << 1$ so that in case a) the Levine-Schwinger result may be applied that[8]

$$a_\omega = \frac{-1}{\gamma\, ka\,(0.6\, i + 0.25\, k\, a)}$$

In case b) the nozzle is assumed short so that

$$a_\omega = -\frac{\gamma-1}{2\gamma}\, M_e$$

In case c) the Mach number is assumed low so that

$$a_\omega = -\frac{1}{\gamma}$$

For purposes of calculation $\beta_w$ is assumed small so that $\varkappa \to k$. Where necessary (in case a)) $\ell/a = 7.52$ has been taken, corresponding to the rig of Ref. (1).

When only combustion noise is under consideration the exit plane pressure, along with the exit plane impedance, are sufficient to calculate the power output. Using Eqs. (12), the admittances above, and calculating the power per unit frequency interval, the results may be expressed in the form $P_{\omega \text{ case } a}/P_{\omega \text{ case } c}$ and $P_{\omega \text{ case } b}/P_{\omega \text{ case } c}$. The results for $M_e$ = 0.3 are shown in Figure 1. It is seen that the results are quite frequency sensitive, but that either of the reflecting terminations causes a substantial drop in radiated power, compared with a non-reflecting termination. For the open end (case a) the quarter and 3/4 wave resonances are clearly seen, whereas for the short choked nozzle case the half-wave resonance is present. This result shows clearly that, if results from case c and case a, for example, are compared experimentally, a correction of the order of 10 dB in radiated power must be applied to the results. Moreover, the correction must carefully consider the frequency content of the noise. Such a correction will be used in the next section.

## Exterior Noise

The transform of the exterior noise may always be written as

$$\frac{P_{\omega_1}}{\bar{P}_1} = H_{A1} A_\omega + H_{\sigma 1} \sigma_\omega + H_{V1} V_\omega + Z_\omega \qquad (17)$$

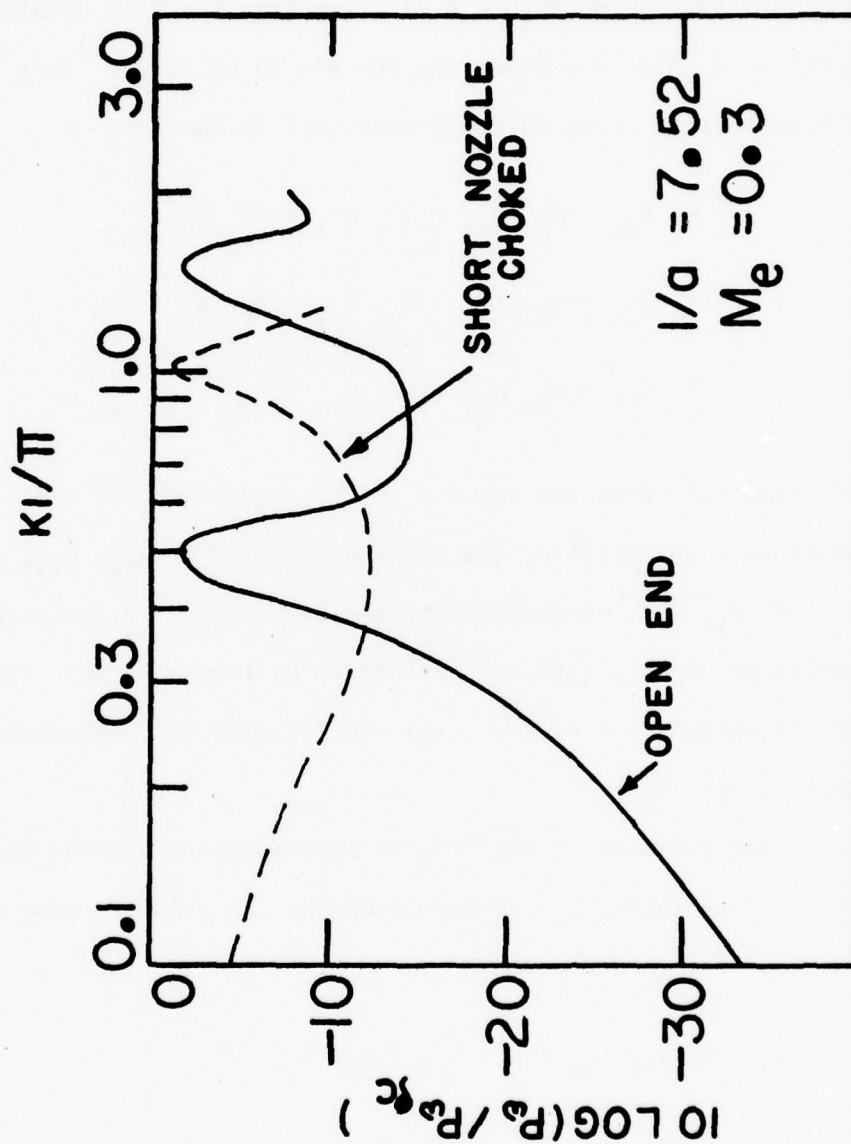where $Z_\omega$ is the deviation from the linear causality of the

Figure 1. Theoretical comparison of the sound radiation per unit frequency interval for two different exit plane terminations. Only direct combustion noise is considered.

first three terms. It is known that even if $Z_\omega$ is substantial
that the best linear fit in a least squares sense is obtained by
assuming $Z_\omega = 0$ and measuring the H's in Eq. (17). This is done
by constructing cross spectral densities in the form

$$S_{1A} = H_{A1} \, S_{AA} + H_{\sigma 1} \, S_{\sigma A} + H_{V1} \, S_{VA}$$

$$S_{1\sigma} = H_{A1} \, S_{A\sigma} + H_{\sigma 1} \, S_{\sigma\sigma} + H_{V1} \, S_{V\sigma}$$

$$S_{1V} = H_{A1} \, S_{AV} + H_{\phantom{A}1} \, S_{\sigma V} + H_{V1} \, S_{VV} \quad , \tag{18}$$

measuring the cross spectra and solving Eqs. (18) for the transfer
functions. In practice, the cross spectra $S_{\infty}$, $S_{1x}$, $S_{11}$, $S_{10}$,
$S_{\tau\tau}$ and $S_{1\tau}$ are measured and the cross spectra of the right
hand sides of Eqs. (18) are calculated by inverting Eqs. (12)—
that is, through use of Eqs. (15) and (16) and the associated
equation for $V_\omega$.

The goodness of the fit, or stated otherwise, the magnitude
of the contaminant $Z_\omega$, is determined by the multiple coherence
function[9]

$$\gamma^2_{1 \cdot i} = \left( H_{A1} \, S_{1A} + H_{V1} \, S_{1V} + H_{\sigma 1} \, S_{1\sigma} \right) / S_{11}$$

$$0 \leq \gamma^2_{1 \cdot i} \gamma 1 \tag{19}$$

The nearer is $\gamma^2_{1 \cdot i}$ to unity, the less is the contaminant or
deviation from linearity. In fact,

$$\gamma^2_{1\cdot i} = 1 - \frac{S_{ZZ}}{S_{11}} \tag{20}$$

Therefore multiplication of the measured spectrum, $S_{11}$, by $\gamma^2_{1\cdot i}$ gives that portion of the spectrum which is linearly, causally related to the measured sources. It is called the multiple coherent spectrum.

If the off diagonal elements of Eqs. (18) are much smaller in magnitude than the diagonal elements, the three sources are uncorrelated. This would be the ideal situation since a definite split of the noise into three components would be possible. It will be found, however, that this did not occur in certain frequency bands. A measure of correlation between the sources is the ordinary coherence function given by

$$\gamma^2 = \frac{\left|S_{ij}\right|^2}{S_{ii} \, S_{jj}}$$

$$0 \leq \gamma^2 \leq 1$$

This function will also be used in the following sections.

III.   Correlation of Past Combustor Rig Tests

In References (1), (4), (10) and (11)-(12) there is a
wealth of data regarding combustion noise from combustor rig tests.
Virtually all relevant parameters have been varied, tests at simulated
engine conditions have been conducted, and different combustor types
were used.   Comparison of correlations which have been produced for
the data, however, shows that the correlation of one manufacturer
does not recover that of another manufacturer.  It is the purpose
here to see if a unified correlation can be developed which will
adequately cover the data ranges of the cited references.

The work here will concentrate on sound power only.  The
frequency content of the cited references poses one of the great
unsolved problems in combustion noise.[13]   In Reference (1) a
theory is presented for the frequency content which appears to
recover the correct trends for the combustors of that work, but it
works for no other manufacturers'. Moreover, the results of Ref. (10)
are not explained by that theory.  About all that can really be
said is that combustion noise has been observed in the past to be
basically low frequency in nature ($\leq$ 1000 Hz).  Of course, it must
be borne in mind that the frequency content depends upon the
acoustics of the containing hardware.  Since the combustor rigs
have been different, it is perhaps not surprising that there is
confusion concerning the observed frequency content.  In any event,
even in this program there will be found some new twists in

frequency content so that the issue will be avoided here. Only sound power will be considered.

In the rigs of Refs. (1) and (10) the six different combustors were exhausting directly (with some diffusion before exit) to the atmosphere. The acoustic configuration was essentially that of an open-ended organ pipe and resonances are clearly seen in the data at the 1/4, 3/4, 5/4, etc. wave resonance points. On the other hand, the work of Refs. (4) and (11)-(12) was carried out in two different rigs which were assumed reflection free at the combustor termination. The data reduction procedure assumed that waves emanating from the combustor were not reflected from downstream impedance mismatches. In viewing these rigs, it is the judgement here that such an assumption was probably justified at least to a reasonable approximation. Consequently, the data of the various rigs cannot be directly compared unless corrections are applied to bring the data to the same basis.

The basis which is chosen here is to correct all acoustic power measurements to the "equivalent reflection free power", $P_{eq}$. Thus, the work of Ref. (4) and (11)-(12) will be accepted as is, and corrections will be applied to the data of Refs. (1) and (10). This correction will be simply done. That is, usually in Ref. (1) the combustion noise spectrum peaked at a frequency slightly higher than the 3/4 wave resonance point. Reference to Fig. 1 shows that a correction of + 7 dB is a reasonable correction to add to the data of Ref. (1). In Ref. (10) most of the noise was centered about the 1/4 wave resonance point, and reference to Fig. 1 shows that a correction

of + 1 dB is reasonable. For high accuracy a frequency dependent
correction should be applied and a summation over frequency bands
employed. However, it will be seen that the crude approximation
above yields satisfactory results.

The next thing to notice is that no entropy or vorticity noise
is expected in the cited rig tests, as discussed in Section II. Con-
sequently, there is high confidence that a form of the correlation
law suggested by Eq. (14) will satisfactorily correlate the data.

The form chosen is

$$P_{eq} = a_1 \, p^{a_2} \, u_{ref}^{a_3} \, T_i^{a_4} \, F^{a_5} \, N_f^{a_6} \, A_e^{a_7} \, (A_e^{1/2}/\ell)^{a_8}$$

(21)

This form is close to the form of Eq. (14) and is suitable for
linear multiple regression analysis after taking the logarithm of
Eq. (21). 202 data points were available from the cited references,
with 15 different combustors. The regression analysis yielded the
following results, where the theoretically expected values are also
shown:

### Table 1

Regression Analysis Results and Comparisons with Theory

|  | $a_1$ | $a_2$ | $a_3$ | $a_4$ | $a_5$ | $a_6$ | $a_7$ | $a_8$ |
|---|---|---|---|---|---|---|---|---|
| Experiment | 0.91 | 1.9 | 3.4 | -2.5 | 1.3 | -0.78 | 1.0 | 1.0 |
| Theory | N/A | 1 | 2 | -2 to -3 | 2 | 0 to -1 | 1 | 1 |

Note: The units are power in watts, pressure in psia,
velocity in ft/sec, inlet temperature in $^{\circ}$R and
exit area in square inches. All other quantities
are dimensionless

The standard deviation of the correlation is $\pm$ 3 dB and a comparison of the regression formula with the data is shown in Fig. 2. The individual General Electric combustors are pointed out in this figure because it was with these combustors that the largest scatter occurred. The correlation is considered highly interesting for several reasons. These are a) there is a rational theoretical basis which generally holds up, b) the single correlation formula holds over an extreme range of acoustic power ($10^6$) and c) the Ref. (1) conclusion of a fuel nozzle effect holds up when all combustors are considered.

A close look at the General Electric designs revealed no design parameter which, if included in the correlation, would reduce the scatter. Consequently, the $\pm$ 3 dB is accepted as mostly due to experimental error in the variety of rigs employed and in data analysis methods.

It is to be noted that if the results of Ref. (1) are not changed by the 7 dB correction, the $a_7$ exponent comes out as 2.0 rather than 1.0. This is not acceptable from the theoretical viewpoint and is viewed as confirmation of the correction procedure.

The primary deviation between theory and experiment lies in the $a_2$ and $a_3$ exponents. There is an interesting interpretation for this. The deviation from theory is by a factor of

$$p^{0.9} \, u_{ref}^{1.4} \approx (p \, u_{ref}^2)^{0.9} \propto (\rho \, u_{ref}^2)^{0.9}$$

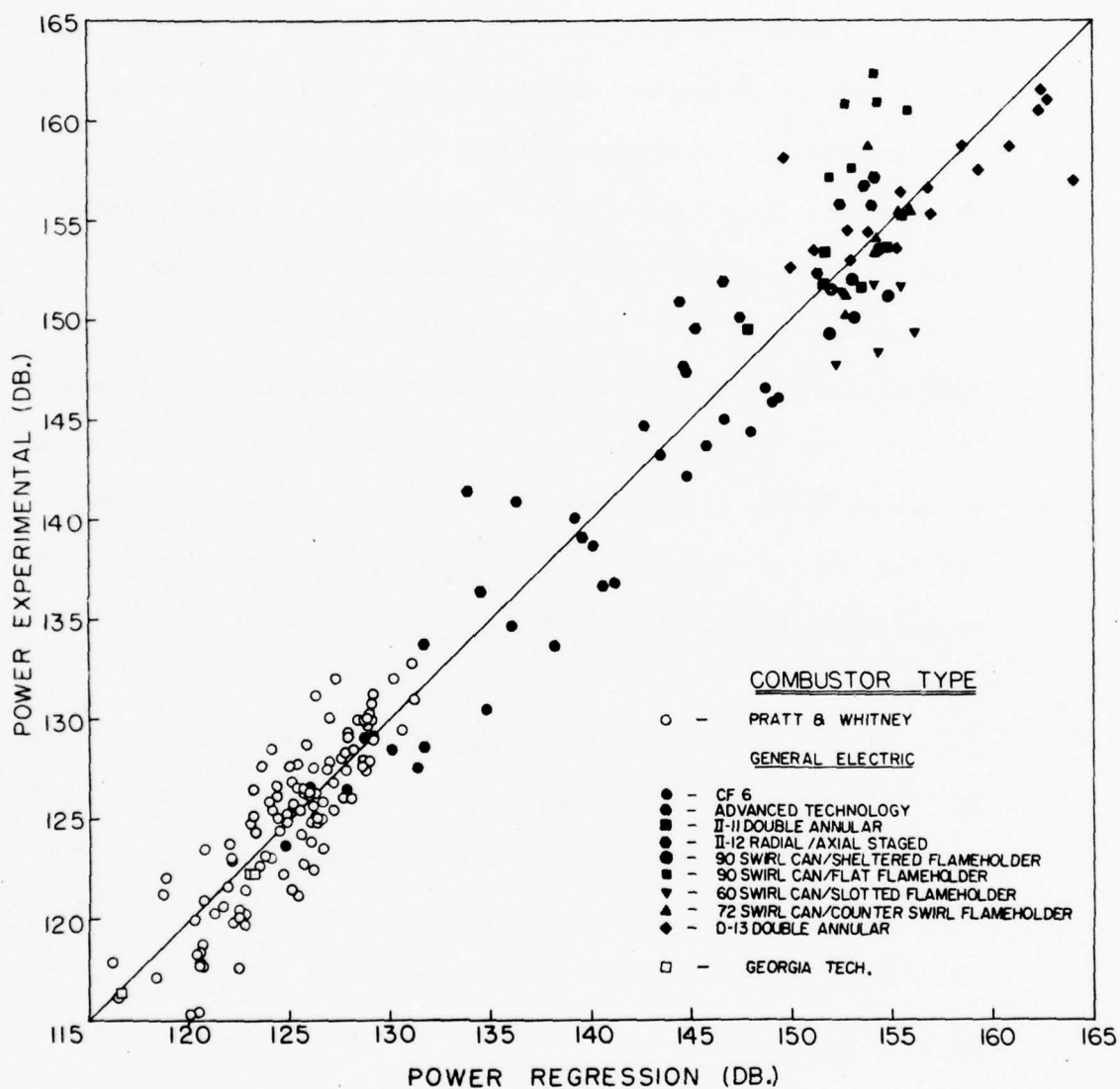That is, the deviation looks closely related to the dynamic head, a

Figure 2. Comparison of the predicted power from the regression equation with the experimental sound power.

a term which often enters in aerodynamic noise computations. Moreover,
aerodynamic noise usually scales with a high exponent on velocity.
It is conjectured here that since no experiment can be entirely free
of aerodynamic noise contamination of the combustion noise results
the high $a_2$ and $a_3$ exponents may be false. It is possible that the
theory is more accurate as to combustion noise scaling laws than the
experiments.

It is now emphasized that this is a combustor rig correlation
for equivalent power in a reflection free situation and in the absence
of entropy and vorticity noise. In an engine installation where the com-
bustor is terminated by nozzle guide vanes, the turbine assembly and
exhaust duct, several things change which will change the acoustic
power output. First, the nozzle guide vanes usually operate at a
choked or nearly choked condition. This necessitates corrections by
a form of Fig. 1 and also brings in the possibility of entropy and
vorticity noise. Second, more noise due to vorticity and entropy can
be created in the turbine, and this is combustor-related. Finally,
there are attenuation processes in the turbine and nozzle which must
be accounted for. These issues will be addressed in Section VIII.

## IV. Combustor Apparatus and Experimental Procedures

### Combustor Details

The combustor, used in the present investigation, is of can-type, taken from a Boeing 502-7D gas turbine engine unit. The original air inlet has been modified to suit the experimental set-up. Figure 3 shows a cross sectional view of the combustor. Liquid fuel is sprayed into the burner liner through a fuel nozzle. Air for combustion enters through the slots in the head end and walls of the liner. The by-passed air leaves the combustor through the annular space between the liner and the burner shell. The geometry and the arrangement of the slots is shown in Fig. 3. A spark plug is used to ignite the fuel/air mixture. Stable operation limits for this combustor were determined in a previous program (Reference (10)). The by-pass air flow rate is measured to be 26% of total air supplied. Pitot pressure distribution and mean temperature distribution of the hot gases at the burner exit plane are reported in Ref. (3).

### Flow Systems

The schematic lay-out of the flow system is shown in Fig. 4. Air for the combustor is supplied from an 861 KPa air reservoir, regulated by a valve and metered by an orifice meter. A muffler is provided in the line, upstream of the combustor, to reduce flow noises. Fuel is pumped from a tank to the fuel spray nozzle by nitrogen pressurization. A turbine flow meter measures the fuel flow rate through the system. The muffler, the fuel tank and the combus-
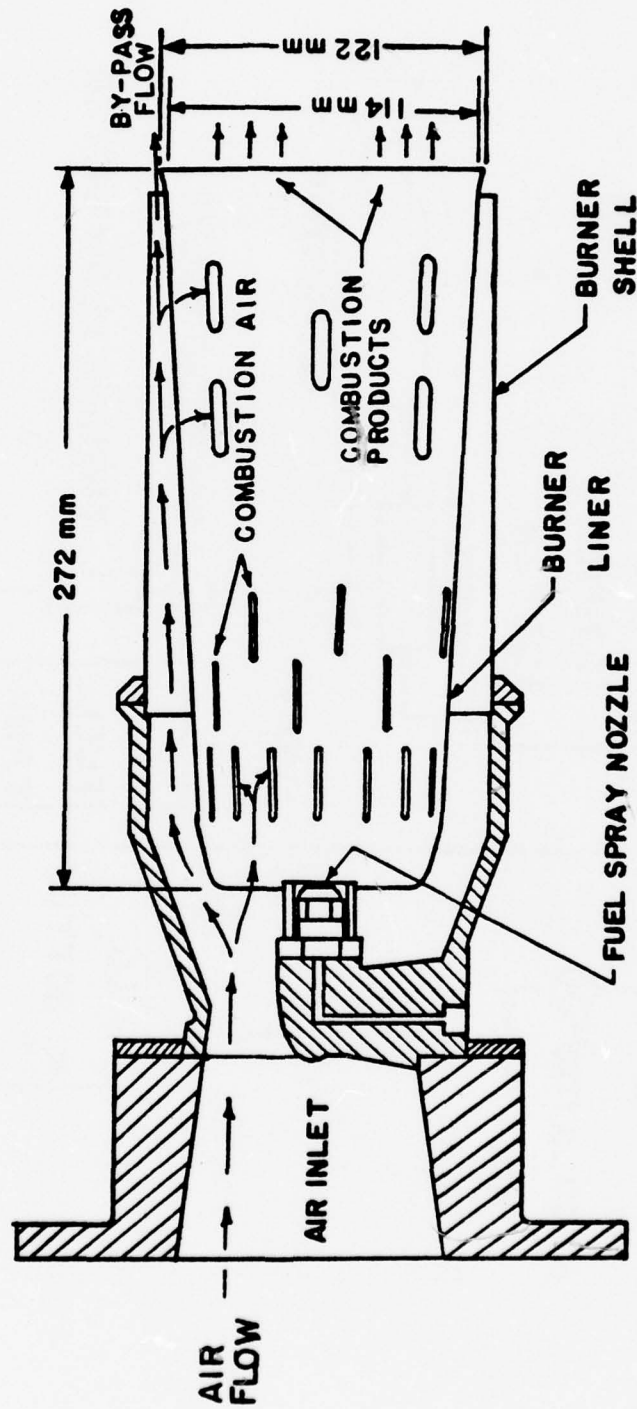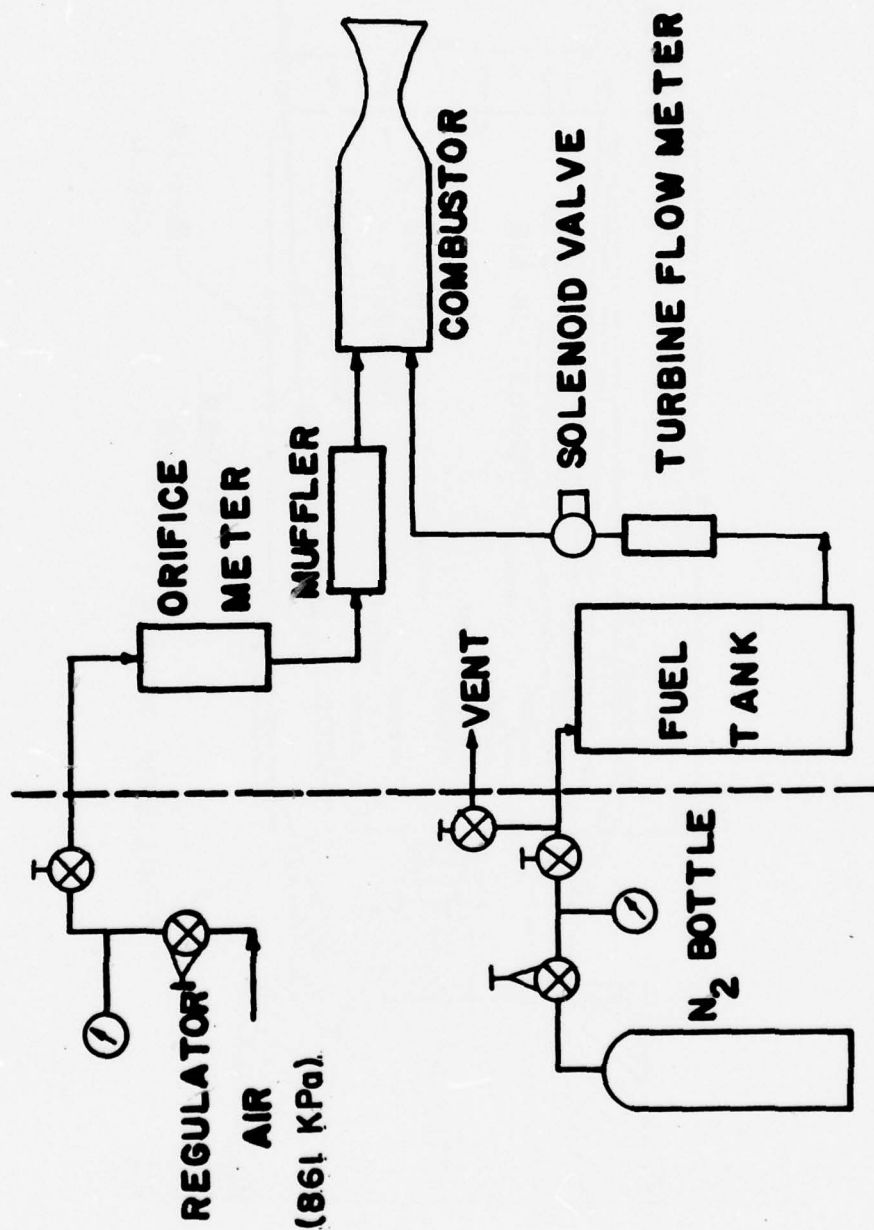
Figure 3. Combustor Details.

Figure 4. Flow System Schematic.

tor are all mounted on a test stand outside the laboratory at an open site while the flow control valves, the flow meter displays and the data acquistion systems are situated inside the laboratory.

## Measurement Techniques

The main objective of this experimental program is to estimate the strengths of various noise sources located inside the combustor (viz. combustion, entropy & vorticity) and their relative contributions to the exterior radiated noise. This requires measurements of interior pressure, temperature and velocity fluctuations as well as exterior noise characteristics. Moreover, it was desired to simulate an engine condition of choked nozzle guide vanes. Consequently, the combustor under consideration was fitted with three terminating converging-diverging nozzles. These provided contraction ratios of 14.6, 12.1 and 9.1. The diverging section is essential to keep jet noise levels very low, thereby eliminating this contaminant from the exterior measurements. After the first test run, it was discovered that a flow separation was occuring upstream of the diffuser exit. This was due to a faulty assumption of considering the diffuser as two-dimensional rather than three-dimensional. This resulted in too large an expansion angle. A new diffuser was built with very low expansion angle (half angle = $2^o$) to remedy the separation problem. For primary data reduction, four tests were carried out, all at choked conditions. Three of them were conducted with the above three nozzle-diffuser assemblies. Another one was at the middle contraction ratio,

with only the nozzle without diffuser in place. The operating conditions for these four tests are listed in Table 2. Apart from these main tests, for the middle contraction ratio, airflow and fuel/air ratio traverses were run a) at constant airflow with varying fuel/air ratios and b) at constant fuel/air ratio with varying airflows.

## Pressure Fluctuation Measurements

The combustor interior pressure fluctuations are measured by Photocon transducers, mounted at locations slightly displaced from the flow field through an infinite tube assembly. This arrangement is necessary to eliminate contamination by hydrodynamic (turbulence) noise.[3] The photocon transducer can extract signals above 130 dB referred to $2 \times 10^{-5}$ $N/m^2$. The interior pressure measurements are made at two points - one downstream of the primary combustion zone but upstream of the nozzle and the other at the nozzle entrance plane as shown in Figure 5.

The exterior radiated noise is measured by three near field Brüel & Kjaer type 4134, 12 mm condenser microphones at $45^o$, $90^o$ and $135^o$ to jet axis. All the three microphones are situated at a radius 25.5 cm from the combustor exit plane. The reason for choosing near rather than far field is that the latter measurements are contaminated by reflections from ground and nearby constructions. The relative positions of the interior and exterior pressure transducers are shown in Figure 5. All these transducers are calibrated by a Whittaker type PC-125 acoustic calibrator. The near field pressure measurements give

Table 2. Primary Operating Test Conditions

| CASE | AIRFLOW ( KG SEC ) | $\dfrac{\text{FUEL}}{\text{AIR}}$ | CONTRACTION RATIO | REMARKS |
|---|---|---|---|---|
| 1 | 0.18 | 0.016 | 14.6 | Diffuser with separated flow |
| 2 | 0.25 | 0.018 | 12.1 | Diffuser with attached flow |
| 3 | 0.30 | 0.017 | 12.1 | No diffuser |
| 4 | 0.34 | 0.018 | 9.1 | Diffuser with attached flow |
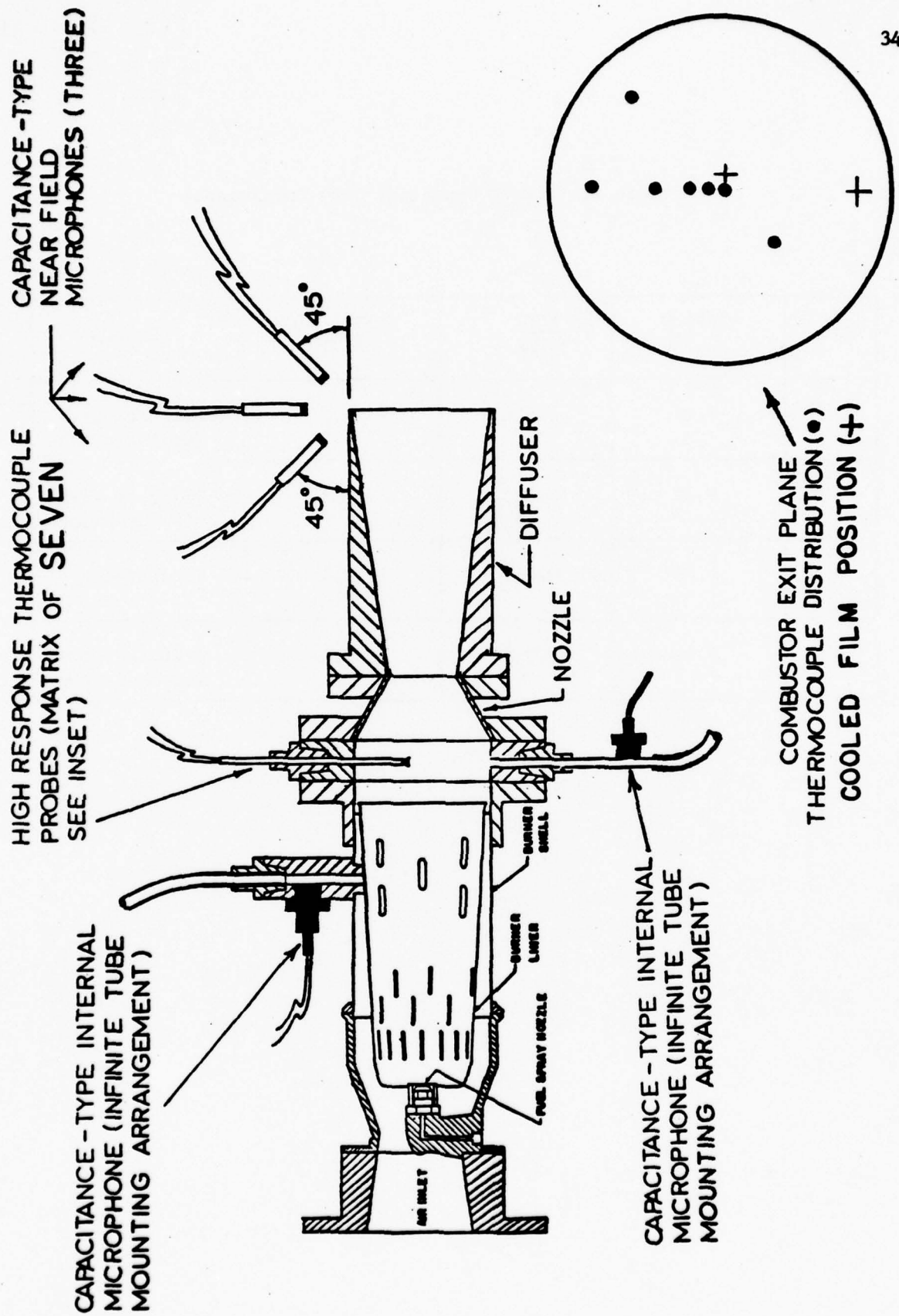
Figure 5. Schematic of the experimental set-up with relative location of the transducers.

HIGH RESPONSE THERMOCOUPLE PROBES (MATRIX OF SEVEN SEE INSET)

CAPACITANCE-TYPE NEAR FIELD MICROPHONES (THREE)

CAPACITANCE-TYPE INTERNAL MICROPHONE (INFINITE TUBE MOUNTING ARRANGEMENT)

45°

45°

DIFFUSER

NOZZLE

BURNER SHELL

BURNER LINER

FUEL SPRAY NOZZLE

AIR INLET

CAPACITANCE-TYPE INTERNAL MICROPHONE (INFINITE TUBE MOUNTING ARRANGEMENT)

COMBUSTOR EXIT PLANE THERMOCOUPLE DISTRIBUTION (●) COOLED FILM POSITION (+)

34

an accurate measurement of acoustic power because of the basically
monopole radiation pattern.[3]

## Temperature Fluctuation Measurements

The entropy noise study requires the details of combustion
generated hot spots; hence, the measurement of temperature fluctua-
tions of hot gases at the burner exit (nozzle entrance) plane have
been carried out using fast response Chromel-Alumel thermocouples.
In the present program, a thermocouple junction constructed from a
wire diameter of 0.025 mm is selected as a compromise between the
conflicting requirements of longevity and response times.

When a thermocouple is used as the primary element for rapidly
fluctuating temperature measurements, the thermal lag of the element,
caused by the slow rate of heat transfer between the element and the
surrounding gas, limits the ability of the element to follow such
fluctuations truly. This thermal lag is quantified by a parameter
called the "time constant" of the thermocouple. The value of the time
constant depends mostly on the properties of the thermocouple junction
and the fluid dynamic environment in which the element is used. It is
important to note that the thermocouple output has to be properly
compensated for its time constant to yield accurate results. This leads
to the additional tasks of determination of thermocouple time constants
and the compensation of thermocouple signals for the time constants.
In an earlier program[3], a new method was developed to find the time
constants under true operating conditions. Also in the present program,

the compensation is done later during data analysis through suitable
modification of the Fourier analyser programming. The details of
this method are described in Ref. (14). Neglecting small variations,
the time constants of the thermocouples used in the present program
are found to be 5 msec.

The temperature measurements of interest to this program are
mean and fluctuating temperatures of hot gases at the burner exit
plane. It is important to note that the entropy noise calculations
require quantities averaged over the burner exit area. The conversion
of single point thermocouple measurements to an area averaged one
demands the knowledge of the spatial distribution of the temperature
fluctuations. It has been found from an earlier program[3] that an
accurate determination of the area averaged temperature requires a
large number of thermocouples to be used at the burner exit plane.
Limited by the availability of data channels, in the present program,
an array of 7 thermocouples has been used. The schematic arrangement
of the thermocouples is shown in Fig. 5.

## Velocity Fluctuation Measurements

The theoretical deduction of various noise source strengths
requires the knowledge of impedance coefficients at the nozzle en-
trance plane. The calculation of these coefficients involve pressure,
temperature and velocity fluctuations. The pressure and temperature
measurement procedures have been described in the preceeding para-
graphs. The velocity fluctuations entering the nozzle were to be meas-

ured by cooled film anemometers. Two such anemometers are positioned at the nozzle entrance plane. The cooled film anemometer is very similar to the hot film one except that the former permits velocity measurements in high temperature environments. In the normal hot wire or hot film anemometer measurements, the temperature of the sensor must be above the temperature of the environment, whereas the cooled film sensor operates below the environment temperature through the addition of a heat sink. The basic theory involved in the cooled film anemometer measurements and the impedance calculation procedures are described in Appendix B. As explained there, these measurements did not work out properly.

## Data Acquisition

The pressure, temperature and velocity fluctuation data have been obtained through the instrumentation scheme shown in Fig. 6. The overall sound pressure levels, registered by microphones, are read out on a Brüel and Kjaer type 2606 microphone amplifier, one at a time. All the pressure transducers, thermocouples and cooled film anemometer signals have been amplified by an array of NEFF type 122 amplifiers and recorded on a PR-2200, 14 channel magnetic tape recorder at a tape speed of 30 ips. The r.m.s. levels of the amplified signals are indicated by a true r.m.s. voltmeter whereas their visual display is available on the oscilloscope screen.
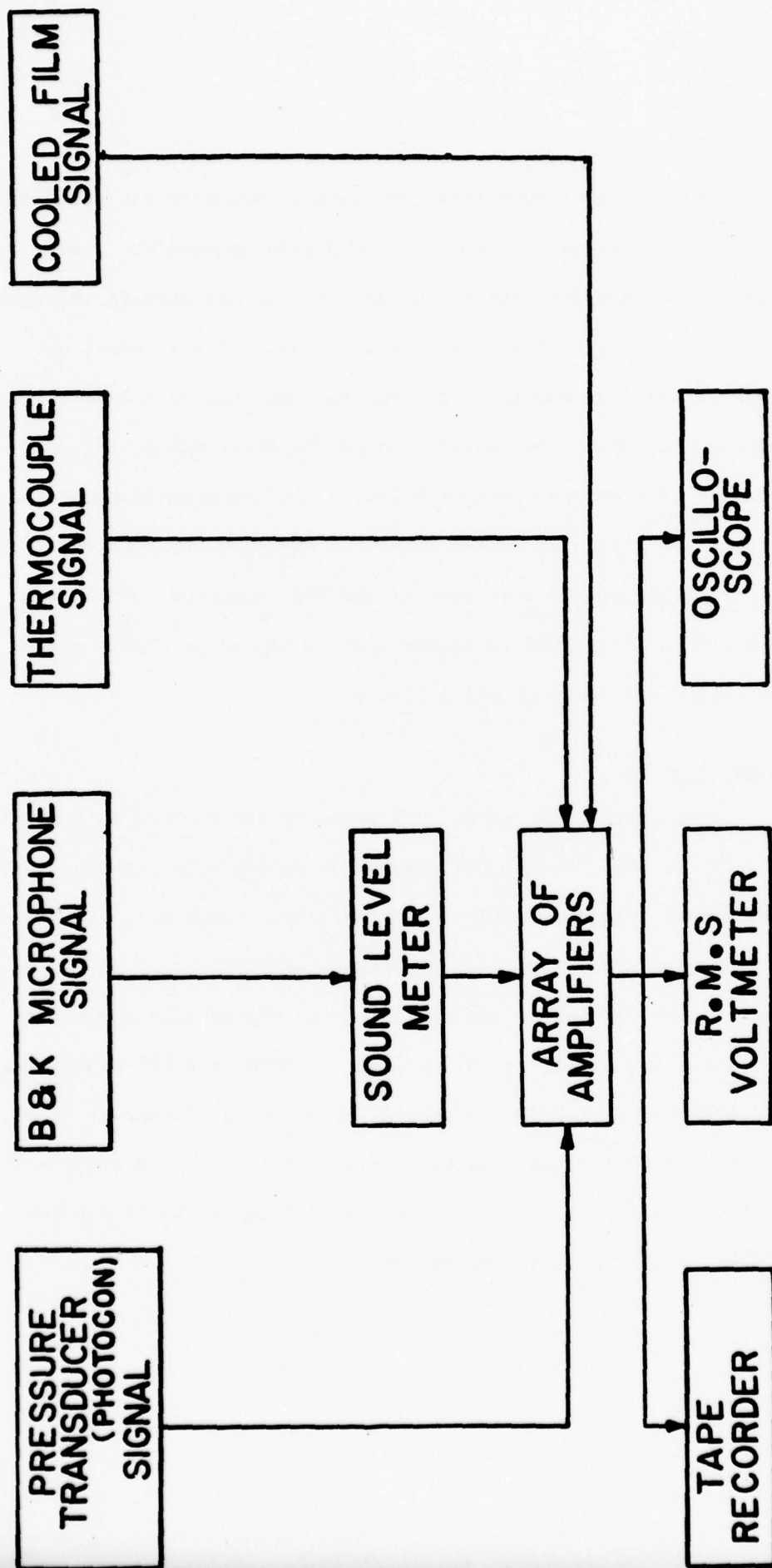
Figure 6. Measurement System Schematic.

## V. Data Analysis Procedures

All data were recorded on a 14 channel FM tape recorder for
later analysis on a Fourier analysis system. The primary quantities
needed are cross spectral data between all interior sensors and the
external microphones and all interior sensors against themselves.

It was determined that the directionality of the exterior
sound was higher than expected on all runs with a general downstream
propagation preferred. The microphone at $90^{\circ}$ to the axis was selected
as the preferred microphone since its reading was usually midway be-
tween the upstream and downstream microphones. Sound power was cal-
culated assuming spherical outward radiation using the $90^{\circ}$ microphone
reading.

The first data check is to determine if there is interior micro-
phone contamination by hydrodynamic noise. This usually only occurs
at very low frequency when there would ordinarily be very high coherence
between the two interior microphones, in the absence of contamina-
tion. Shown in Fig. 7 is a typical coherence obtained. It is concluded
that there was negligible contamination of the interior signals on
all tests. Consequently, the interior theory was deemed valid for use
in extracting source strengths.

However, this high coherence between the two signals caused
some difficulties in reduction of the data at low frequencies. It is
known that the accuracy of multiple coherence estimates degenerates
if the inputs are highly correlated.[9] In fact, the data around
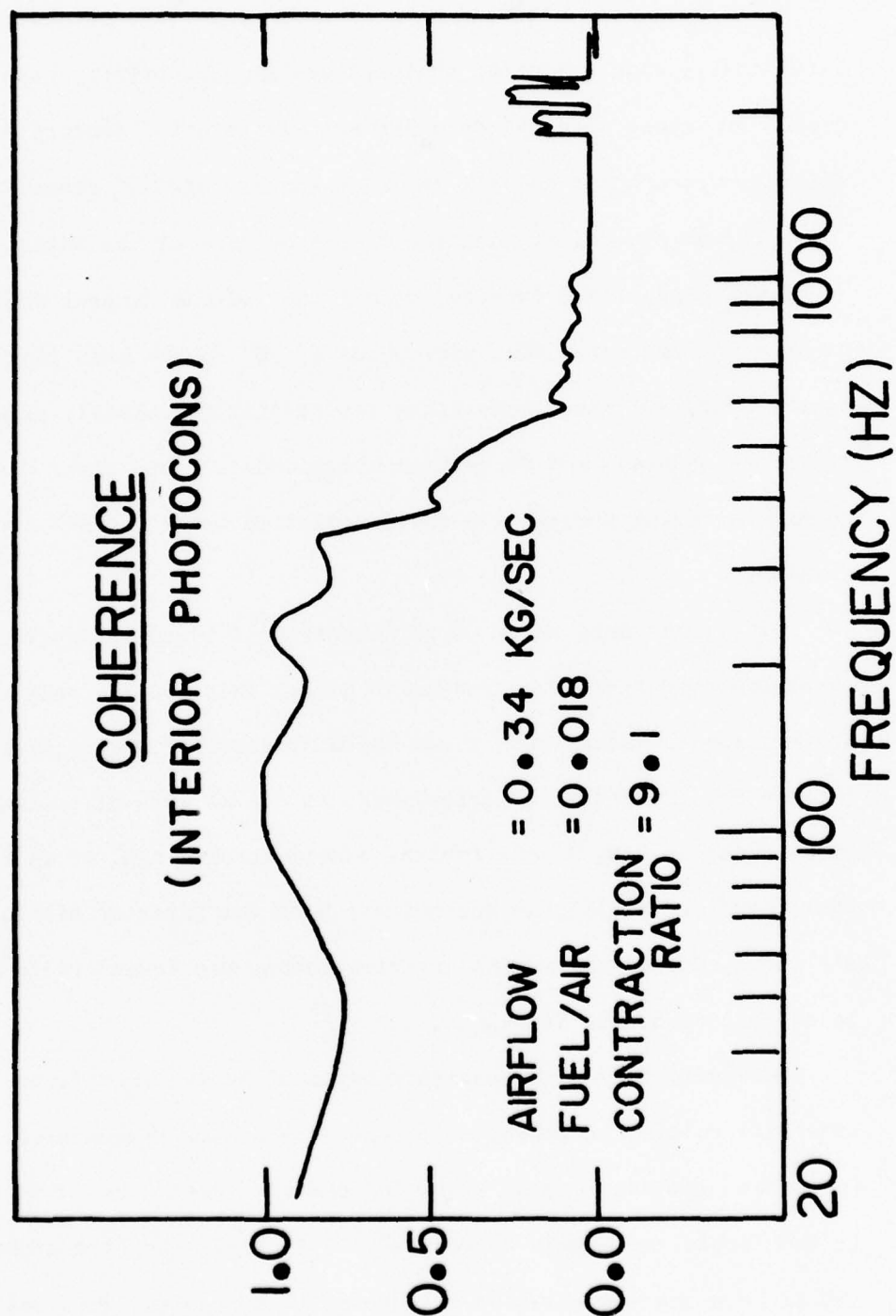100 Hz were lost on all runs because of this problem. This was used

Figure 7. Coherence between interior microphones.

to advantage in the calibration of microphones. The infinite tubes
to the two interior microphones carry different temperature gases,
because of their locations, and could be expected to give different
readings for the same true pressures. The 100 Hz data were used to
generate a correction factor for one of the microphones to bring
the two readings to the same values. This was possible because of
the demonstrated high coherence and the theoretical demand that at
this low frequency there should be no spatial structure to the pres-
sure field.

The magnitude squared of the cross spectra measured  were some-
times quite low, of the order of 0.01 times the product of the two
auto spectra of interest. This routinely happened, for example, when
taking cross spectra between two widely spaced thermocouples or be-
tween a thermocouple and a far field microphone. The accuracy with
which a cross spectrum can be determined is determined by the number
of samples used in the ensemble averaging procedure. For example the
variance in an estimate of $S_{ij}$ , $\sigma_{ij}^2$, is of the order of $S_{ii}S_{jj}/N$,
where N is the number of samples. To extract a cross spectral density
where the magnitude of the variance is of the order of one tenth of
the square of the spectral density of interest is

$$\frac{\sigma_{ij}^2}{|S_{ij}|^2} = 0.1 = \frac{S_{ii}S_{jj}}{N|S_{ij}|^2} = \frac{1}{10^{-2}N}$$

Consequently, N must be of the order of 1000 to have any confidence
in the data measured.

In the first data run 900 averages were taken by a combination of ensemble and frequency averaging. 100 ensemble averages were taken with a frequency bandwidth of 8 Hz. Then 9 adjacent bands were averaged. After the first fully instrumented run, however, it was seen that the multiple coherence was going to be lower than anticipated. Because the inputs are highly correlated at low frequency and the accuracy of multiple coherence estimates drops sharply when this occurs, all following runs were reduced with 7000 averages, made by a 1000 ensemble average with 7 frequency band averages.

Compensation had to be applied to the thermocouples because their response starts rolling off at 6 dB/octave above about 40 Hz. They were compensated by the technique of Ref.(14)where the correction is applied during Fourier analysis rather than by electronic compensation before recording. The rolloff forces an upper frequency limit of about 2500 Hz, above which the electronic noise limit is reached.

The basic measurements were analysed to produce $S_{11}$, $S_{01}$, $S_{x1}$, $S_{oo}$, $S_{xx}$, $S_{ox}$, $S_{\tau 1}$, $S_{\tau \tau}$ , $S_{\tau o}$, and $S_{\tau x}$. However, the measurements involving $\tau$ must be discussed separately since $\tau$ is a cross section average quantity while multiple point measurements were made of temperature. In fact, what was measured and analysed were multiple point cross spectra between individual thermocouples and the other measurements. Consider the construction of $S_{\tau \tau}$ from Eq. (16). It becomes

$$S_{TT} = \frac{1}{A_e} 2 \int dA(\underset{\rightarrow}{x}) \int dA(\underset{\rightarrow}{y}) \frac{S_{t(\underset{\rightarrow}{x}) \ t \ (\underset{\rightarrow}{y})}}{\bar{t}(\underset{\rightarrow}{x}) \ \bar{t}(\underset{\rightarrow}{y})}$$

(22)

The transformation from $\underset{\rightarrow}{x}$, $\underset{\rightarrow}{y}$ to $\underset{\rightarrow}{x}$, $\underset{\rightarrow}{\eta}$ coordinates with $\underset{\rightarrow}{y} = \underset{\rightarrow}{x} + \underset{\rightarrow}{\eta}$ and then shifting to the cylindrical coordinate systems of Fig. 8 yields

$$S_{TT} = \frac{1}{A_e} 2 \left\{ \int_o^a dr \int_o^{2\pi} r d\theta \int_o^{a-r} \rho d\rho \int_o^{2\pi} d\varphi \ \frac{S_{t(r,\theta)t(r,\theta;\rho,\varphi)}}{\bar{t}(r,\theta) \ \bar{t}(r,\theta;\rho,\varphi)} \right.$$

$$\left. + \int_o^a r dr \int_o^{2\pi} d\theta \int_{a-r}^{a+r} \rho d\rho \int_{\varphi_1}^{\varphi_2} d\varphi \ \frac{S_{t(r,\theta) \ t(r,\theta;\rho,\varphi)}}{\bar{t}(r,\theta) \ \bar{t}(r,\theta;\rho,\varphi)} \right.$$

$$\varphi_2 = \pi + \theta + \cos^{-1} z \qquad\qquad z = \frac{\rho^2 + r^2 + a^2}{2\rho r}$$

$$\varphi_1 = \pi + \theta - \cos^{-1} z$$

This complicated formula is simplified first by assuming the temperature cross spectrum and mean temperature is isotropic in $\theta$ and $\varphi$ so they are functions of $\rho$ and $r$ alone. This yields

$$S = \frac{1}{A} 2 \ 4\pi \int_o^a r dr \left\{ \pi \int_o^{a-r} \rho d\rho \ \frac{S_{t(r) \ t(r;\rho)}}{\bar{t}(r) \ \bar{t}(r;\rho)} \right.$$

$$\left. + \int_{a-r}^{a+r} \rho d\rho \ \cos^{-1} z \ \frac{S_{t(r) \ t(r;\rho)}}{\bar{t}(r) \ \bar{t}(r;\rho)} \right\}$$

These integrals are then discretized and numerically evaluated from the data by a very coarse integration scheme. In practice, a pair of
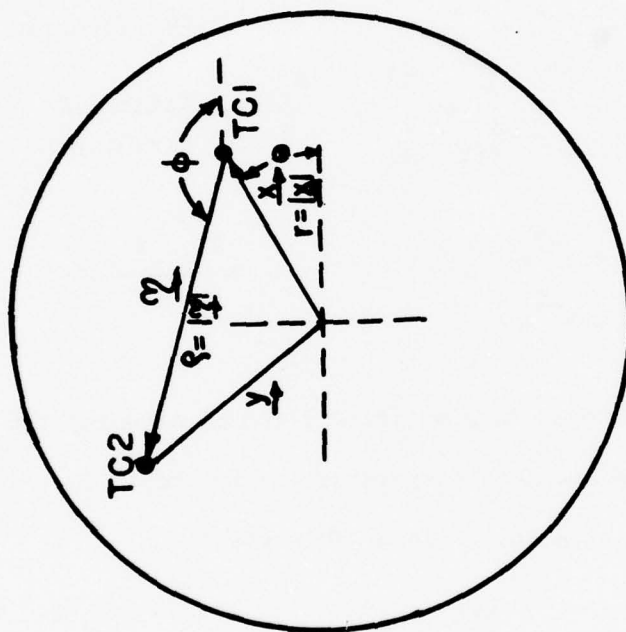
44



Figure 8. Coordinate systems used in analysing the area averaged temperature fluctuation spectrum.

data at the separation distances $\rho$ = 0, 1, 2 and 3 inches is taken.
This is considered a universal curve when normalized by the auto
spectrum at $\rho$ = 0. Consequently, the r value is meaningless and the
r variation has been averaged out. The above equations can be re-
written in the form

$$S_{\tau\tau} = \frac{A_{cor}}{A_e} \; \frac{\overline{S_{tt}}}{\bar{t}^2}$$

where the ratio $A_{cor}/A_e$ , is a rough measure of the area fraction
over which the temperatures are correlated. This computation proce-
dure is illustrated in Fig. 9 for a particular run. Striking in this
figure is the fact that the space-separated temperatures become more
highly correlated at high frequency than at low frequency.

Because of its coarse construction, $S_{\tau\tau}$ is the quantity known
with the least accuracy. By construction, since it is an auto spec-
trum, it must be real. However, at low frequency, two frequency points
were encountered where $A_{cor}/A_e$ were negative, which is impossible.
The magnitude of this negative amount was about .03, giving an esti-
mate of the resolution of the method. When this occurred, $A_{cor}/A_e$
was set equal to zero.

Construction of the cross spectrum of $\tau$ with pressure intro-
duced no special problem. Two points of temperatures were used and
the cross spectra were averaged.

From these data, the spectra $S_{AA}$, $S_{A\sigma}$, $S_{AV}$, $S_{VV}$, $S_{V\sigma}$, $S_{\sigma\sigma}$
are constructed by manipulations on Eqs. (12). $S_{A1}$, $S_{\tau 1}$, and $S_{V1}$,
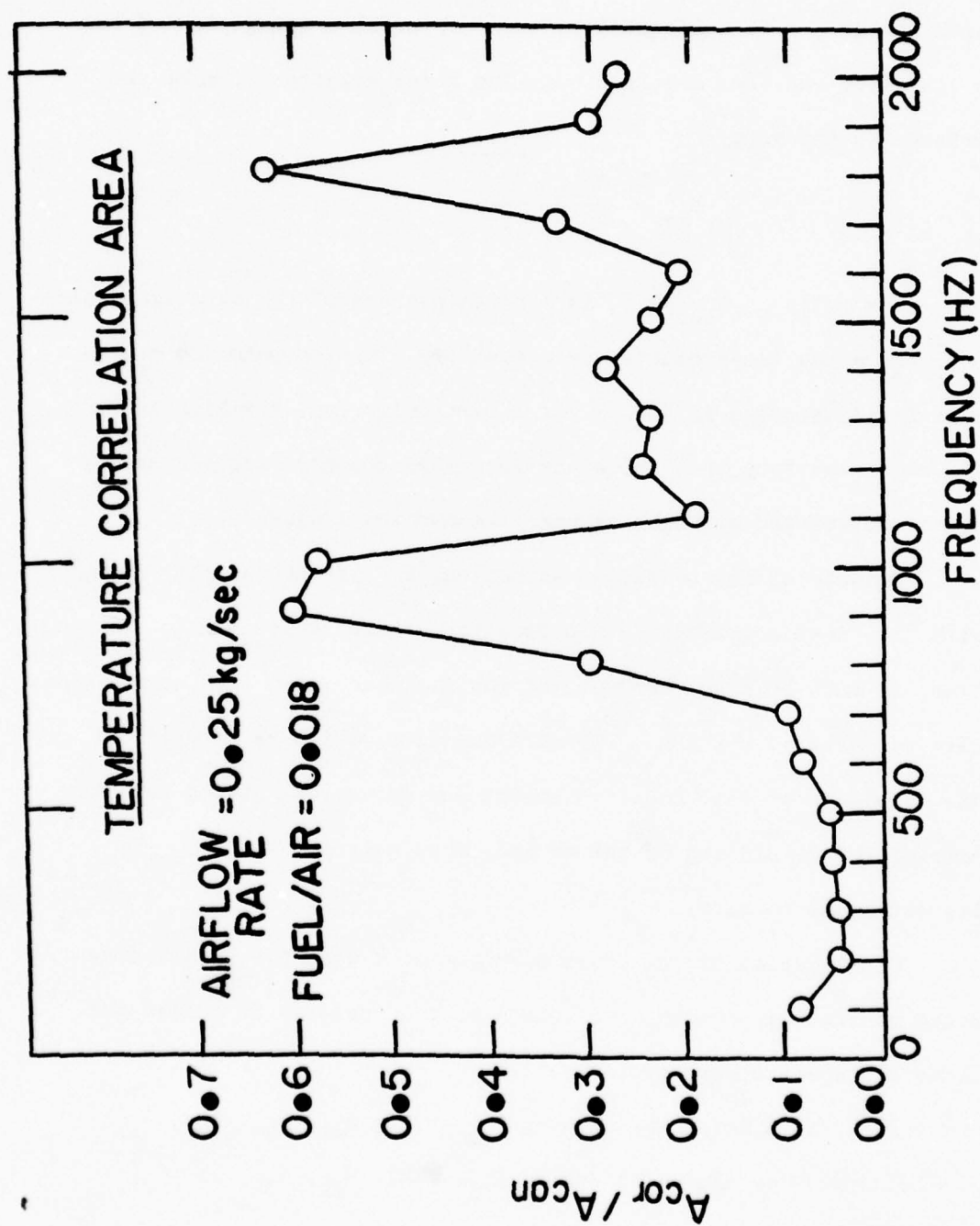
Figure 9. Typical correlation area curve.

needed in Eqs. (18), are also generated by computations from the fundamental data. In the theoretical computations the $a_\omega$, $b_\omega$ and $\beta_w$ values are taken as generated in Section VI. Ordinary coherence functions between all quantities and the multiple coherence function are then computed. The data are checked so that all coherence functions at each frequency must lie between 0 and 1 or else that frequency point is rejected. Data rejection at 100 Hz always occurred. In the first fully instrumented run, some data rejection at 200 and 300 Hz also occurred.

A complete statistical analysis of errors in the measurements and data reduction process was beyond the scope of the program. However, judging from data scatter in the spectral results to follow and knowledge of the accuracy of determination of some of the cross spectral properties leads one to the following judgements: a) sound power results are probably correct to $\pm 1.5$ dB, b) spectral determination of source quantities is probably accurate to $\pm 3$ dB and c) mean square determination of source quantities is probably correct to $\pm 2$ dB. Further discussions of the split of the sound power into various causal elements is deferred until later.

### VI. Admittance and Transmittance Determinations

It has been mentioned in Section II that application of theory to the data reduction process requires knowledge of the admittance coefficients $a_\omega$, $b_\omega$ and $\beta_w$. In prior calculations and tests[3] the effect of $\beta_w$ was found to be small, as long as it is small. It was found $\beta_w \approx 0.06$ was adequate for matching of theory and data and this value will be used here. However, $a_\omega$ and $b_\omega$ have a profound influence on the deduction of the vorticity noise strength and they must therefore be known with some precision. Three methods were used; these were a) theoretical calculations using Candel's theory[15], b) measurements using a combination of cooled film, thermocouple and pressure measurements and c)experiments on a model nozzle in an entropy tube facility. These will be described below.

The diffuser configuration employed was to have accomplished two things; these are a) to drop the jet noise contamination, which it did and b) to act as an impedance matching horn, which it only partially did. The hope was that all acoustic energy passing the choked throat would get out to the far field. Apparently, it did not and the transmission properties of the nozzle diffuser assembly are of interest since they influence the results. Moreover, the transmittances due to entropy and vorticity incident on the nozzle cannot be explained through $a_\omega$ and $b_\omega$ alone because there is continuous generation of reflected and transmitted waves as the incident entropy and vorticity traverse the nozzle. Consequently, the transmittance due to incident

isentropic and entropy waves was looked at in some detail as an aid in interpretation of results.

The theoretical calculations of admittance coefficients follows from Ref. (15) where the mean velocity is assumed linear in distance from the entrance plane to the throat. For one of the nozzles a theoretical calculation is shown in Fig.10. The $b_\omega$ values undergo a monotonic decline in absolute magnitude with an increase in frequency. The $a_\omega$ magnitude undergoes a rise with frequency in the frequency range shown. Actually, as the wavelength becomes comparable to the nozzle length, $|a_\omega|$ would undergo a maximum. However, the frequencies considered in this program are low enough that the behavior of Fig. 10 is all that need be considered. The basic point to be noted is that $|a_\omega|$ and $|b_\omega|$ are small numbers, of the order of the mean entrance Mach number. These low admittance values mean that the nozzle is highly reflective to incident isentropic waves but quite sensitive to incident entropy waves, insofar as creation of pressure waves is concerned. On the other hand, as frequency increases the nozzle becomes a) less reflective to incident isentropic waves and b) less sensitive to generation of pressure by incident entropy waves.

Confirmation of the theoretically expected behavior was given by the results of the entropy tube tests which are fully described in Appendix A. A model nozzle, designed for the same axial Mach number gradient as the hot flow # 2 nozzle, was tested in the entropy tube and bombarded with isentropic and entropy waves. Unfortunately the signal to noise ratio was not good at frequencies above 250-500
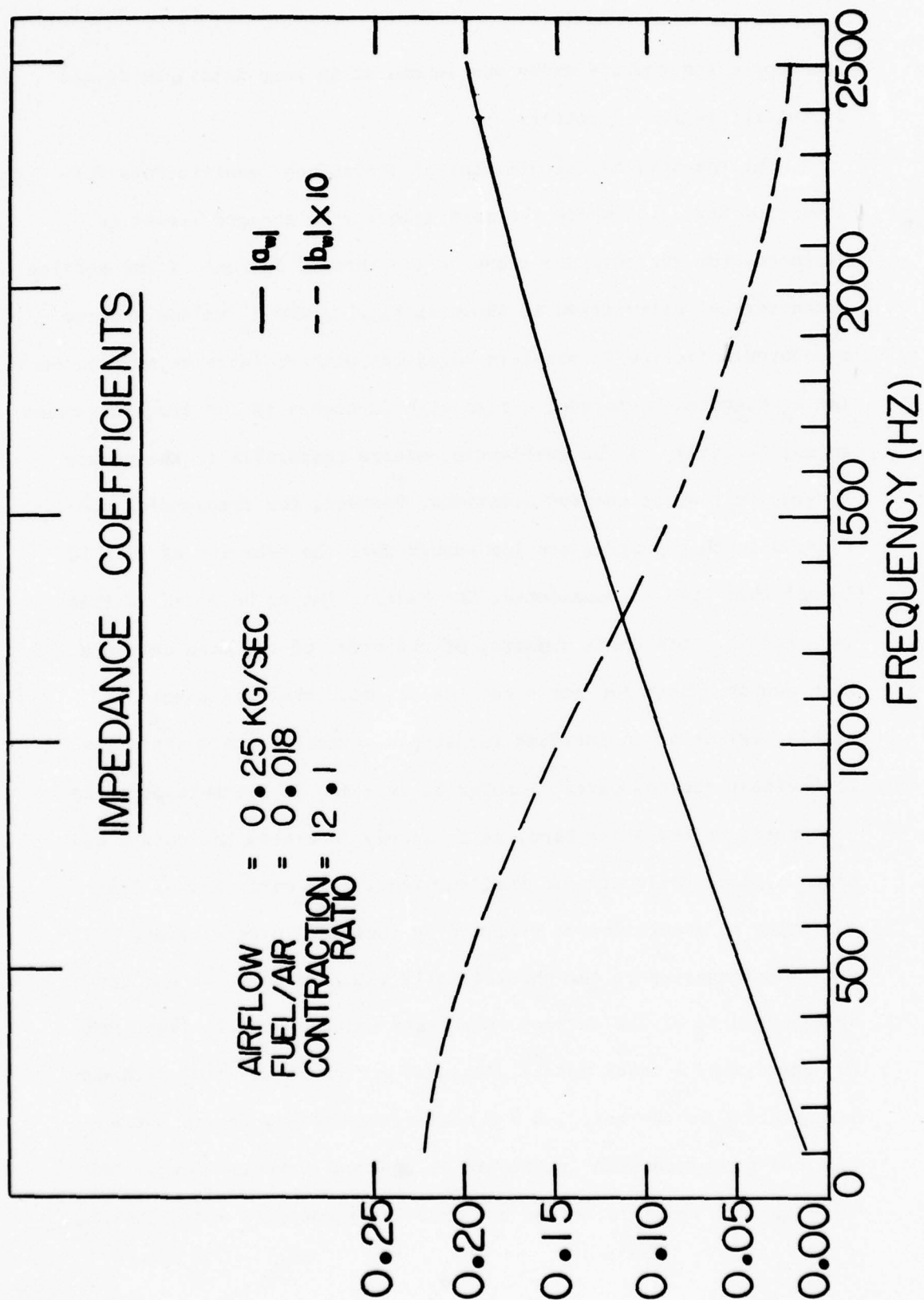
Figure 10. Isentropic and non-isentropic admittance coefficient calculated theoretically for a particular nozzle.

Hz so that the results are relegated to Appendix A. Reference to
Figs. 14 and 22 of that Appendix show the expected trends but
quantitative comparison is not highly satisfactory.

The actual hot flow test nozzle passes a flow which is not
uniform in temperature due to a bypass cooling flow which is at the
wall. Consequently, it was desired to measure the admittance coeffi-
cients directly in the hot flow case. In Appendix B are described
the results of that effort. Unfortunately the claims of the manu-
facturer concerning a piece of instrumentation (cooled film probe)
were shown to be highly inaccurate. As a consequence, the attempted
measurements failed.

Because of the above problems it was decided to use the theo-
retical admittance values in the data reduction procedure. The justi-
fication is through the trends exhibited in the entropy tube results,
the fact that when $|a_\omega|$ and $|b_\omega|$ are low enough they affect the re-
sults in only a minor way, and the fact that nozzles have behaved
well when compared against theory in other programs.[16]

Concerning the transmittance properties of the nozzle-diffuser
combination, Figures 18 and 23 in Appendix A give a feel for what may
be expected. As frequency rises and the isentropic admittance increases,
isentropic waves having an easier time getting through. Thus, it is
expected that the transmittance will rise with frequency. More com-
plex behavior with respect to the entropy transmittance is expected,
however, as the entropy admittance coefficient drops with a frequency
rise, the pressure generation ability of the entropy wave drops. On

the other hand, the transmittance of the generated pressure wave increases. Figure 18 of Appendix A confirms that there are competing mechanisms.

The actual transmittance coefficients in the hot firing were obtained by comparison of external and internal pressures. First, the theory of Eqs. (12) has to be reworked to define the incident pressure pulse, since transmittances are defined in terms of incident and transmitted pulses. The theory as presented in Eqs. (12) gives the complete pressure at a point, consisting of incident and reflected pulses. Decomposing the solution of Eqs. (12) into left and right running waves, the wave incident on the nozzle is given by

$$\frac{Po_i}{\bar{p}(\ell)} = A_\omega H_{Ao_i} + V_\omega H_{Vo_i} + H_{\sigma o_i} \sigma_\omega$$

$$H_{Ao_i} = H_{Ao} (1 + i\alpha_e/K)/2$$

$$H_{Vo_i} = H_{Vo} (e^{-iK\ell}/2 \cos K\ell)$$

$$H_{\sigma o_i} = (b_\omega/M_e) H_{Vo_i} \tag{23}$$

whereas for the transmitted wave Eq. (17) with $Z = 0$ applies. The isentropic transmittance is defined by $T_{i1} = p\omega_1/p\omega_{o_i}$ where only the isentropic part of $p\omega_{o_i}$ is included. Since isentropic waves are produced by the combustion noise

$$T_{i1} = \frac{H_{A1}}{H_{Ao_i}} \frac{\bar{p}(\infty)}{\bar{p}(\ell)} \tag{24}$$

results. Here $H_{A1}$ is measured and $H_{Ao_i}$ is theoretically computed.

For the entropy transmittance coefficient the dimensionless definition

is used $T_{\sigma 1} = \dfrac{p\omega_1/\bar{p}(\infty)}{\sigma_\omega}$ , where one has to be careful here to ex-

clude from $p\omega_1$ components due to the isentropic incident wave caused

by reflections of entropy generated isentropic waves. Doing this,

$$T_{\sigma 1} = - H_{\sigma o_i} T_{i1} + H_{\sigma 1} \tag{25}$$

The quantities of Eqs. (24) and (25) are also generated during

the data reduction process and are shown in Figs. 11 and 12.

$T_{i1}$ shows the striking rise in transmittance with a frequency rise,

as expected, but it does this for both the jet and diffuser termina-

tions. The second feature to note is that the jet transmittance is

substantially lower than for the three diffusers. Consequently, there

is some mechanism, which is not understood at this time, which favors

sound transmittance in diffused flows following a choking point. This

will show up later as a sound level significantly higher than can be

explained by the correlation efforts of Section III. The increase in

transmittance with frequency is characteristic of an impedance match-

ing horn, but the jet effect is not understood.

As expected from Appendix A, Fig. 12 shows no particularly strik-

ing behavior for the entropy transmission coefficient. The jet again

shows a depressed transmittance curve with a shape which is similar

to the nozzle-diffuser curves.

In Figs. 11 and 12 only magnitude has been presented since
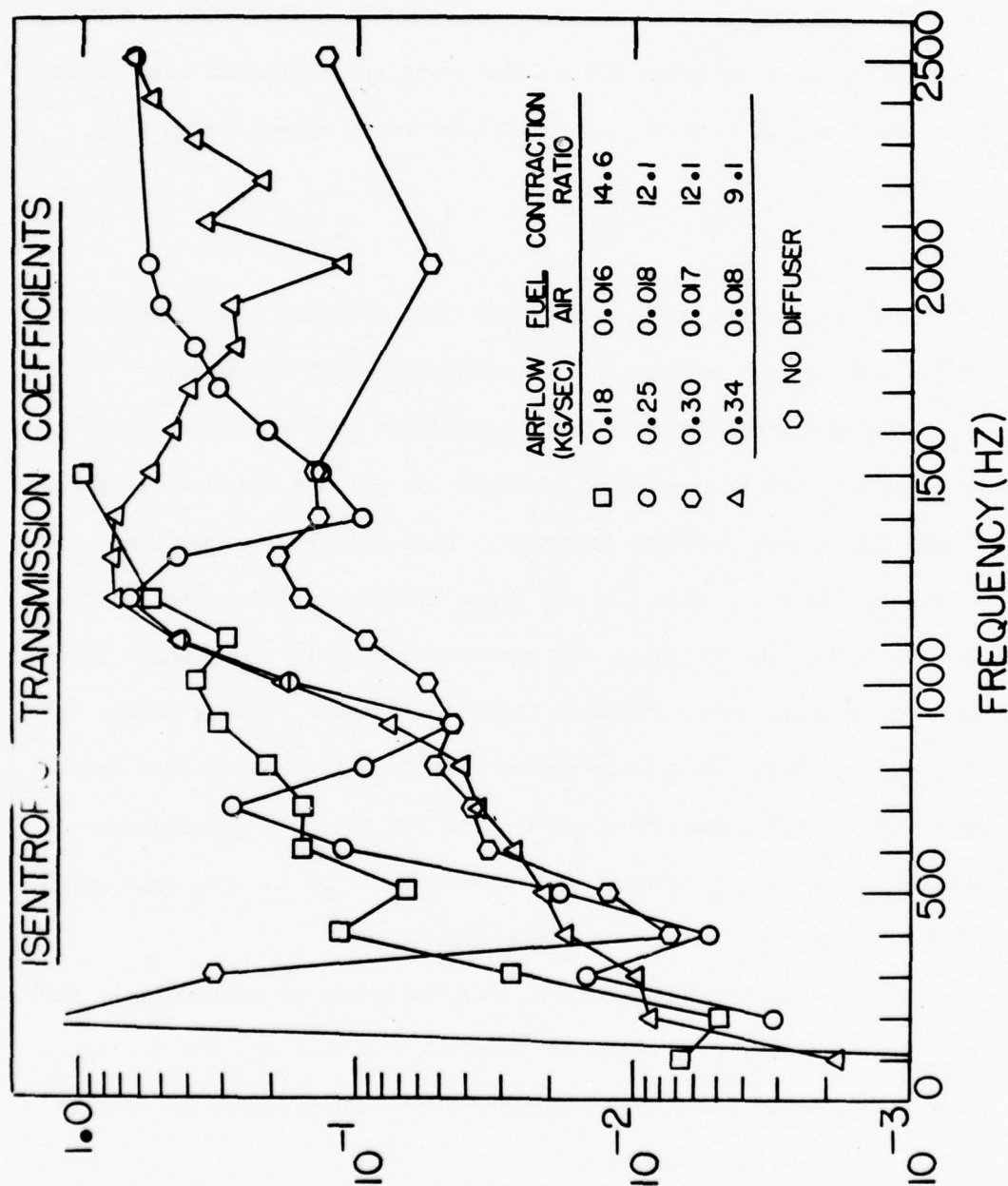
Figure 11. Isentropic transmittance coefficients for the four fully reduced runs.

54
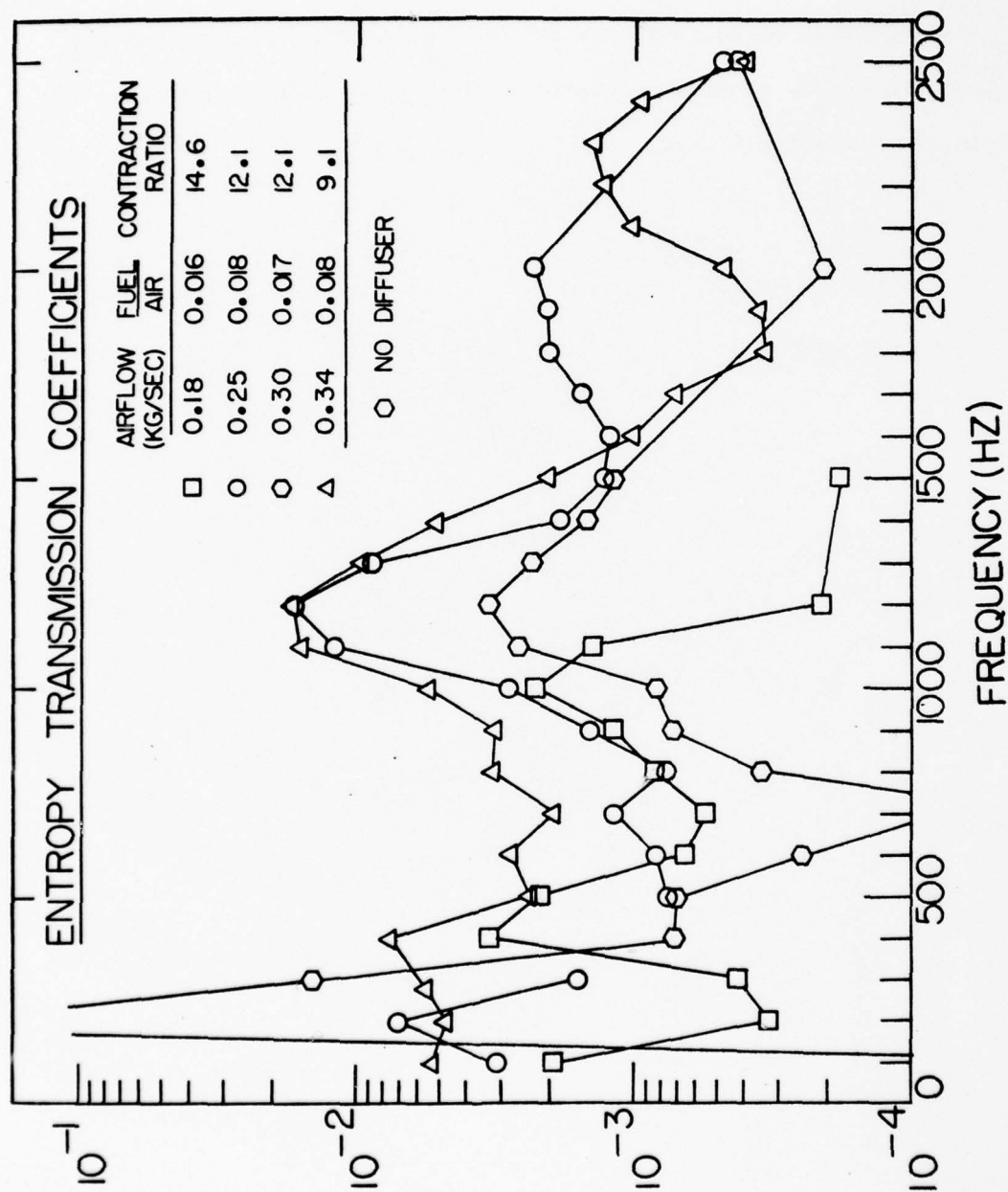
Figure 12. Entropy transmission coefficients for the four fully reduced runs.

phase information depends upon the distance between the source and
receiver points. The vertical scale also should be viewed on a rela-
tive magnitude basis since the absolute magnitude depends upon the
location of the exterior microphone. Only the shape on the frequency
plot is of interest here.

## VII. Experimental Results

### Source Identification

The spectral results to be presented are two-sided spectra corrected to a 100 Hz bandwidth. Consequently, the mean square value of a quantity may be obtained by band summation, and then multiplication by 2. Moreover, the spectra are always of normalized quantities so that mean square values are really fractional mean square quantities.

Shown in Fig. 13 is a typical auto spectrum of an interior microphone and in Fig. 14 is shown a typical compensated thermocouple spectrum. The microphone resonances correspond to the nearly-closed-end longitudinal resonances in the vicinity of 800, 1600, etc. Hz. In addition there is a peak near 100-200 Hz which has a counterpart in the thermocouple spectrum; this is perhaps the entropy wave-acoustic wave resonance which was shown to exist in Ref. (3). The thermocouple spectrum is not "closed" in the sense that there is high confidence that the area under the curve will give the mean square value of the relative temperature fluctuation. However, over the range of frequencies shown the rms fluctuation is of the order of 12-13% of the mean temperature. Recall, the reason higher frequencies are not shown is that above 2500 Hz the thermocouple output is in the electronic noise. This will not, however, affect any of the conclusions of the work. In Fig. 13, the rapid falloff with frequency is expected to yield a rapidly diminishing combustion noise source strength, in accordance with Eq. (15). This will indeed be found to be the case.
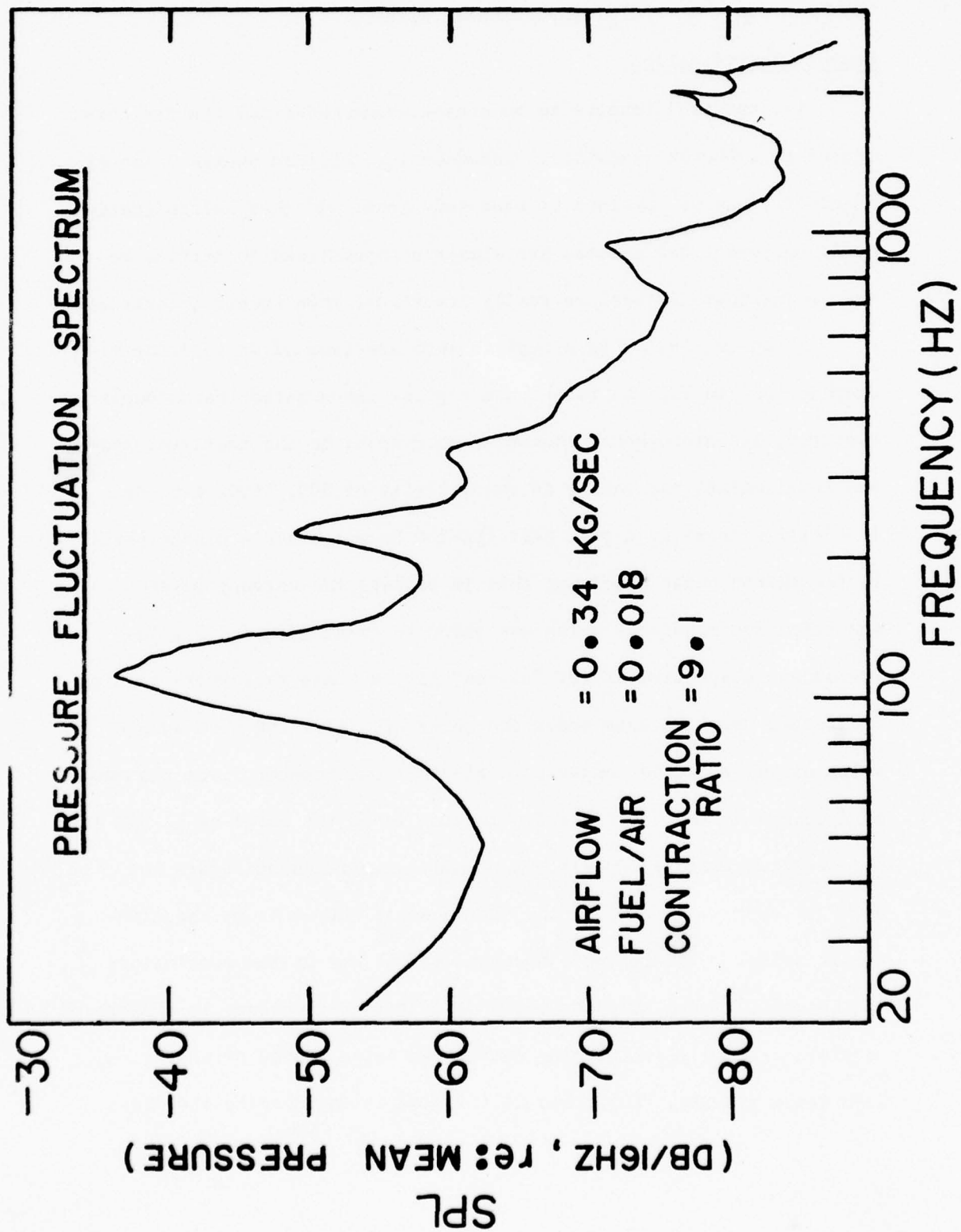
Figure 13. Auto spectrum of an interior microphone.
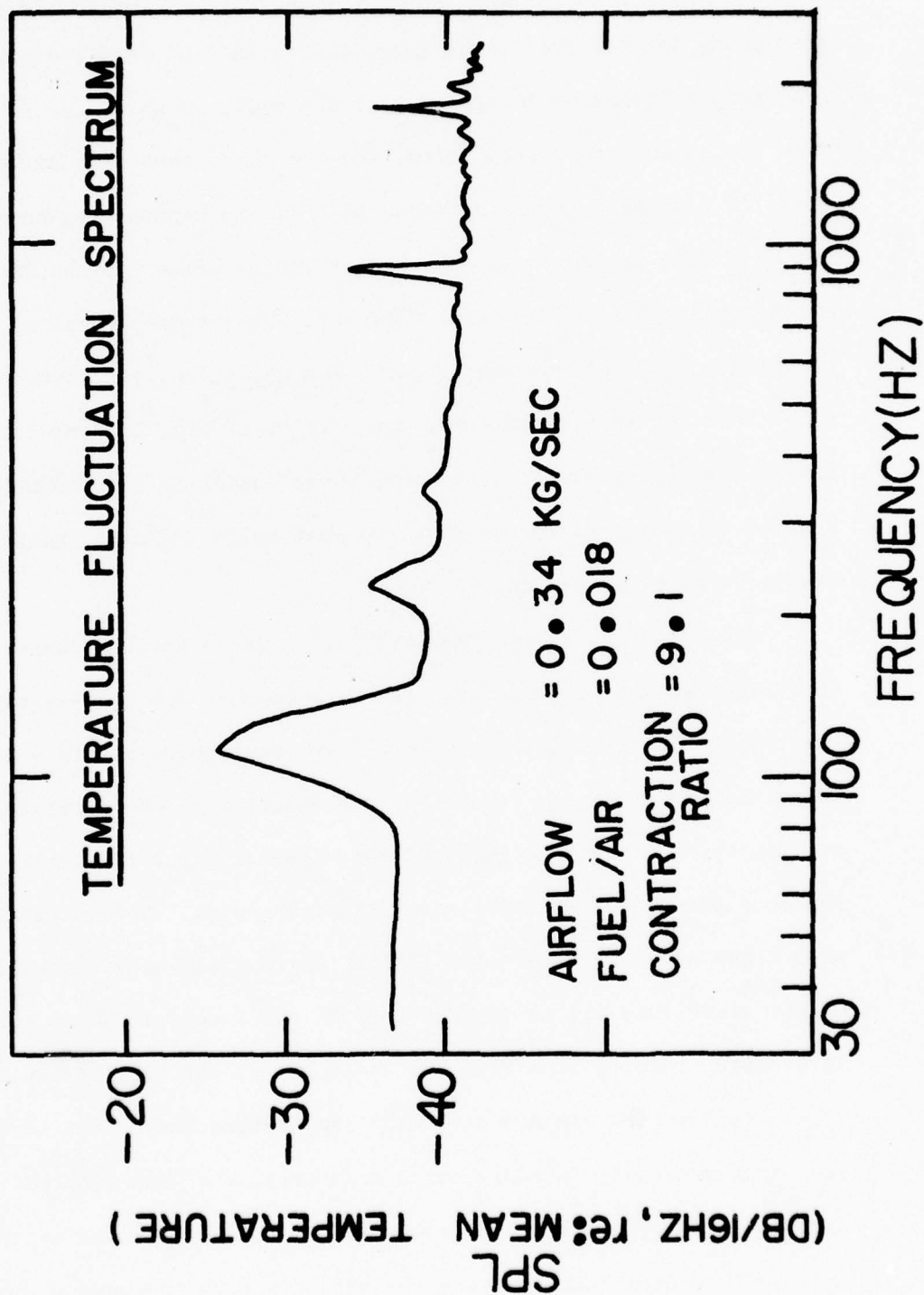
Figure 14. Auto spectrum of an exit plane thermocouple.

In Fig. 15 are displayed the auto spectra of the 90$^o$ exterior microphone for the four basic runs. The extent and detail of the high frequency information increased with the order in which the runs were made for reasons explained later. For the three runs with diffusers there is a general level increase and shift to higher frequencies as the mass flow is increased. The most striking effect is the depression of the noise when there was no diffuser. The jet-only spectrum is still climbing at 2500 Hz because of jet noise masking of the combustion noise results, as will be seen. The spectra of Fig. 15 contains noise from all possible sources, not just those inside of the combustor; Fig. 15 is merely raw noise data and must be corrected to obtain noise caused by interior sources.

Shown in Fig. 16 are the correlation areas for the temperature fluctuations. Recall these are needed to compute the area-average of the temperature fluctuations. There were two problem points - at 300 Hz on the first run and at 400 Hz on the last run the correlation area was negative, which is a physical and mathematical impossibility and reflects the use of a coarse net of thermocouples. These problem points will cause spurious results to follow, but overall will cause little effect since they are in but one band of the spectrum. There are two interesting results from Fig. 16. These are a) the correlation area "resonates" at the can acoustic mode frequencies and b) the correlation area generally increases with frequency. The resonance was expected since the temperature fluctuation is made up of two parts - one due to random hot spots and the second due to the wave motion in
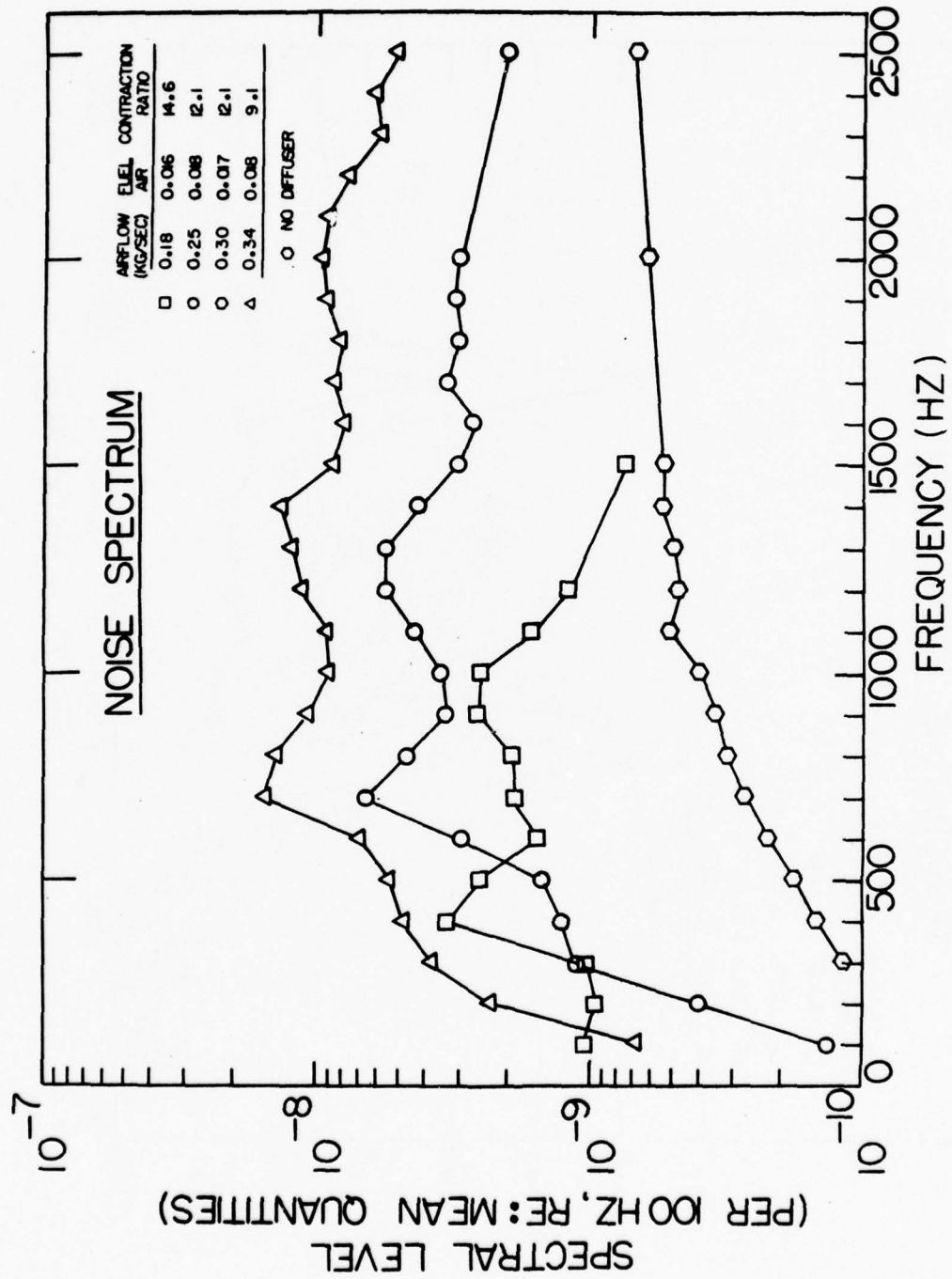
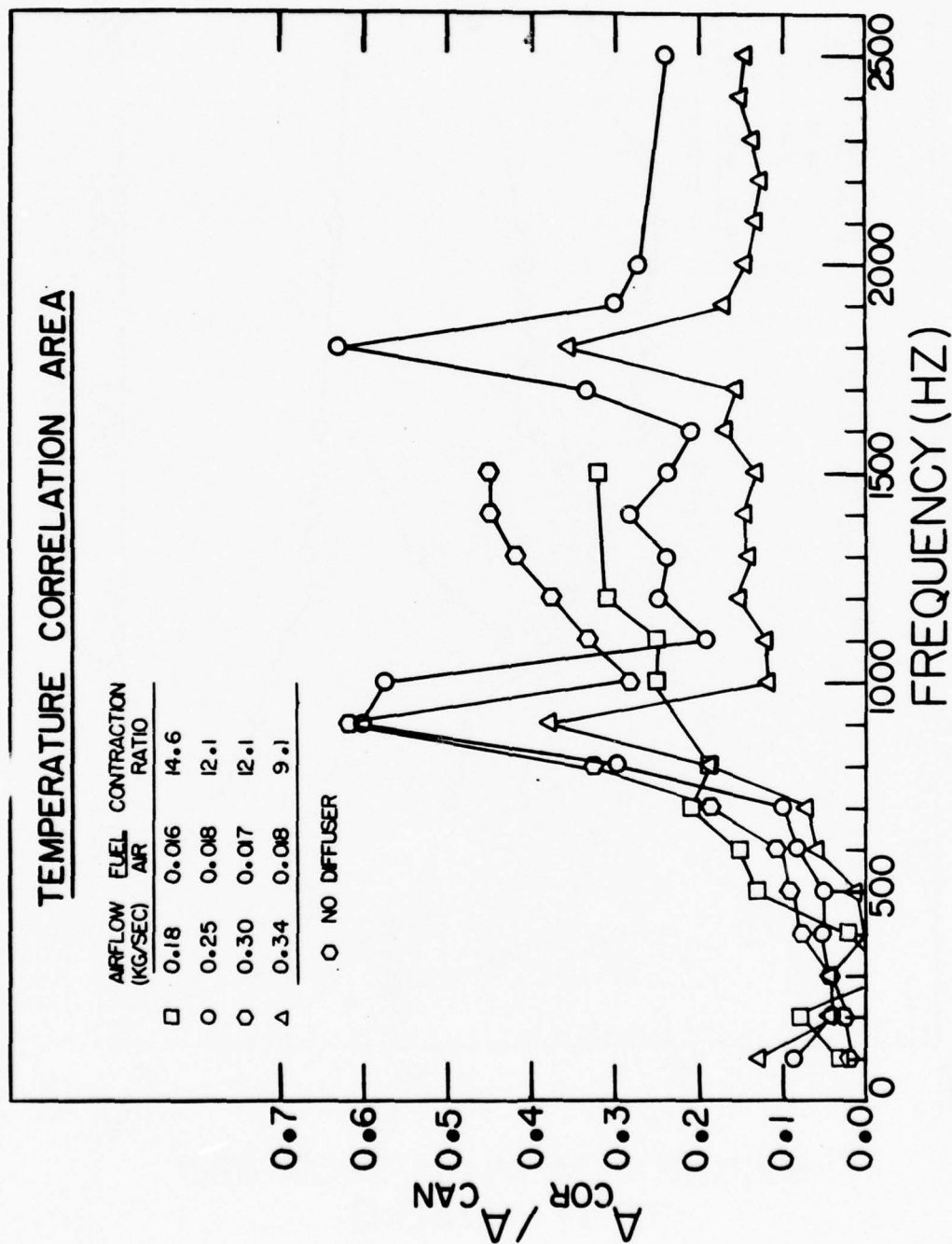Figure 15. Auto spectra of the 90° Exterior microphone for the four basic runs.

Figure 16. Temperature correlation areas for the four basic runs.

the can. The wave motion, being basically a plane wave, is correlated over the entire can diameter and dominates the temperature fluctuation at resonance. The general rise with frequency, however, is surprising. One generally associates higher frequencies with smaller hot spots. This result suggests that although the longitudinal length scale may decrease with an increase in frequency the lateral scale increases. Within the limits of data scatter expected, all curves of Fig. 16 are believed consistent. There was no difference expected between the runs for the correlation area with only a factor of 2:1 variation in mass flow.

Shown in Fig. 17 are the multiple coherence functions for the four basic runs. It is this function which shows the fraction of noise on Fig. 15 which is linearly, causally related to the interior sources. There is a general rise in coherence with frequency, except for the nozzle-only case which had heavy jet noise masking at high frequency. In any event at low frequency there is always relatively poor multiple coherence indicating a) nonlinear behavior, b) measurement noise or c) the presence of other, unaccounted for, sources. However, the multiple coherence level is of such magnitude that there is statistical confidence in the results, even at low frequency. While it only has meaning as an indicator of average coherence, the band summation averages of the multiple coherence are 0.28, 0.35, 0.14 and 0.27, in the order of increasing mass flow.

The coherent noise spectrum is obtained by multiplying the results of Fig. 17 by the results of Fig. 15. The results are shown in
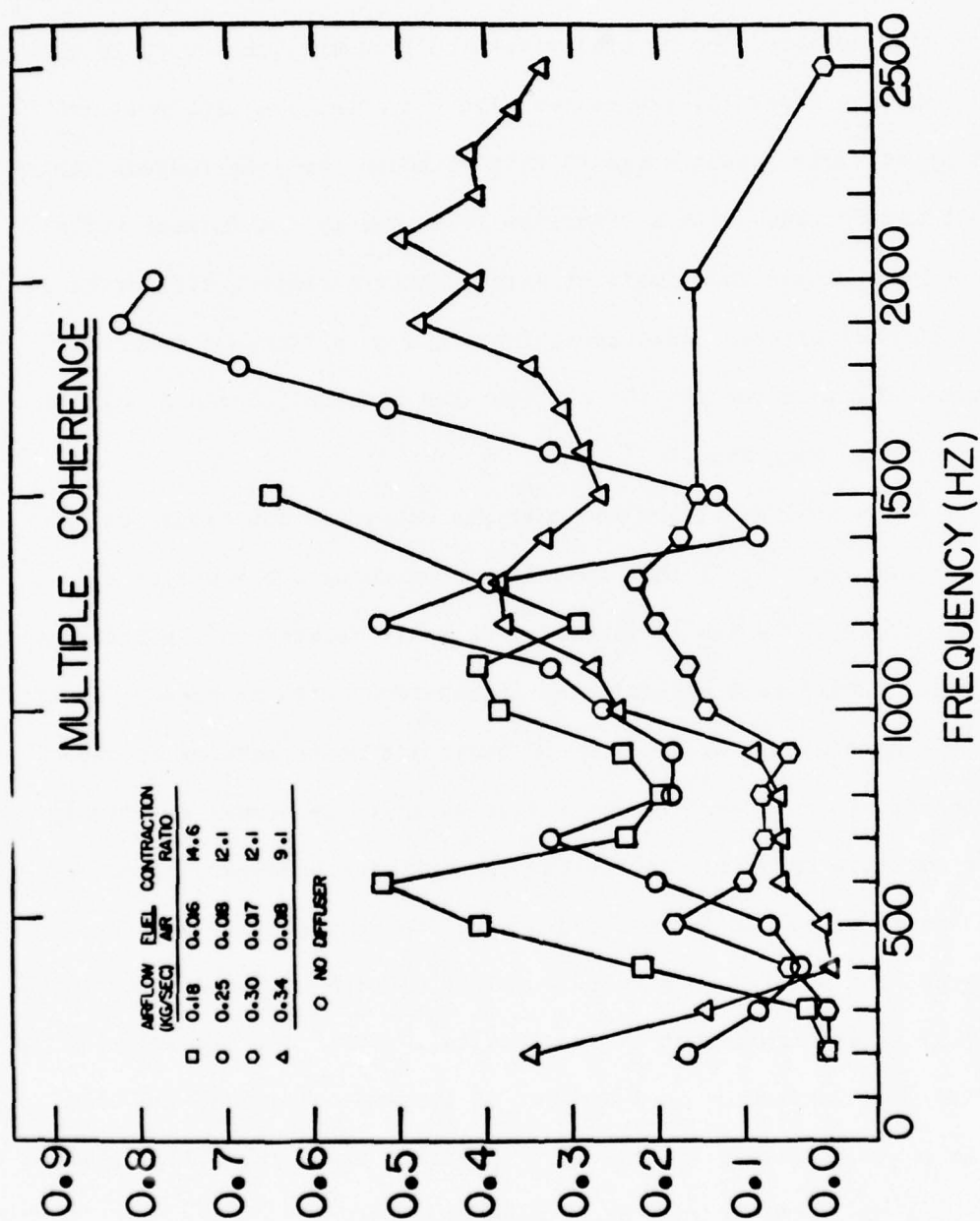
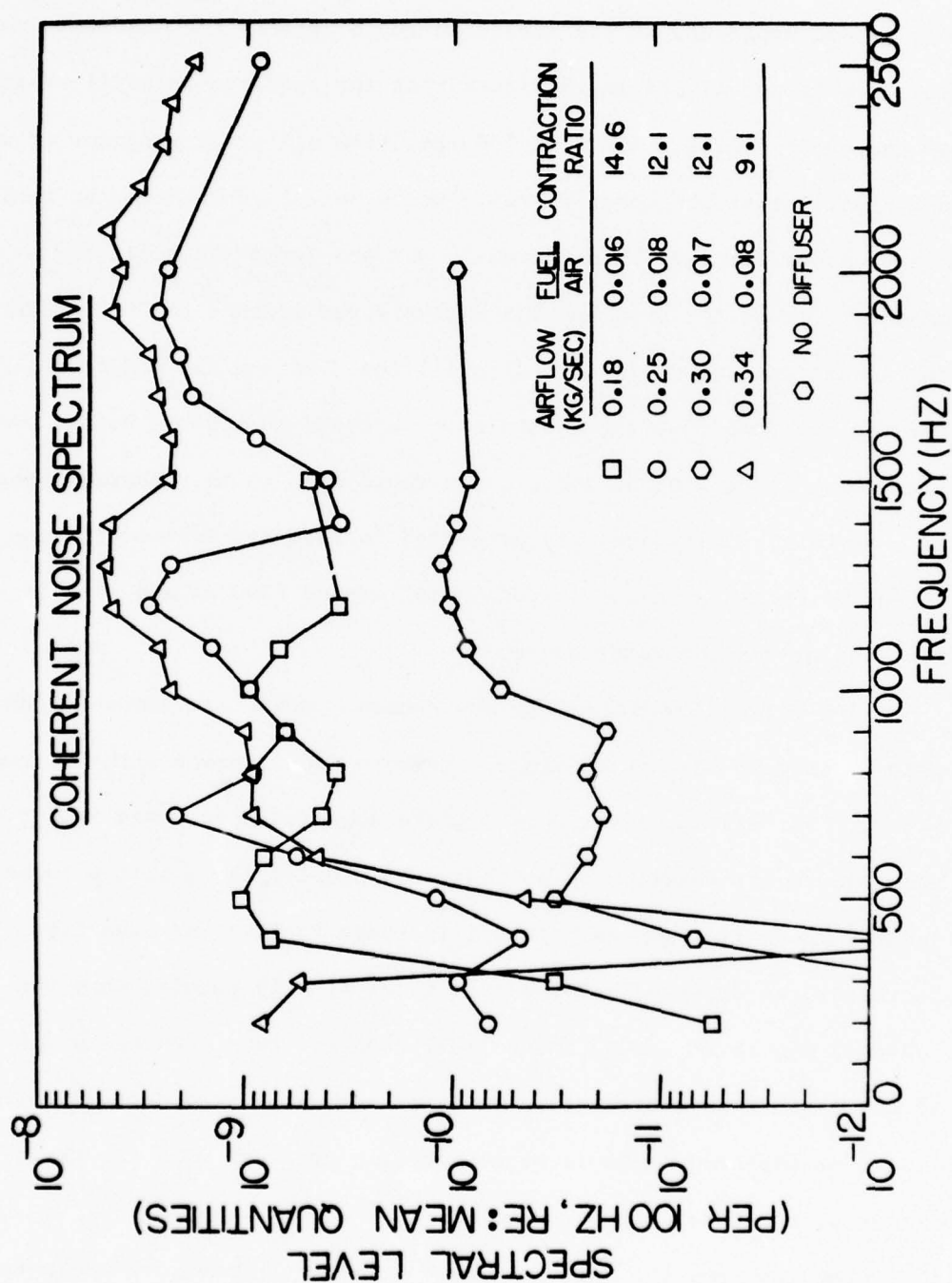Figure 17. Multiple coherence function for the four basic runs.

Figure 18. Coherent noise spectra of the 90° microphone for the four basic runs.

Fig. 18. The reason for the ever-widening frequency range of the analysis is now apparent. In the first run (0.18 kg/sec) the coherent noise spectrum is not closed in the sense that the spectrum is still rising at the upper analysis limit of 1500 Hz. From all prior programs it was anticipated that the coherent noise would be well down from the maximum by about 1000 Hz. This did not occur and forms the basis for a major result of the program. The analysis was widened to 2000 Hz for the second run (no diffuser) but still the spectrum did not close. For the last two runs the analysis was widened to 4000 Hz but it was found that above 2500 Hz there was a rapid drop in the coherent spectrum so that results are only presented to 2500 Hz. Most of the coherent noise is contained in the "hump" around 2000 Hz and this is a new finding for combustor noise.

The data below 500 Hz for the coherent noise are somewhat suspect because of the low multiple coherence and problems with the temperature correlation area. However, the low frequency range is not the major noise contributor so that this problem is of little consequence. There is a general overall increase in level as mass flow increases, as expected and the results of Fig. 15 persist that the jet-only run is at a much lower level than the runs with the diffuser. If the basic source strength within the combustor remain relatively fixed, as expected, this level change is consistent with the transmittance results of Figs. 11 and 12.

Consider now the derived source strengths. These are the auto spectra $S_{AA}$, $S_{\sigma\sigma}$ and $S_{vv}$. They are presented in Figs. 19-21. $S_{AA}$
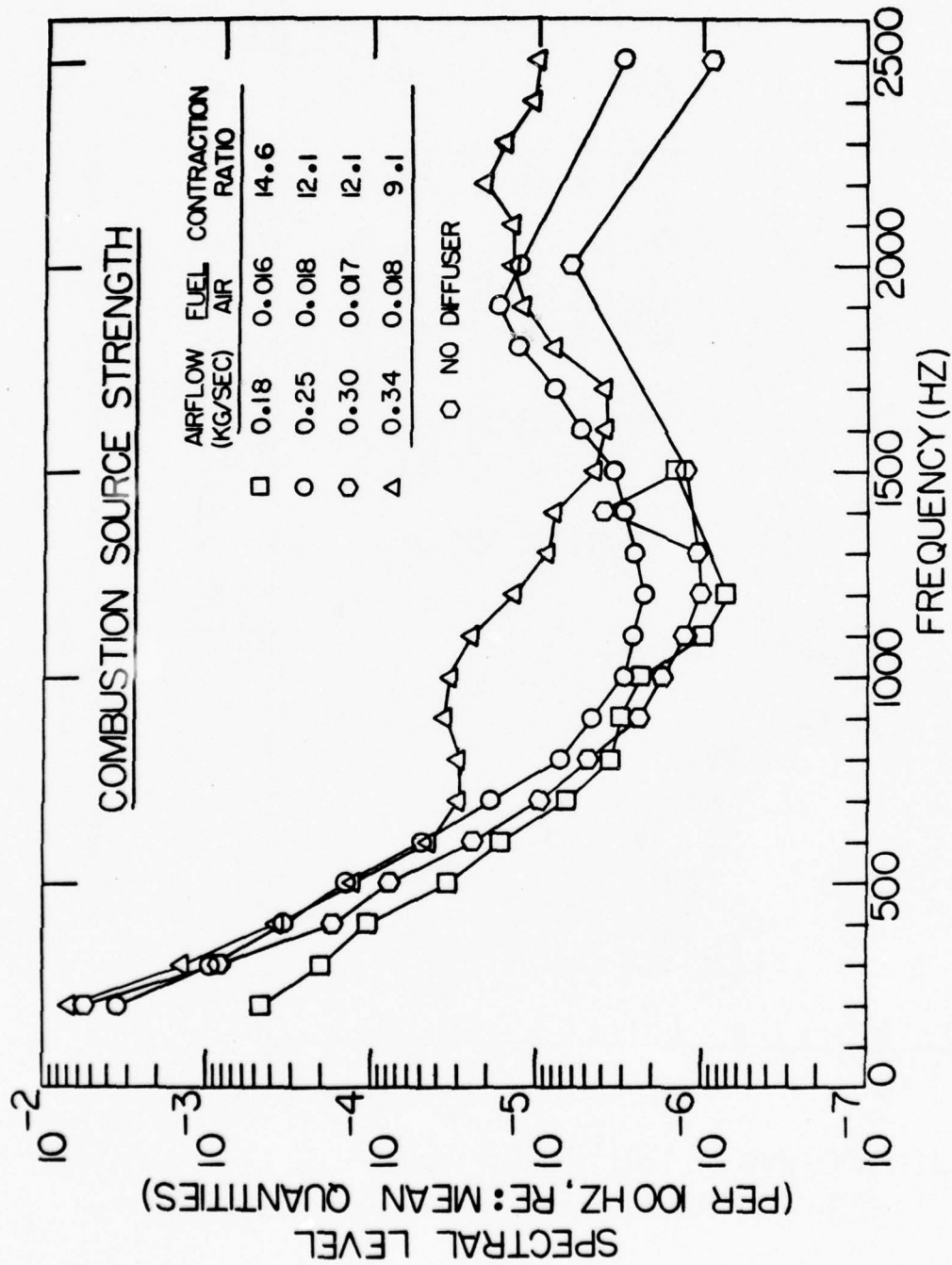
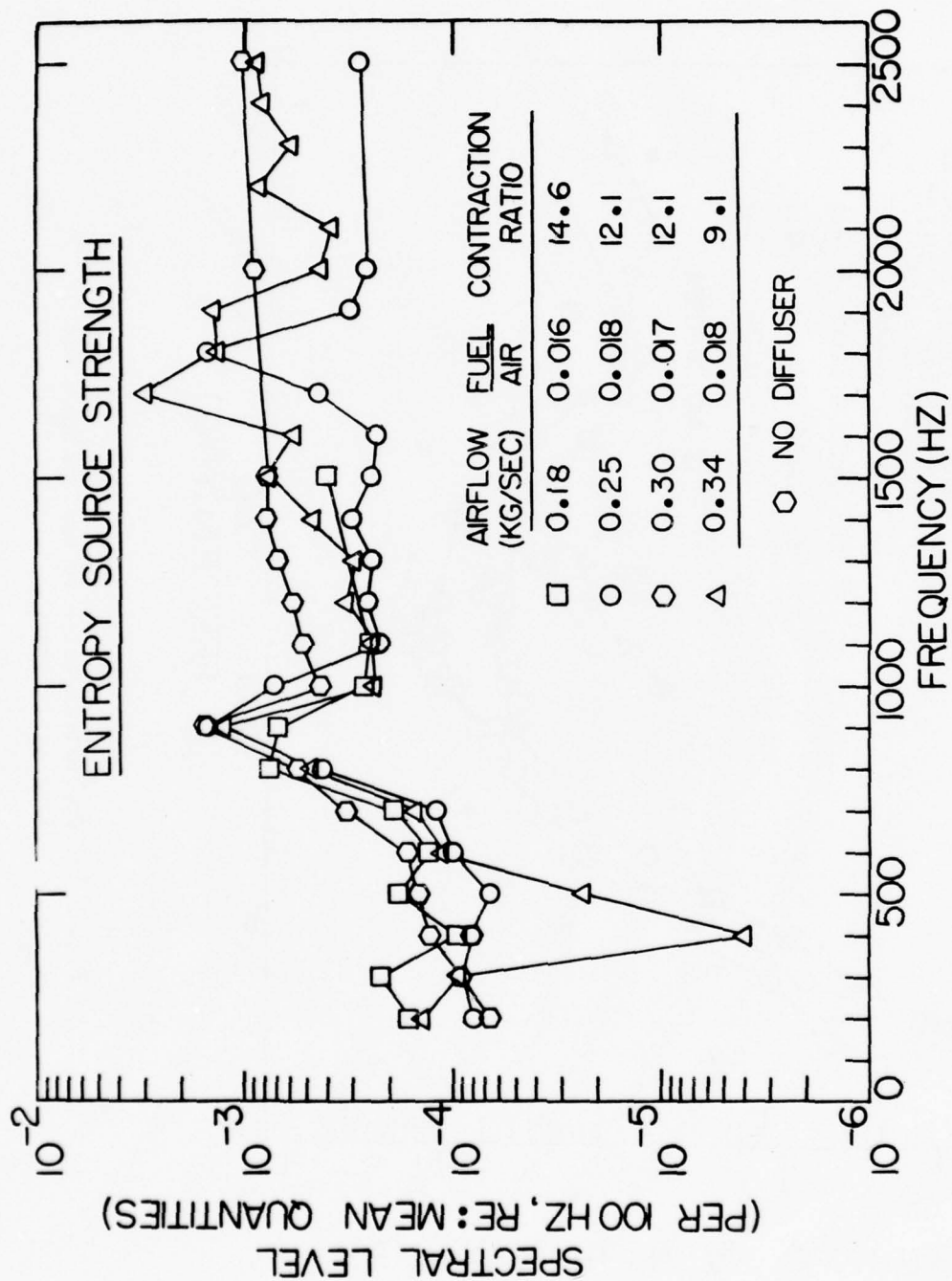Figure 19. Combustion noise source spectrum for the four basic runs.

Figure 20. Entropy noise source spectrum for the four basic runs.
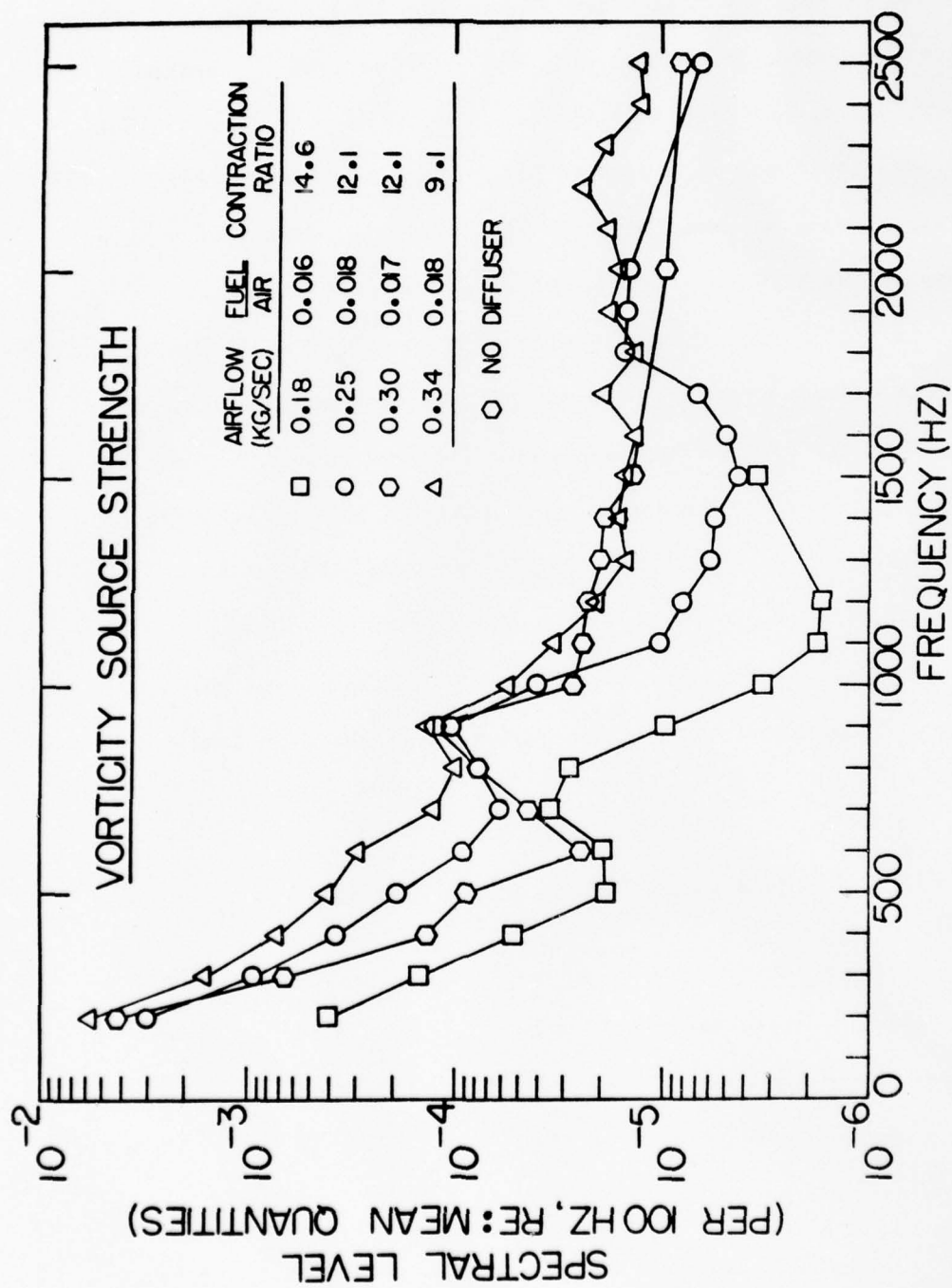
Figure 21. Vorticity noise source spectrum for the
four basic runs.

has a maximum at low frequency, rapidly falls then has a hump around

2000 Hz. The major contribution to the mean square value of A comes

at low frequency. In a prior program[3] the derived $S_{AA}$ peaked at

200 Hz, but recall here that the data at 100 Hz were lost so that

this fact could not be confirmed here. The same general trend holds

for all curves, as expected, with the only major discrepancy being

a hump in the high mass flow spectrum around 1000 Hz.

In Fig. 20 the entropy source strength, $S_{\sigma\sigma}$, is displayed and

there is high consistency between runs, as expected. In Fig. 21, $S_{vv}$

shows the same general trends between the four runs, but there is an

increase in overall level with an increase in mass flow. While $S_{\sigma\sigma}$

is relatively flat, $S_{vv}$ shows roughly the same behavior as the $S_{AA}$

curves of Fig. 19.

The overall behavior of the mean square values of the source

strength is obtained by band summation and is shown in Table 3.

Table 3

Mean Square Values of the Interior
Source Strengths

| Run | $<A^2>$ | $<\sigma^2>$ | $<V^2>$ |
|---|---|---|---|
| 0.18 kg/sec - diffuser | $1.73 \times 10^{-3}$ | $8.26 \times 10^{-3}$ | $1.45 \times 10^{-3}$ |
| 0.25 kg/sec - diffuser | $1.02 \times 10^{-2}$ | $1.65 \times 10^{-2}$ | $1.01 \times 10^{-2}$ |
| 0.34 kg/sec - diffuser | $1.80 \times 10^{-2}$ | $2.98 \times 10^{-2}$ | $1.76 \times 10^{-2}$ |

In Table 3 there is a clear trend for the mean square values of the

source strengths to rise with mass flow, which was not expected in the theory of Section II. As an example $<\sigma^2> \propto \dot{m}^2$. This kind of a trend is apparent in the bottom two entries for $<A^2>$ and $<V^2>$. However, the first entry for these two quantities indicates a stronger dependence. On the other hand, $<A^2>$ and $<V^2>$ are highly influenced by the low frequency portions of the spectrum (see Figs. 19 and 21) where the data is least accurate and where there is little coherent noise output. At higher frequencies there is less of a difference between the first and last runs. Because of the relative insensitivity of $S_{\sigma\sigma}$ to frequency the deduction of the $\dot{m}^2$ dependence is preferred for all source strengths. This would bring the theory in closer line with the empirical correlation of Section III, although the physics of why this trend occurs is unclear. At any rate, this interpretation will be accepted and the conjecture of Section III that the additional dependence of power on $u_{ref}$, as compared with theory, is due to aerodynamic noise contamination will be dropped.

Now the question arises as to the separability of the coherent noise into components due to the various sources. The first bit of damning evidence comes from Fig. 22, where the ordinary coherence between sources is calculated. First of all, at low frequencies all sources are highly coherent with each other. This was expected between entropy and combustion noise from Ref. (3), but it is now shown to include vorticity as well. At the higher frequencies ($>$ 2000 Hz) there is an exceedingly high coherence between the combustion and vorticity sources. In the mid range there is often a high coherence between
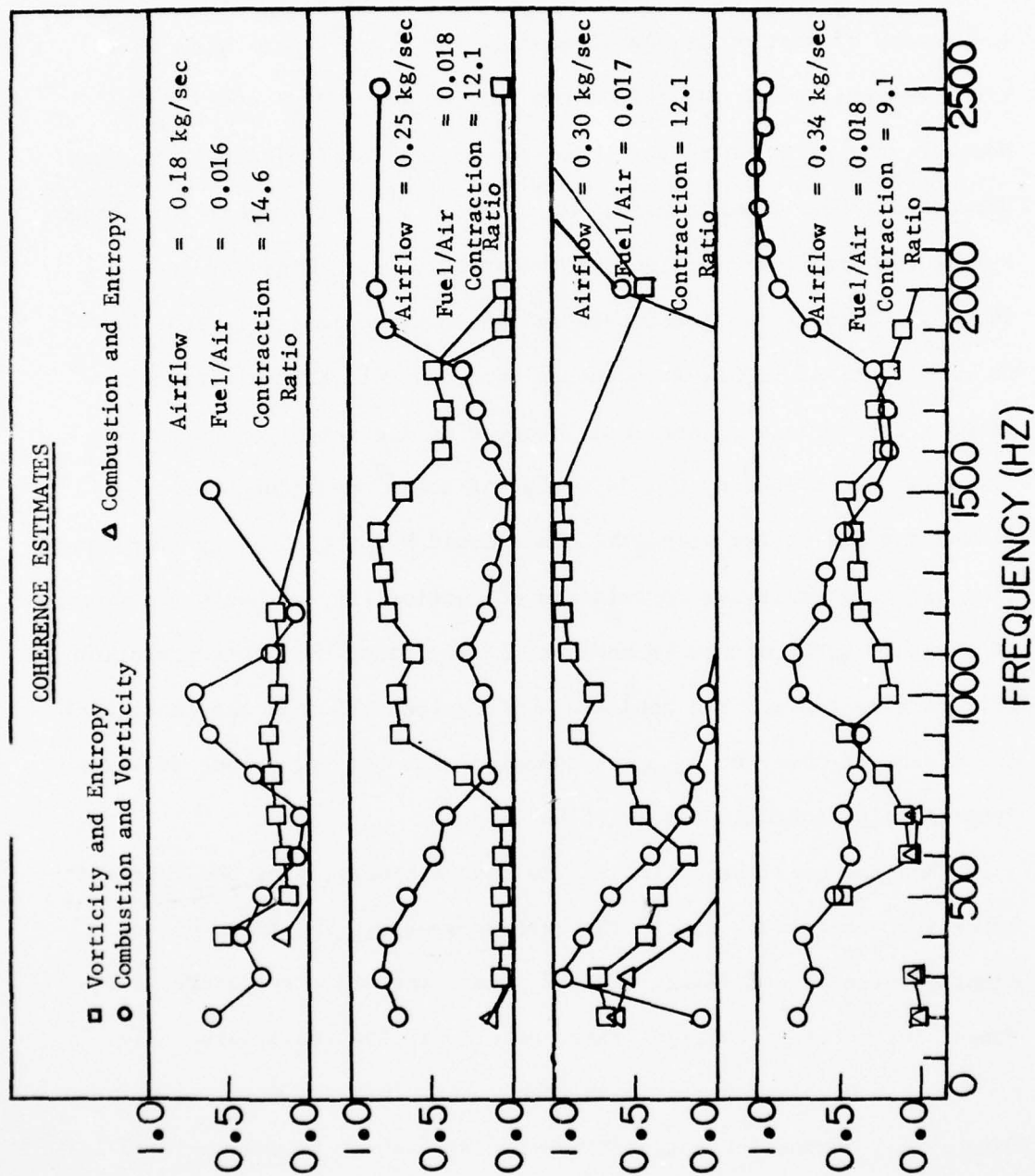
Figure 22. Ordinary coherence between sources for the four basic runs.

vorticity and entropy. These facts are merely stating that the off diagonal elements of Eq. (18) are important to the overall sound that is created, and one cannot justifiably split the sound into unique components.

As an example consider that only two sources are present, both of which are in phase with the radiated sound if each were to act alone. If they are correlated and out of phase with each other there would be no radiated sound, but if they were in phase there would be twice as much sound as compared with the sum of the sound from each individual source. Given, however, that there is a strong desire to say which cause is dominant in producing sound and that the coherence between sources is rarely perfect on Fig. 22, an approximate procedure will be used to split the sound.

The ordinary coherence between the sources and the measured sound was computed and multiplied by the measured sound, and these values are called the "sound due to source i", whatever source i is. The split is then displayed on Figs. 23-26. Ignore for the moment the bold square points on Figs. 23 and 24. If one adds up the components one will sometimes get greater than and sometimes less than the upper curve which is the multiple coherent noise. This is due to the problem above that the sources are coherent with each other. Nevertheless, approximately, two major facts are seen. These are a) at high frequency (say >1100 Hz) vorticity and combustion noise are dominant and, recall, usually highly correlated and b) the only frequency regime where entropy noise is strong is at low frequency (say < 600 Hz).
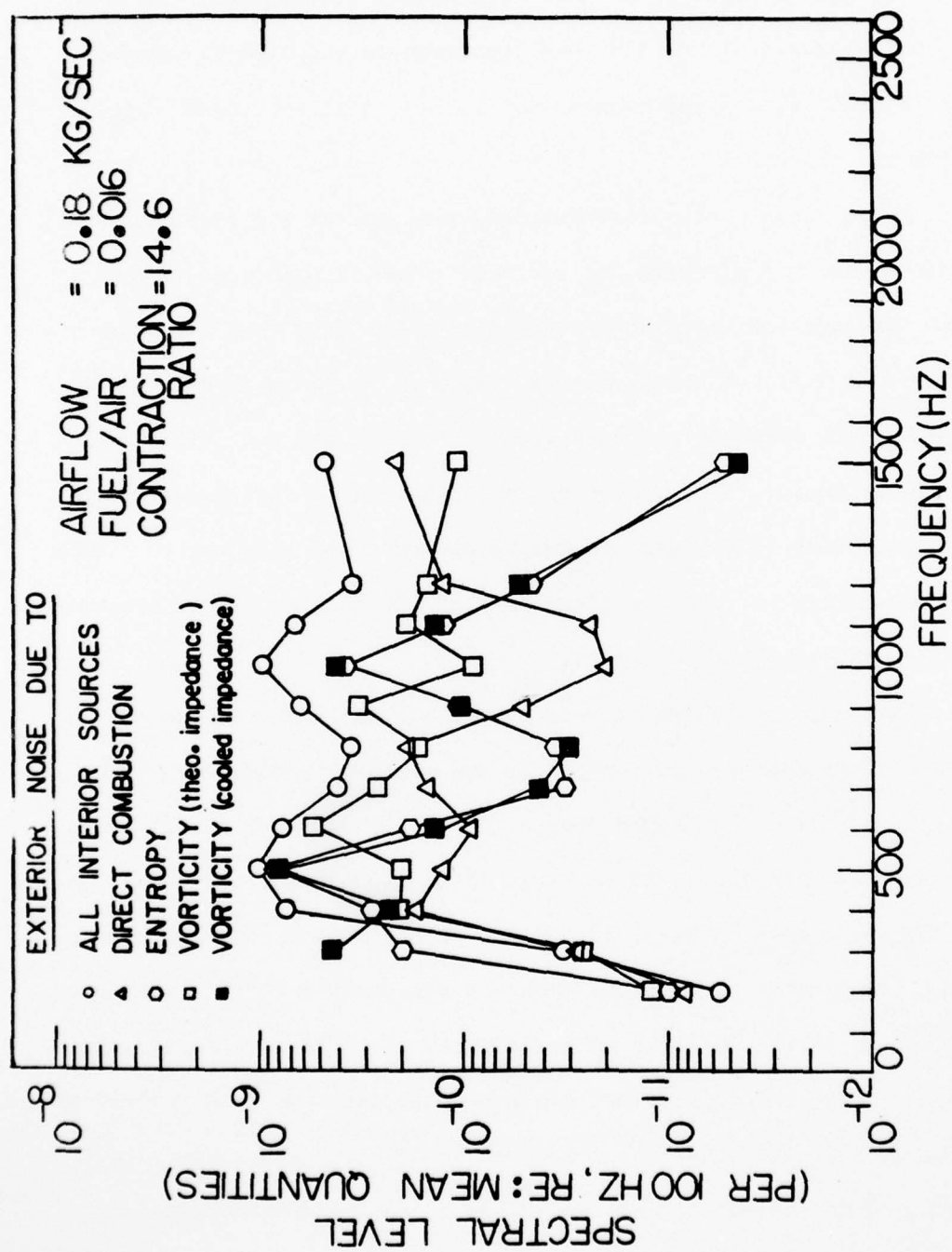
Figure 23. Multiple coherent noise and the split of the noise into the various causal elements for the 0.18 kg/sec run.
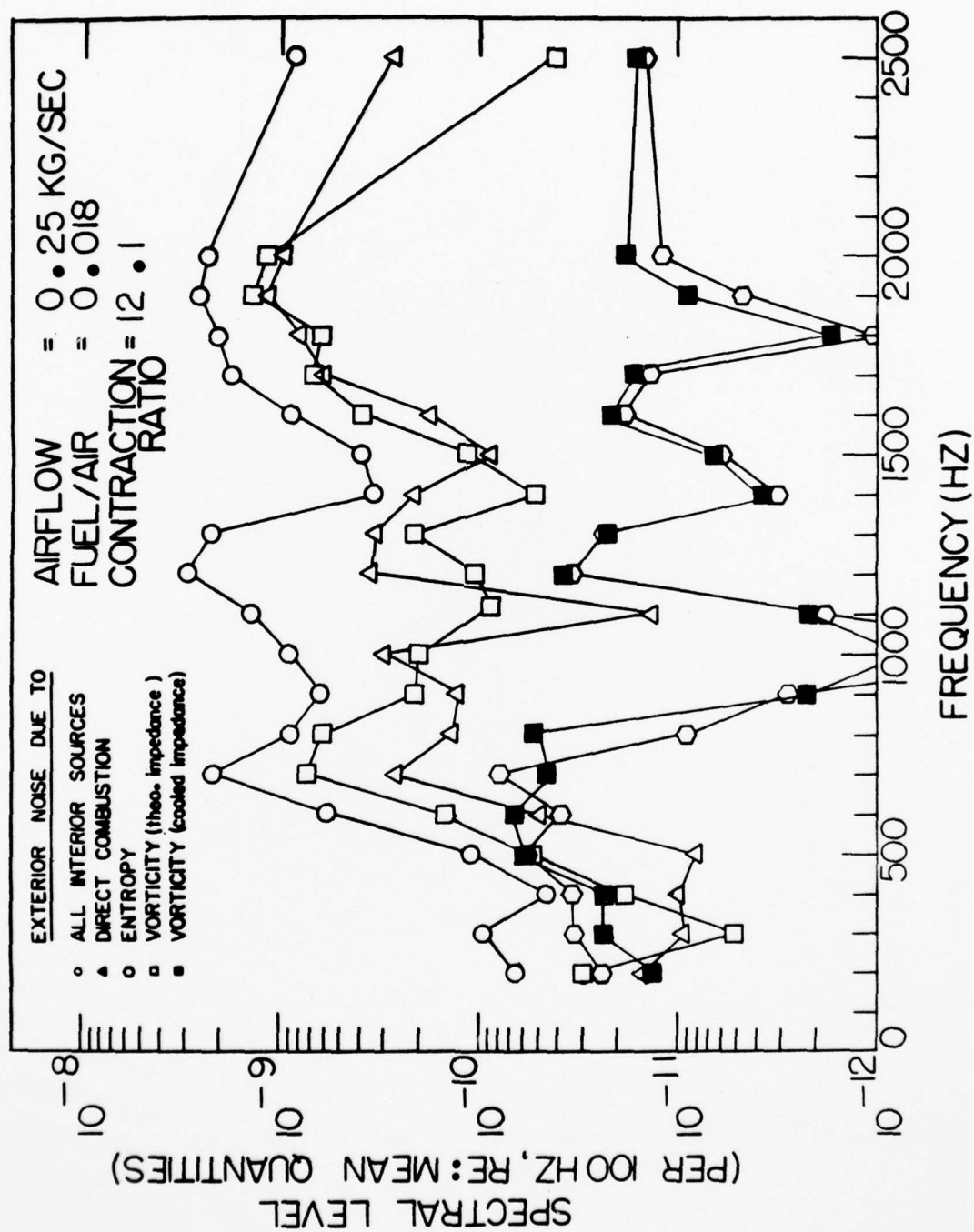
Figure 24. Multiple coherent noise and the split of the noise into the various causal elements for the 0.25 kg/sec run.
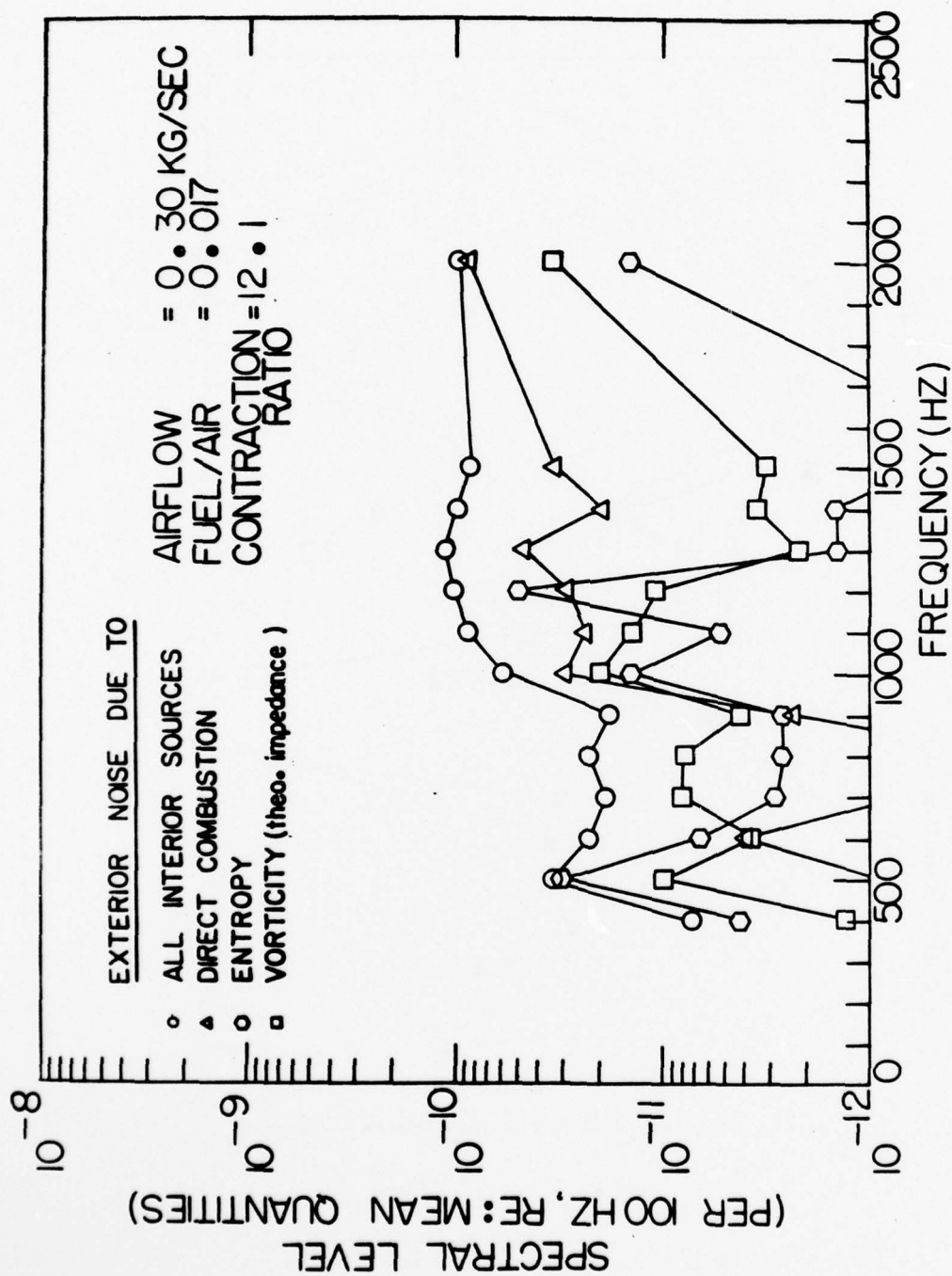
Figure 25. Multiple coherent noise and the split of the noise into the various causal elements for the 0.30 kg/sec run.
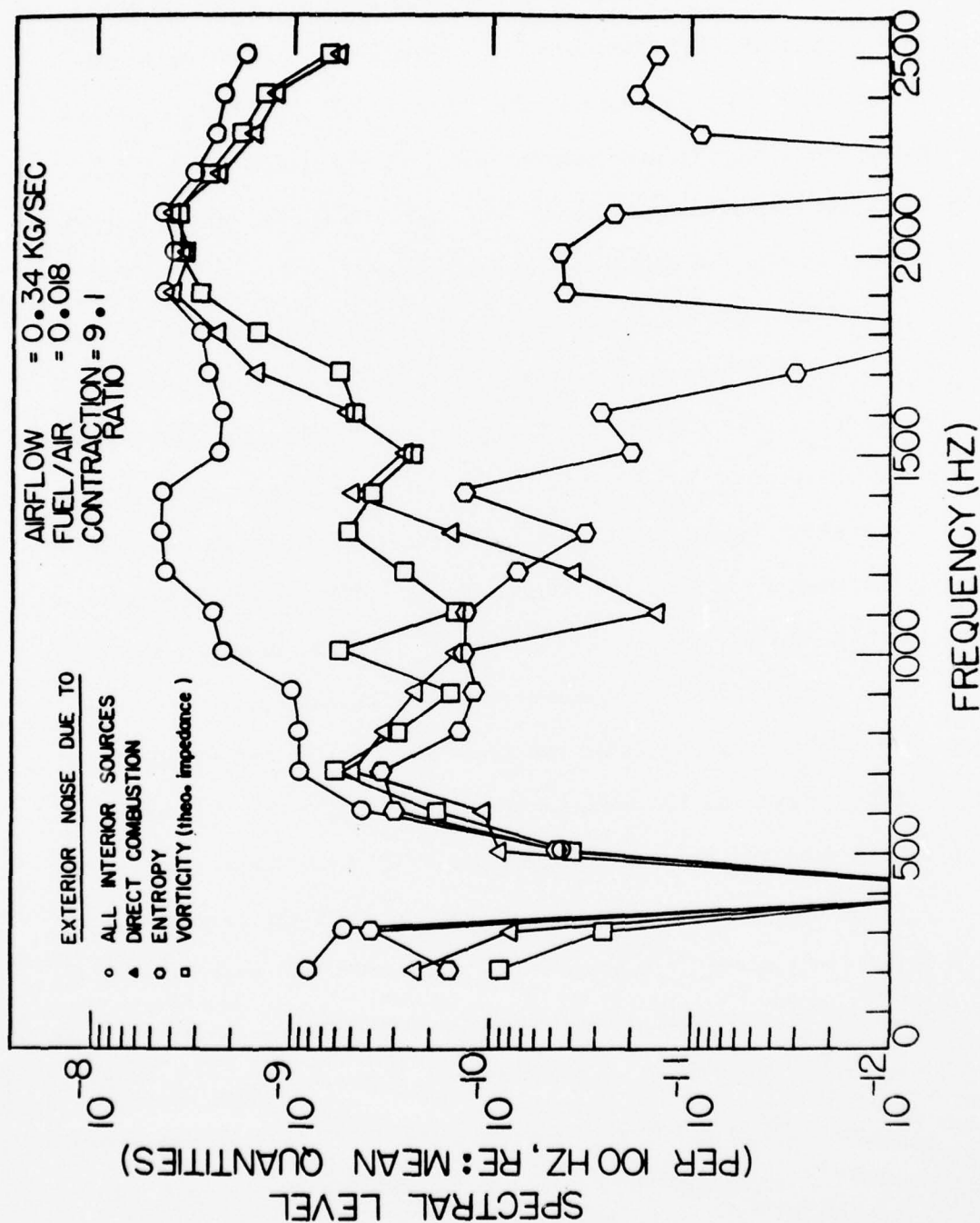
Figure 26. Multiple coherent noise and the split of the noise into the various causal elements for the 0.34 kg/sec run.

The comparisons become much less ragged if one does a band summation on the various components. If one adds the bands of the various components and divides by the summation of the bands of the overall multiple coherence runs, the figures 0.90, 0.65 and 0.91 result for the three diffuser runs in order of increasing mass flow. That is, the components add up to less than the whole, but comparable to it, because of the coherence between sources.

Shown in Table 4 are summations of the various components from 200-1500 Hz and 200-2500 Hz expressed as a fraction of the total of all components. The 1500 Hz point is selected because the first run only was analysed up to 1500 Hz. In the last two runs it is clear that combustion and vorticity noise dominate above 1500 Hz and, in fact, the second run had this domination at 1500 Hz. The first run had roughly equivalent source causality at 1500 Hz. Based on the last two runs, however, and the apparent takeover of combustion and vorticity at 1500 Hz on the first run (see Fig. 23), it can be surmised that if the first run had been analysed out to 2500 Hz, the same split would have occurred as with the last two runs. Such figures are entered in parentheses in Table 4 as an average from the last two runs. The major conclusions here are that a) combustion and vorticity noise dominate the noise output and are highly correlated and b) only at low frequency is entropy noise a strong source. What is being said here is that in this apparatus the presence of vorticity-nozzle interaction adds about a factor of two to the overall noise as compared to what would occur if only combustion noise were present. The relative split be-

tween the sources in the nozzle-only run was 63% , 23% and 14% and
the first two would undoubtedly have climbed relative to the last
one if the analysis had been carried to 2500 Hz.

Table 4

Split of the Noise into Causal
Properties for the Diffuser Runs

| Run | (Hz) Freq. | % Combustion | Vorticity | Entropy |
|---|---|---|---|---|
| 0.18 kg/sec | 1500 | 24 | 40 | 36 |
| | 2500 | (45) | (51) | (4) |
| 0.25 kg/sec | 1500 | 40 | 53 | 7 |
| | 2500 | 42 | 56 | 2 |
| 0.34 kg/sec | 1500 | 32 | 43 | 25 |
| | 2500 | 49 | 46 | 5 |

Returning for a moment to Figs. 23 and 24, the derived sound
due to vorticity is displayed by the bold squares when the impedances
measured by the cooled film probes are used. These are not believed,
however, for the reasons cited in Appendix B. Moreover, the indicated
$<v^2>$ rises by almost a factor of 100 which yields an unrealistic rms
fluctuation level (nearly 100%) for an area-averaged quantity.

## Sound Power Scaling

The multiple coherent sound power and the sound power scaling
laws are obtained by multiple corrections to the data. The power de-
sired is the effective sound power so that it may be compared with the
prediction formula of Section III.

Consider first the sound power for the four primary runs where the multiple coherent power is to be placed on an effective basis. Band summation was applied to the coherent mean square pressure of the $90^\circ$ microphone, but the spectra were corrected by a correction curve closely related to Fig. 1. It was assumed that combustion noise was dominant and the $|H_{Ao}|^2$ was compared with $|H_{Ao}|^2$ for a reflection free termination. The coherent $p_1$ was assumed proportional to $p_o$, as it would be if only combustion noise was present. The result is that 7.9 dB must be added to the measured mean square coherent $< p_1^2 >$ to bring it to an equivalent reflection free situation. This magnitude may have been expected from Fig. 1. It was then assumed that a monopole radiation pattern existed with $< p_1^2 >$ then converted to sound power. However, a further correction had to be applied to the data of the first run since it was analysed only out to 1500 Hz. It was noted in the second two diffuser runs that the ratio of the 2500 Hz value of $< p_1^2 >$ to the 1500 Hz value was a consistent 2.3. Consequently, this factor was multiplied to the sound power of the first run. The jet-only run was left unmodified, since at 2000 Hz, its upper analysis limit, the other runs had started to decay in the coherent $S_{11}$. In all cases, the resultant numbers were multiplied by 0.45, 0.42, 0.49 and 0.63, respectively, to convert the total sound to combustion noise sound, because the prediction formula is only good for pure combustion noise.

The results for the basic runs are shown in Table 5 and are quite interesting. The measured effective coherent sound power is about 10 dB

higher than the prediction formula for the runs with the diffuser, although the scaling with mass flow appears as predicted. On the other hand, the nozzle-only run with a high velocity exit jet shows a good comparison with the formula value. It is clear that the diffuser is doing something, but exactly what is not known. The first run value appears slightly high in comparison with the other two diffuser runs, but it should be remembered that the diffuser flow was separated. Consequently, there may have been some difference in sound transmission behavior or additional coherent sound generation.

Table 5

Sound Power from Experiment and from the
Correlation Formula for the Four Basic Runs

| Run | Acoustic Power (dB re $10^{-12}$w) | |
| --- | --- | --- |
| | Correlation Formula | Experiment |
| 0.18 kg/sec diffuser | 111.6 | 122.6 |
| 0.25 kg/sec diffuser | 116.4 | 125.0 |
| 0.34 kg/sec diffuser | 120.9 | 128.2 |
| 0.30 kg/sec nozzle only | 116.1 | 113.4 |

For the mid-contraction ratio case a set of runs were made with the diffuser while varying the airflow and fuel/air ratio off of the nominal operating condition. The $90^{o}$ B&K microphone was used as the reference microphone, monopole radiation was assumed and the "average" baseline multiple coherence value of 0.35 was applied directly to the overall $< p_1^2 >$. Moreover, the value from Table 4 of 42% combustion

noise was applied to the value and the 7.9 dB correction factor was
also applied. The results are shown in Table 6. Notice the close
agreement between the band summation value in Table 5 and the base-
line power obtained by manipulation of the overall measured pressure
in Table 6. The fuel/air ratio scaling was as expected. However, the
observed dependence on mass flow is stronger than predicted. This
may be giving a clue that the diffuser is indeed at fault in causing
higher overall levels than expected. As mass flow increases from the
baseline value a shock must form in the diffuser which may be sensi-
tive to upstream disturbances in causing more noise. On the other
hand, as the mass flow drops from the choking condition the experi-
mental sound power is dropping rapidly toward the formula value.
However, if this were to be a valid explanation then the same ex-
treme sensitivity would have had to have been present when fuel/air
ratio was varied, and it was not.

Table 6

Sound Power from Experiment and the
Correlation Formula for the Variations
about the Baseline Case for Nozzle-Diffuser
Assembly # 2

| Airflow (kg/sec) | Fuel/Air | Power (dB re $10^{-12}$ w) | |
| --- | --- | --- | --- |
| | | Correlation | Measured |
| 0.25 | 0.0180 | 116.4 | 125.3 |
| 0.21 | 0.0175 | 114.2 | 119.7 |
| 0.31 | 0.0173 | 118.3 | 129.8 |
| 0.25 | 0.0156 | 115.9 | 125.2 |
| 0.25 | 0.0203 | 117.1 | 126.2 |

## Discussion

Upon review of the data the following summary is offered:

a) The source quantities behaved similarly in all runs, except
for an empirical discovery that the level is mass flow sen-
sitive which only serves to strengthen the agreement be-
tween the interior theory and experiment.

b) The impedance of a choked nozzle tends to favor higher fre-
quencies in the radiated sound than heretofore observed。

c) There is high correlation between the vorticity and combus-
tion noise sources and they are dominant in producing co-
herent noise, especially at the higher frequencies。

d) The multiple coherence for the nozzle-diffuser assemblies
was high at high frequencies where the majority  of sound
radiation occurred.

e) The coherent noise from the nozzle-only configuration was
somewhat lower than predicted but the coherent noise from
the nozzle-diffuser assemblies was much higher than pre-
dicted.

f) The split between vorticity and combustion noise favored
vorticity noise more in the case of the nozzle-diffuser
apparatus as compared with the nozzle-only case.

For the nozzle only case a low value compared with the prediction
formula can be relatively easily explained. First of all, the analysis
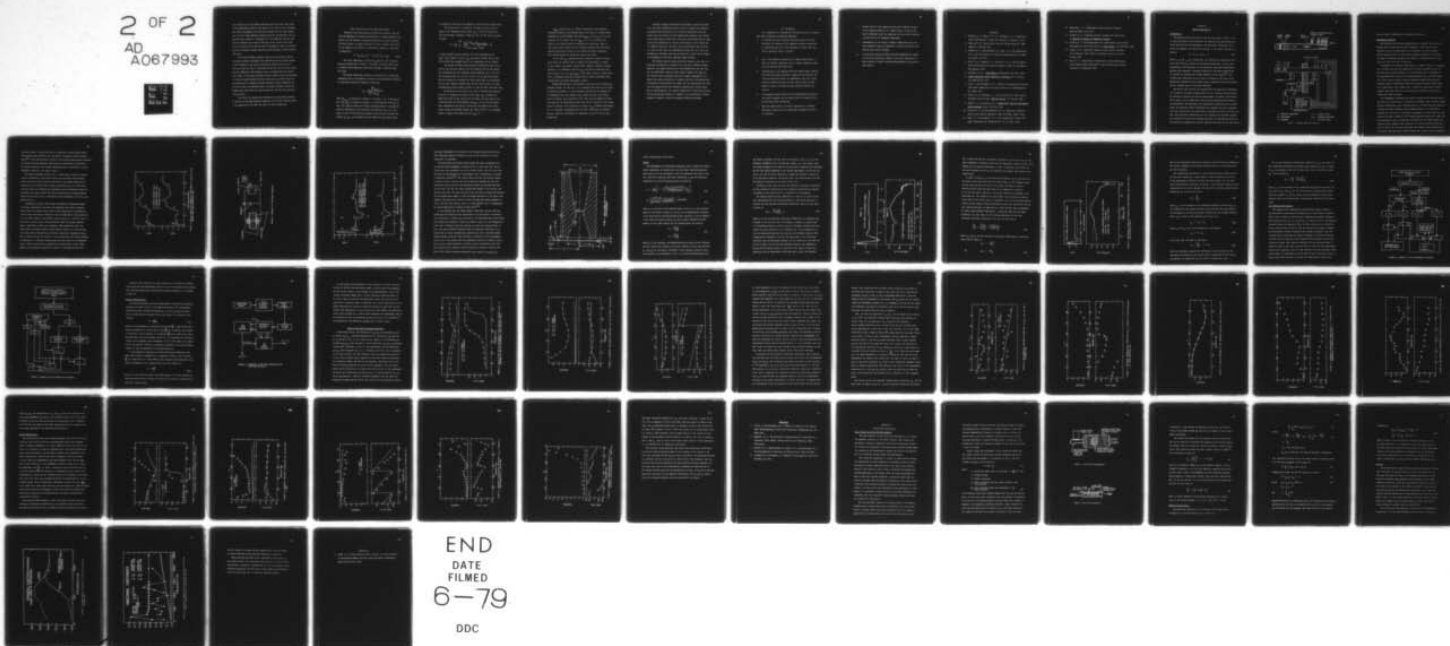
was carried out to only 2000 Hz and there would have been some sound in the 2000-2500 Hz band to have added to the overall level. Secondly, near field microphones were used and the high velocity, high temperature jet has a high impedance mismatch with the surroundings. The jet may have been acting as a waveguide for a few diameters and the near field microphones saw a smaller fraction of the overall noise than would have been seen in the far field. Consequently, there is believed no real discrepancy between expectation and experiment for the nozzle-only case.

The nozzle-diffuser assembly cases are more puzzling, and the conclusion appears inescapable that additonal noise was being created in the diffuser by the vorticity which was coherent with the can-interior vorticity. This is indicated by the fact that vorticity noise was more dominant in the diffuser cases as compared with the nozzle case. Thus, a flow with an adverse pressure gradient may be susceptable to vorticity-flow interaction which causes noise. A second reason for increased noise is perhaps the high coherence between combustion and vorticity noise. As described above, two highly coherent sources can produce more noise than the noise produced by the sum of two uncorrelated sources.

The lack of an entropy noise dominance was surprising. However, it was due to the high frequency dominance of the noise. Entropy noise is as important as the other two types at lower frequencies.

## VIII. Corrections to the Prediction Formula

Because of the uncertainties in some of the results, the fact that the dominance of relative contributions is highly frequency sensitive, and the combustor termination appears to strongly influence the noise output, it appears difficult to give a general correction to the combustor rig formula for sound power. However, a form which is suggested is

$$P = P_{eq} \, \eta_{ter} \, \eta_A ( 1 + \eta_v + \eta_s) \, \eta_{int} \, \eta_{down} \tag{26}$$

The first computation is that of $P_{eq}$ from Eq. (21) using the empirical coefficients of Table 1. This gives the power which would be radiated from combustion noise alone through a reflection free end plane.

The second computation involves a correction for a reflecting termination and is an impedance correction. Using estimated, measured or calculated isentropic impedance coefficients

$$\eta_{ter} = \frac{1}{\Delta\omega} \int_0^{\Delta\omega} \frac{|H_{Ao}|^2}{|H_{Ao_{ref}}|^2} \, d\omega$$

where $H_{Ao_{ref}}$ is obtained by setting $x = \ell$ and $a_\omega = -\frac{1}{\gamma}$ in the $H_{Ap}$ of Eq. (12). $H_{AO}$ is obtaind by setting $x = \ell$ and using the actual $a_\omega$ in Eqs. (12). This is merely an average correction factor to account for spectral differences in the acoustics of different rigs. It is the source of the 7.9 dB correction applied in the previous section. The product $P_{eq} \, \eta_{ter}$ is the amount of pure combustion noise which would

be radiated in the rig in the absence of vorticity and entropy noise.

The third term is a correction, if known, for the spectral shape of the combustion noise source, $A_\omega$. It could be measured by the two microphone technique using Eq. (15). If the actual $A_\omega$ shape is known

$$\eta_A = \frac{1}{\Delta\omega} \int_0^{\Delta\omega} \frac{|A_\omega|^2}{|A_\omega|^2_{\text{this report}}} \frac{|A_{\omega_{\text{ref}}}|^2_{\text{this report}}}{|A_{\omega_{\text{ref}}}|^2} \, d\omega$$

It would actually be more accurate to do the averaging on the $|H_{A0}|^2 |A_\omega|^2$ product to get a $\eta_{\text{ter}} \eta_A$ product average. The $\eta_A$ term has actually been assumed unity in all comparisons of this report.

The fourth and fifth terms account for additional noise due to entropy and vorticity effects. For the diffuser runs of this report and considering the full frequency range 0-2500 Hz $\eta_V = 1.1$, $\eta_S = 0.1$. For the nozzle only run, $\eta_V = 0.3$, $\eta_S = 0.2$. In any given case these would be difficult to estimate but would really have to be measured. One can tell, however, whether they are zero because there are some configurations such as those of Refs. (1) and (4) where they were zero.

As one moves to the right in Eq. (26) it becomes more and more difficult to estimate the values of the terms. $\eta_{\text{int}}$ accounts for additional noise if the sources are correlated. In this report it is conjectured that for the diffuser runs $\eta_{\text{int}} \approx 2$, but for any given case, depending on the type of correlation, any number for a three source system could emerge between the limits 0 and 4. It is perhaps safest to neglect this effect and set $\eta_{\text{int}} \approx 1$.

$\eta_{down}$ accounts for all effects downstream of the combustor termination plane or the choking plane in the case of a choked nozzle termination. In the diffuser runs here $\eta_{down} \approx 3$ if $\eta_{int} \approx 2$, as conjectured. In the nozzle only run $\eta_{down} \approx 1$. It is here where the effects of an engine installed configuration would enter. That is, this factor would account for the acoustical behavior and additional coherent generation of noise in the turbine and nozzle assemblies. Such considerations are beyond the scope of this work.

In Eq. (26) $P_{eq}$ contains the basic combustor variables scaling laws. Since all sources scale in roughly the same manner, as shown in this report, $P_{eq}$ should contain proper combustor variables scaling behavior. It is essential that the $\eta_{ter}$ correction be made, and after that, if $\eta_{A}(1 + \eta_{v} + \eta_{s})\,\eta_{int}\,\eta_{down}$ is set equal to unity, a lower limit for P is probably the result, unless there is heavy attenuation downstream before the power measurement is made.

Moving specifically to the possible corrections to the prediction formulas of Refs. (1) and (4), it is recognized that there are two types of prediction schemes - one for combustor rigs and one for engines. It is recommended that for combustor rigs, where vorticity and entropy noise are absent, the correlation of Eq. (21) with the numbers of Table 1 be used for the sound power output. This can be corrected to the actual acoustic behavior of the combustor by using an $\eta_{ter}$ estimated from Figure 1. It is therefore recommended that the Pratt and Whitney and General Electric combustor rig formulas be abandoned in favor of the one generated here.

Turning to engine correlations the problem is much more diffi-
cult. The Pratt and Whitney method consists of taking the combustor
rig formula and correcting it by a turbine transmission loss and
nozzle loss. The results of this program show, however, that further
corrections should be made for a) vorticity and entropy noise b) addi-
tional noise generation by vorticity and entropy in the turbine and
c) combustor acoustics. The first two are noise gains and the third
is a loss so that they are compensating corrections. As a first ap-
proximation, therefore, they may be expected to cancel and no change
is recommended to the Pratt & Whitney engine formula.

The General Electric engine prediction scheme is not tied to a
theoretical mechanism as strongly as is the Pratt & Whitney scheme.
Moreover, the engine correlation of each manufacturer does not hold
for the sound power results of each other's engines. No light has
been shed on this discrepancy from this program. Consequently, for
engine core noise correlations it appears that both correlations must
be accepted as valid within the bounds that the correlations are only
used for engines within the individual manufacturer's group. While
this is unsatisfactory, the current program has at least been success-
ful for giving some guidance in combustor rig correlations. A future
program is needed to clarify the engine correlation problem.

# IX. Conclusions

It is imperative in scanning the conclusions below to recognize that some of them may be apparatus dependent.

1. A correlation, with a rational theoretical basis, has been developed for combustors with impedance matching termiations or exhausting directly to the atmosphere. In such cases only direct combustion noise is present.

2. Due to the impedance properties of a choked nozzle there is a shift in radiated combustion noise to higher frequencies than would be expected from prior data.

3. Contributions to the radiated noise for choked nozzle termination have been shown from direct combustion and indirect vorticity and entropy sources. An unambiguous split into causal relations between the noise and the sources cannot be made, however, because of relatively high coherence between the sources.

4. A discrepancy between theoretical and experimental scaling of the source strengths was seen which serves to explain the observed sound power scaling law.

5. When the choked nozzle is further terminated by a diffuser additional coherent noise is generated, although the source is uncertain.

6. Entropy noise is only important below about 1000 Hz, because of the impedance behavior of a choked nozzle. Vorticity and direct combustion noise are important over the entire frequency spectrum and are of comparable magnitudes.

7. Measurements of two acoustic pressures downstream of the primary combustion zone are sufficient to isolate the direct combustion noise source strength.

8. A correlation formula procedure has been suggested for combustor rig noise prediction. However, for strict application it would require at least as detailed measurements as outlined in this report.

## References

1. Mathews, D. C., Rekos, N. F. Jr., and Nagel, R. T., "Combustion Noise Investigation," Report No. FAA RD-77-3, February, 1977.

2. Cumpsty, N. A., "Excess Noise from Gas Turbine Exhausts," ASME Paper No. 75-GT-61, 1975.

3. Strahle, W. C., Muthukrishnan, M., Neale, D. H. and Ramachandra, M. K., "An Investigation of Combustion and Entropy Noise," NASA CR 135220, July 1977.

4. Matta, R. K., Sandusky, G. T. and Doyle, V. L., "GE Core Engine Noise Investigation-Low Emission Engines," Report No. FAA-RD-77-WA, February, 1977.

5. Goldstein, M. E., Aeroacoustics, McGraw-Hill, New York, 1976.

6. Liquid Propellant Rocket Combustion Instability (D. T. Harrje, ed.) NASA SP-194, 1972.

7. Crocco, L and Sirignano, W. A., "Behavior of Supercritical Nozzles under Three Dimensional Oscillatory Conditions," AGARDograph No. 117, NATO, 1967.

8. Levine, H. and Schwinger, J., "On the Radiation of Sound from an Unflanged Circular Pipe," Physical Review, 37, 383-406, 1948.

9. Bendat, J. S. and Piersol, A.G., Random Data: Analysis and Measurement Procedures, Wiley, New York, 1971.

10. Strahle, W. C. and Shivashankara, B. N., "Combustion Generated Noise in Gas Turbine Combustors," NASA CR 134843, August, 1974.

11. Matta, R. K. and Mingler, P. R., "Core Engine Noise Control Program," FAA Report No. FAA-RD-74-125, Vol. II, July, 1976.

12. Emmerling, J. J., "Experimental Clean Combustor Program," NASA CR 134853, July 1975.

13. Strahle, W. C., "Combustion Noise," accepted for publication in _Progress in Energy and Combustion Science_.

14. Strahle, W. C. and Muthukrishnan, M., "Thermocouple Time Constant Measurement by Cross Power Spectra," _AIAA Journal_, 14, 1642-1644, 1976.

15. Candel, S. M., "Analytical Studies of Some Acoustic Problems of Jet Engines," Ph.D. Thesis, California Institute of Technology, 1972.

16. Bell, W. A., "Experimental Determination of Three-Dimensional Liquid Rocket Nozzle Admittances," Ph.D. Disserattion, Georgia Institute of Technology, 1972.

Appendix A

## Entropy Tube Results

### Introduction

The purpose of using the entropy tube facility, shown in Fig. 1, was to check the values of the admittance and transmittance coefficients, obtained from the hot flow experiments. The admittance coefficients for a nozzle are defined by an admittance relation, at the nozzle entrance, as given by

$$V_s + a_s \, p_s + b_s \, \sigma_s = 0 \tag{A1}$$

where $V_s$, $p_s$ and $\sigma_s$ are, respectively, the appropriate transforms of the plane wave velocity, pressure and entropy perturbations. $a_s$ and $b_s$ are, respectively, the isentropic and non-isentropic admittance coefficients. Equation (A1) expresses a boundary condition at the nozzle entrance and is obtained by studying the unsteady behaviour of the nozzle[A1]. The transmittance coefficient for any nozzle is defined as the ratio of the appropriate transform of the pressure pulse, transmitted out of the nozzle, and the incident pulse at the nozzle entrance.

The entropy tube facility was designed with the objective of obtaining a) a transient isentropic pressure pulse and b) a transient entropy pulse. By appropriate internal and external measurements of pressure fluctuations, and by using a set of simplified linear acoustic equations which simulate the experiments, the admittance and transmittance coefficients for a given nozzle are evaluated. These coefficients are compared with the corresponding values from the hot flow experiments, described in section 6 of this report. The admittance coefficients are also compared with available approximate theoretical values. This Appendix describes the experimental facility, the theoretical formulation, the data reduction and analysis, and the final re-
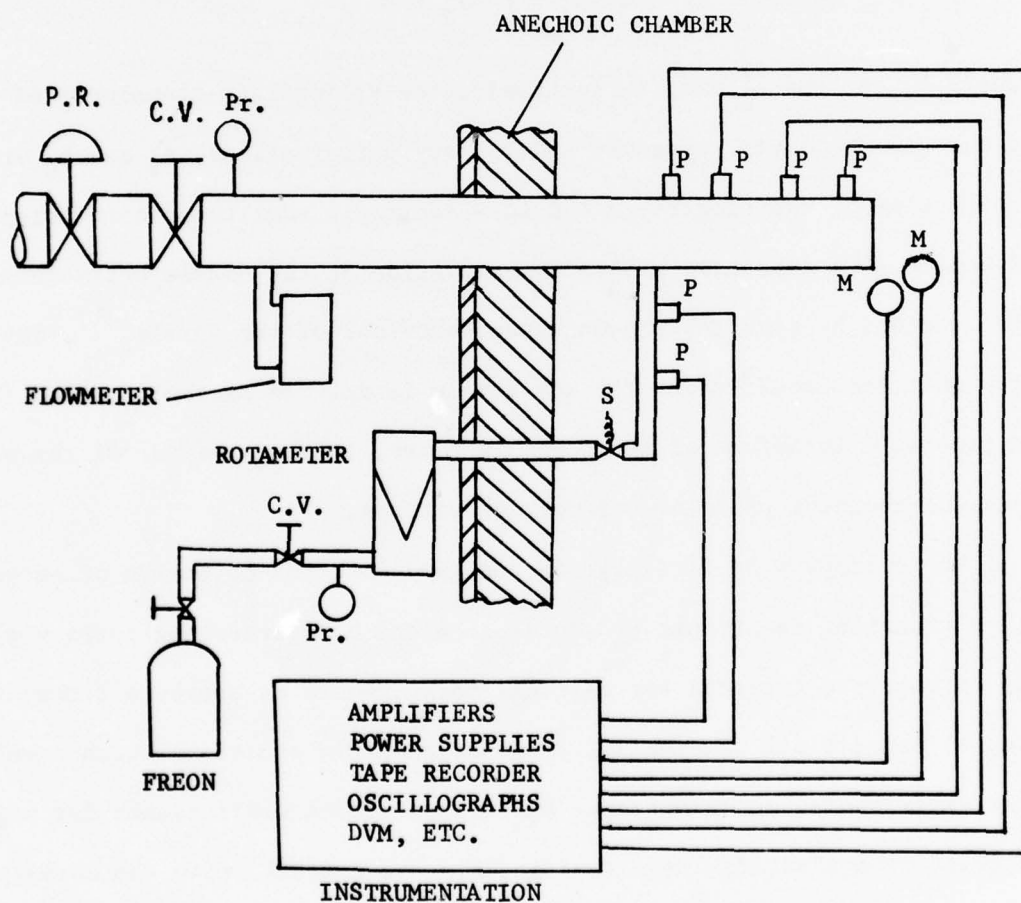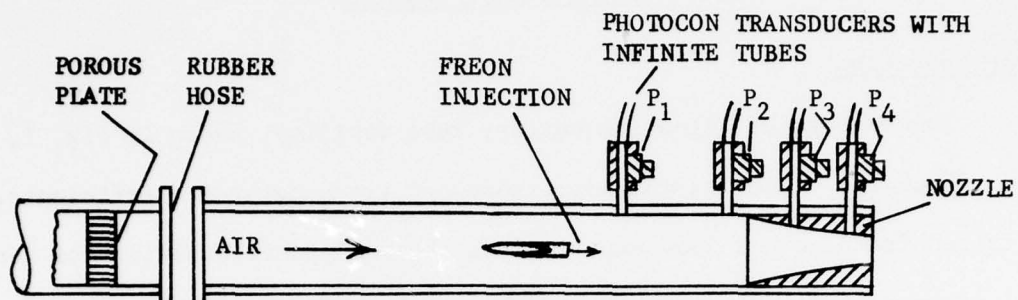
Fig. 1 . Entropy Tube Test Facility

sults in terms of admittance and transmittance values.

## Experimental Facility

The objective was to obtain, experimentally, transient isentropic and entropy pulses and record the nozzle response to these pulses. With a transient pulse, one experimental run is expected to yield, through a Fourier decomposition, all the desired frequency information. Of course, the highest acceptable frequency will depend, as explained later in this section, on the rise time of the pulse.

A schematic of the entropy tube facility is shown in Fig. 1. It consists of a constant area two inch diameter duct, having a uniform flow of air. Any test nozzle, whose response is to be evaluated, can be connected to the downstream end of this duct. Airflow, obtained from a 150 psia reservoir, first passes through a pressure regulator, which filters out the upstream pressure disturbances. Then the flow goes through a porous plate and a rubber hose, both of which help to reduce the flow noise. A static pressure measuring device and a flow meter are provided to monitor the steady state flow variables.

Two independent techniques were used for generating the desired pulses. The first one, shown in Fig. 1, consisted of sending a shot of freon, a high molecular weight gas, into a uniform airflow. A solenoid valve was used for creating the sharp transient pulses. When switched on, its operation is analogous to the action of puncturing a diaphragm in a shock tube test. The process initiates a series of left running expansion pulses and a right running compression pulse, followed by the freon flow. The right running compression pulse, termed as the isentropic (or initial) pressure pulse, was used to obtain the isentropic admittance and transmittance coefficients of the nozzle. The freon front travels through the injector, into the constant

area duct, where it mixes with the air to generate a sharp entropy pulse. This entropy pulse interacts with the nozzle to generate a sharp pressure pulse[A2]. This pressure pulse, termed as the entropy pressure pulse, was used to evaluate the non-isentropic admittance and transmittance coefficients. The typical isentropic and entropy pressure pulses, as monitored by two microphones in the duct, are shown in Fig. 2.

The second technique, shown in Fig. 3, consisted of creating an abrupt spark by discharging a high charge across two electrodes. The transient spark creates an initial pressure pulse (due to the energy added) and an entropy pulse (or the hot spot). These pulses were used, as in the freon injection case, for estimating the isentropic and non-isentropic acoustical properties of a given nozzle. The typical isentropic and entropy pressure pulses for the spark case, as monitored by two microphones in the duct, are shown in Fig. 4.

A comparison of Figs. 2 and 4 shows the essential difference between the pulses, generated by the above two techniques. The initial pressure pulses look very similar except that the pulse generated by the spark has a much higher amplitude as compared to the one generated by freon injection. Also the spark creates a much sharper initial pulse, i.e. the rise time of the pulse, is much smaller. Some explanation about the entropy pressure pulses, generated by these two techniques, seems appropriate here. The freon injection process creates a high molecular weight or a positive density pulse, which, encountering the nozzle, generates a compression pulse. This is shown as pulse (2) in Fig. 2. On the other hand, the spark discharge is equivalent to a negative density pulse and thus results in an expansion pulse. (These conclusions are theoretically substantiated in Ref. (A2)). However, the theoretical formulation, given in a following section, has
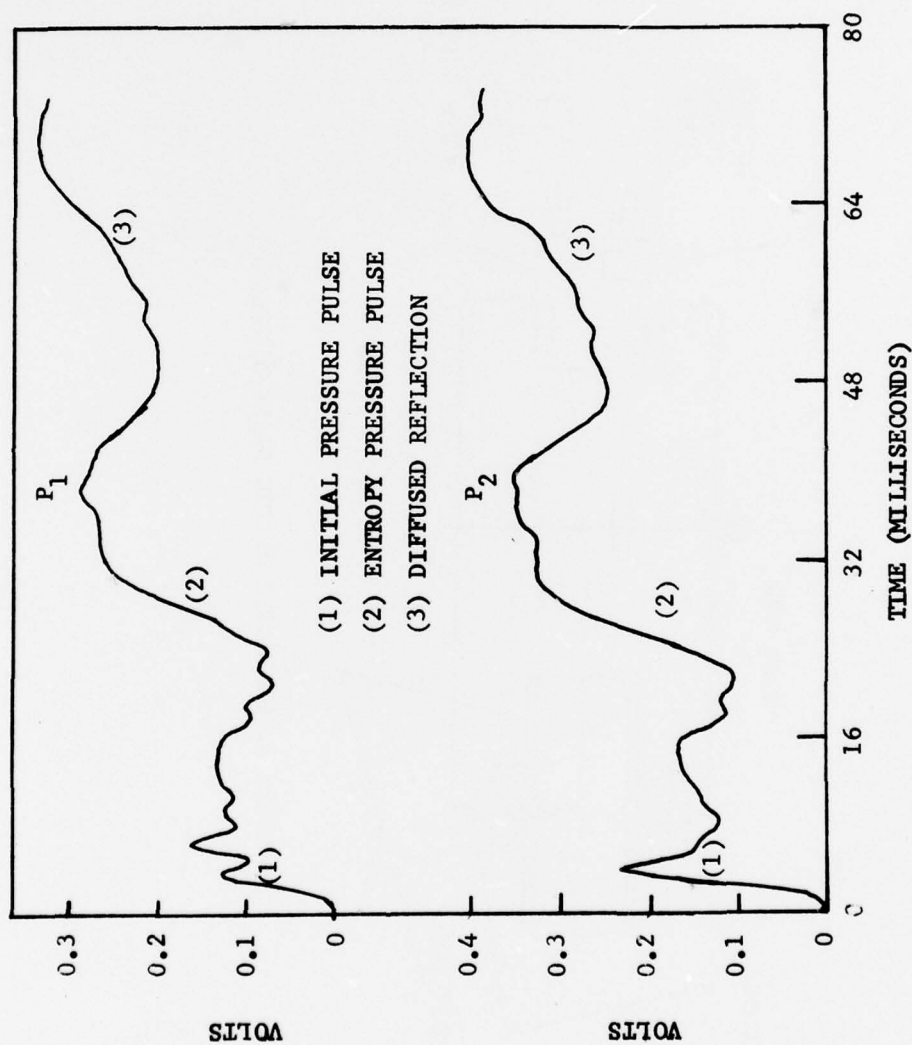
97



FIGURE 2. TYPICAL SIGNALS AS RECORDED BY MICROPHONES $P_1$ AND $P_2$ IN THE ENTROPY TUBE. FREON INJECTION CASE.
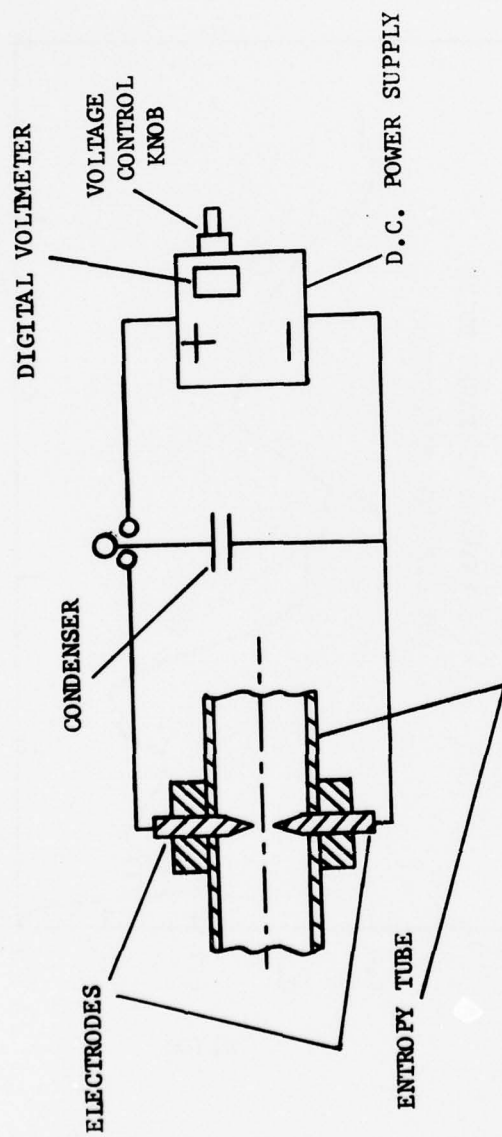
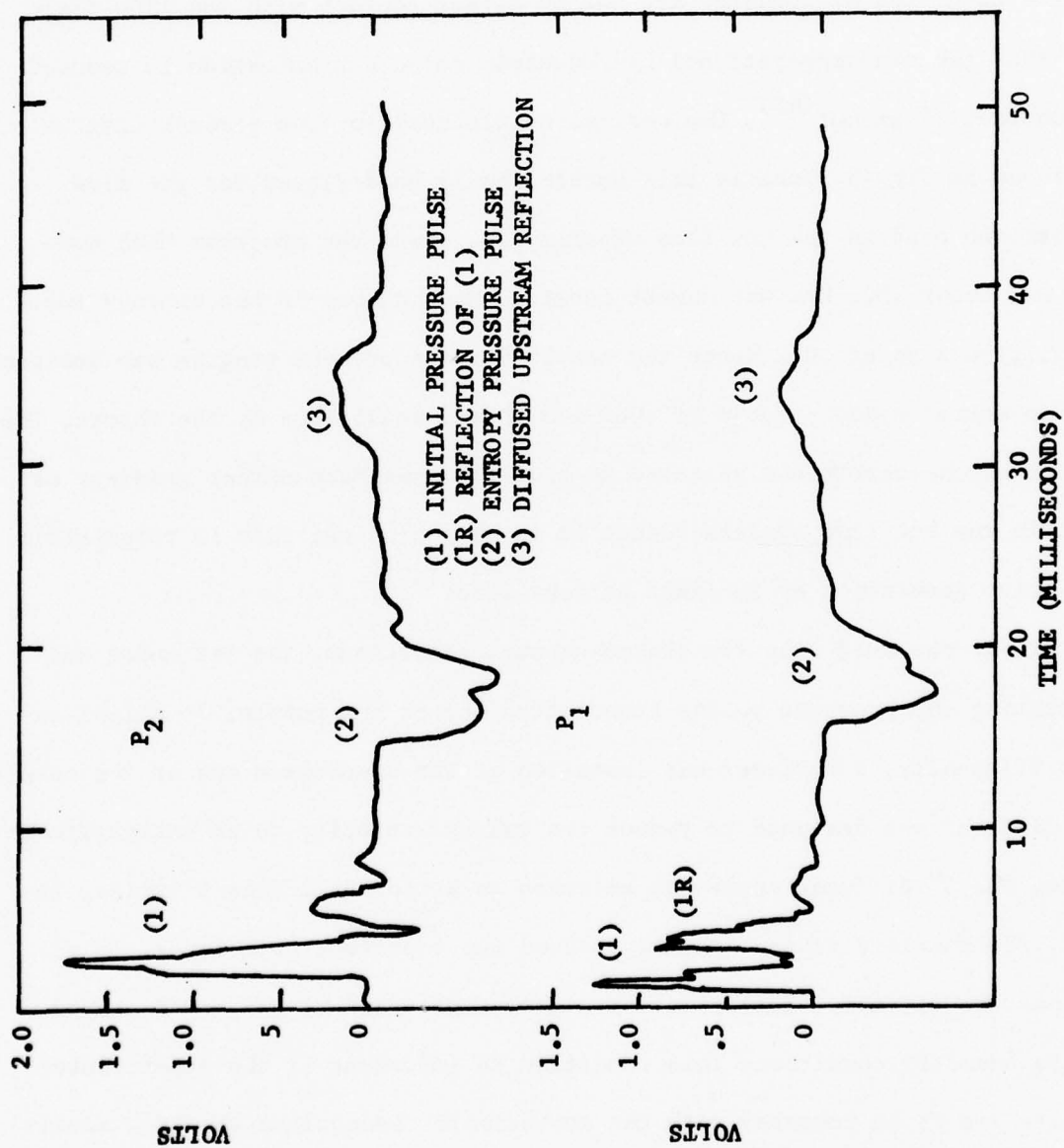FIGURE 3. SCHEMATIC OF THE SPARK DISCHARGE.

FIGURE 4. TYPICAL SIGNALS AS RECORDED BY MICROPHONES $P_2$ AND $P_2$ IN THE ENTROPY TUBE. SPARK CASE.

been made independent of the nature of the entropy pressure pulse. Thus, both techniques should be identical as far as the evaluation of nozzle properties is concerned.

For monitoring the pressure pulses inside the tube, microphones with an infinite tube arrangement, as shown in Fig. 1, were used. With the infinite tube, the microphones are not in direct contact with the flow field and thus the non-propagational hydrodynamic noise contamination is reduced a substantial amount[A3]. The conical nozzle used for the present program is shown in Fig. 5. Ideally this nozzle should be designed for the flow conditions used in the how flow experiments, where the upstream Mach number was about .02. But the lowest possible Mach number in the entropy tube facility was about .06. Hence the nozzle for the present program was designed for an entrance Mach number of .065 and choked conditions at the throat. The length of the nozzle was selected to give the same Mach number gradient as used in the hot flow studies, since it is this gradient that is responsible for noise generation by incident entropy waves[A1].

It was observed that for choked exhaust conditions, the jet noise was blanketing the pressure pulses transmitted out of the nozzle. To alleviate this difficulty, a diffuser was installed at the downstream end of the nozzle. The diffuser was designed to reduce the exhaust velocity to an insignificant value. The $5^\circ$ diffuser angle was selected to avoid stall possibilities. In fact, the nozzle diffuser assembly served two important objectives. It a) reduced the jet noise contamination significantly and b) preserved choked nozzle boundary condition: This condition is important if the experimental results are to be compared with the approximate theoretical results, available only for choked conditions. Internal pressure measurements were used for evaluating the isentropic and non-isentropic admittance values of the nozzle. The external pressure measurements were used for obtaining the
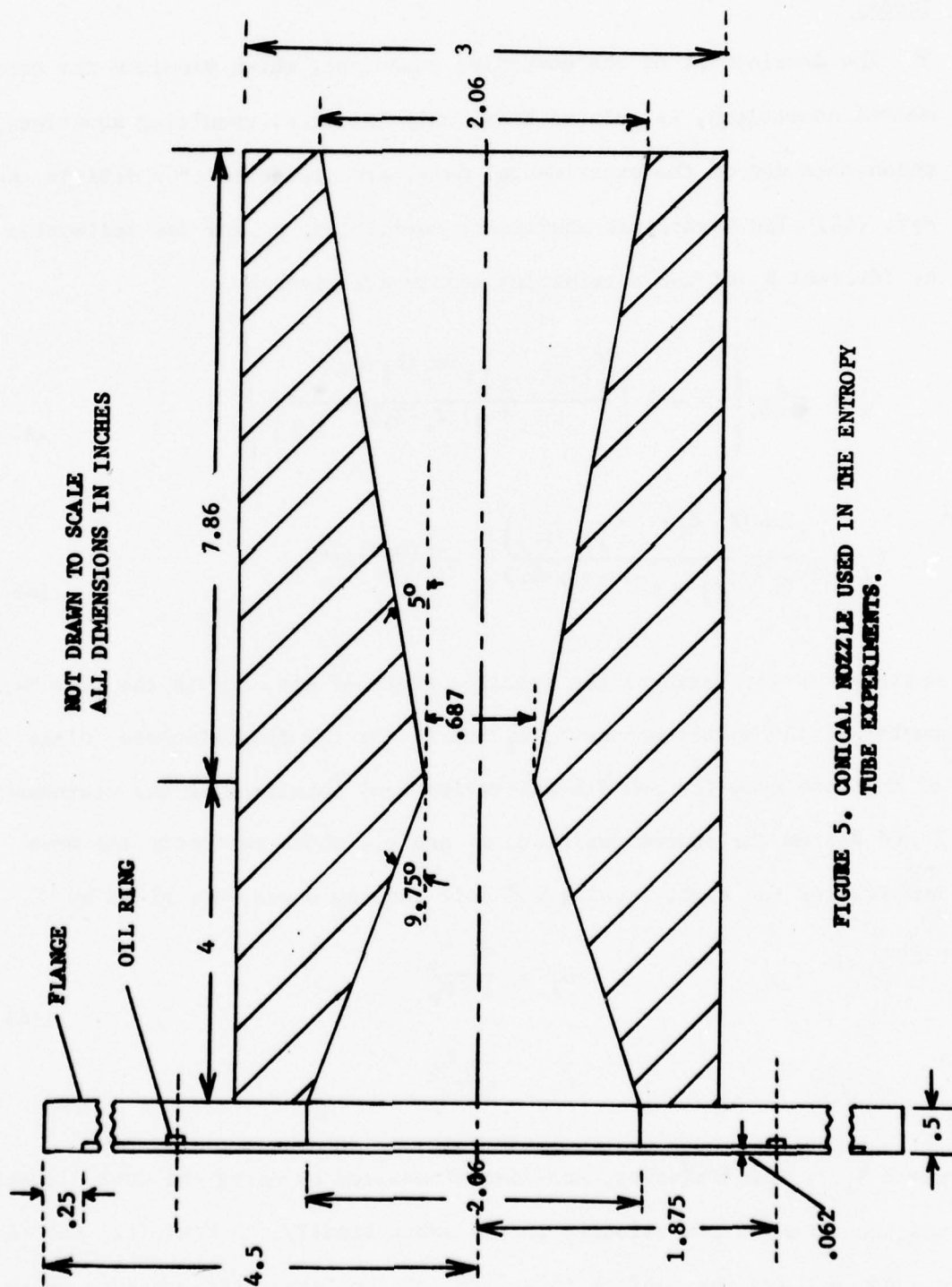
NOT DRAWN TO SCALE
ALL DIMENSIONS IN INCHES

FLANGE

OIL RING

FIGURE 5. CONICAL NOZZLE USED IN THE ENTROPY
TUBE EXPERIMENTS.

nozzle transmittance coefficients.

## Theory

The development of the governing equations, which simulate the experimental conditions, is deleted here. Only the final resulting equations, which make use of the experimental data, are presented (For details, see Ref. (A2)). The isentropic admittance coefficient $a_s$ and the reflection coefficient $R_s$ of the terminating nozzle are given by

$$a_s = \frac{1}{\gamma a M_o} \left[ 1 - 2 \left\{ \frac{\left( p_{s_1}/p_{s_2} \right) e^{im_2(Z_2-Z_1)} - 1}{e^{i(m_1+m_2)(Z_2-Z_1)} - 1} \right\} \right] \qquad (A2)$$

$$R_s = \left\{ \frac{e^{im_1(Z_2-Z_1)} - \left( p_{s_1}/p_{s_2} \right)}{\left( p_{s_1}/p_{s_2} \right) - e^{-im_2(Z_2-Z_1)}} \right\} e^{-i(m_1+m_2)Z_2} \qquad (A3)$$

where $\gamma_a$ is the ratio of the specific heats of air, $M_o$ is the flow Mach number at the nozzle entrance, $Z_1$ and $Z_2$ are the dimensionless (diameter of the tube used for non-dimensionalization) locations of the microphones 1 and 2 from the source position. $m_1$ and $m_2$, which represent the wave numbers for the right running and left running waves, are given by

$$m_1 = \frac{\beta_1 M_o}{1 + M_o}$$

$$\qquad (A4)$$

$$m_2 = \frac{\beta_1 M_o}{1 - M_o}$$

where $\beta_1$ is the frequency, non-dimensionalized by using the duct diameter and the steady state velocity in the duct. Finally, in Eqs. (A2) and (A3), $p_{s_1}$ and $p_{s_2}$ are the Laplace transforms of the isentropic pressure pulse, as measured by the microphones 1 and 2. It is worth mentioning here that

the Laplace transform (LT) was used in the present analysis. To get the frequency information for a non-periodic signal, as is the present case, the normal procedure is to make use of the Fourier transform (FT) technique. But for the signals generated in the present experiments, the FT does not exist; only the LT exists. Therefore, a method was devised to obtain the LT on the Fourier analyser. The details about the non-existence of FT and the method of obtaining LT are given in Ref. (A2).

According to Eqs. (A2) and (A3), the isentropic admittance coefficient and the reflection coefficient may be evaluated by obtaining the Laplace transforms of the initial pulse, as recorded by two microphones.

The entropy pressure pulse, generated as a result of a cold (or hot) spot interacting with the pressure gradient in the nozzle, was used to estimate the non-isentropic admittance coefficient. The LT of this pulse is given by

$$P_{s_\sigma} = \frac{b_s \gamma_a M_o}{1 - \gamma_a M_o a_s} \sigma_s \tag{A5}$$

where $b_s$ is the non-isentropic admittance coefficient. $\sigma_s$ represents the strength of cold (or hot) spot. The attempt to measure $\sigma_s$ directly had to be abondoned because of several practical problems. Instead, the evaluation of $b_s$ was carried out in an indirect way. It was assumed that $\sigma_s$ could be maintained identical for runs with two different nozzles. This assumption was completely valid for the spark case, as all the source variables could be maintained constant. For the freon case, the freon injection process, for two runs with different nozzles, was compared by monitoring the pressure pulses in the freon line. Figure 6 gives this comparison for the experimental conditions used in Ref. (A2), whereas

GRAPH - A

TYPICAL FREON LINE PHOTOCON'S SIGNALS

GRAPH - B

FOURIER TRANSFORM OF THE PHOTOCON'S SIGNALS

SOLID LINE—WITH TRIAL NOZZLE

DOTTED LINE- WITH ORIFICE PLATE

— Time (msecs) —
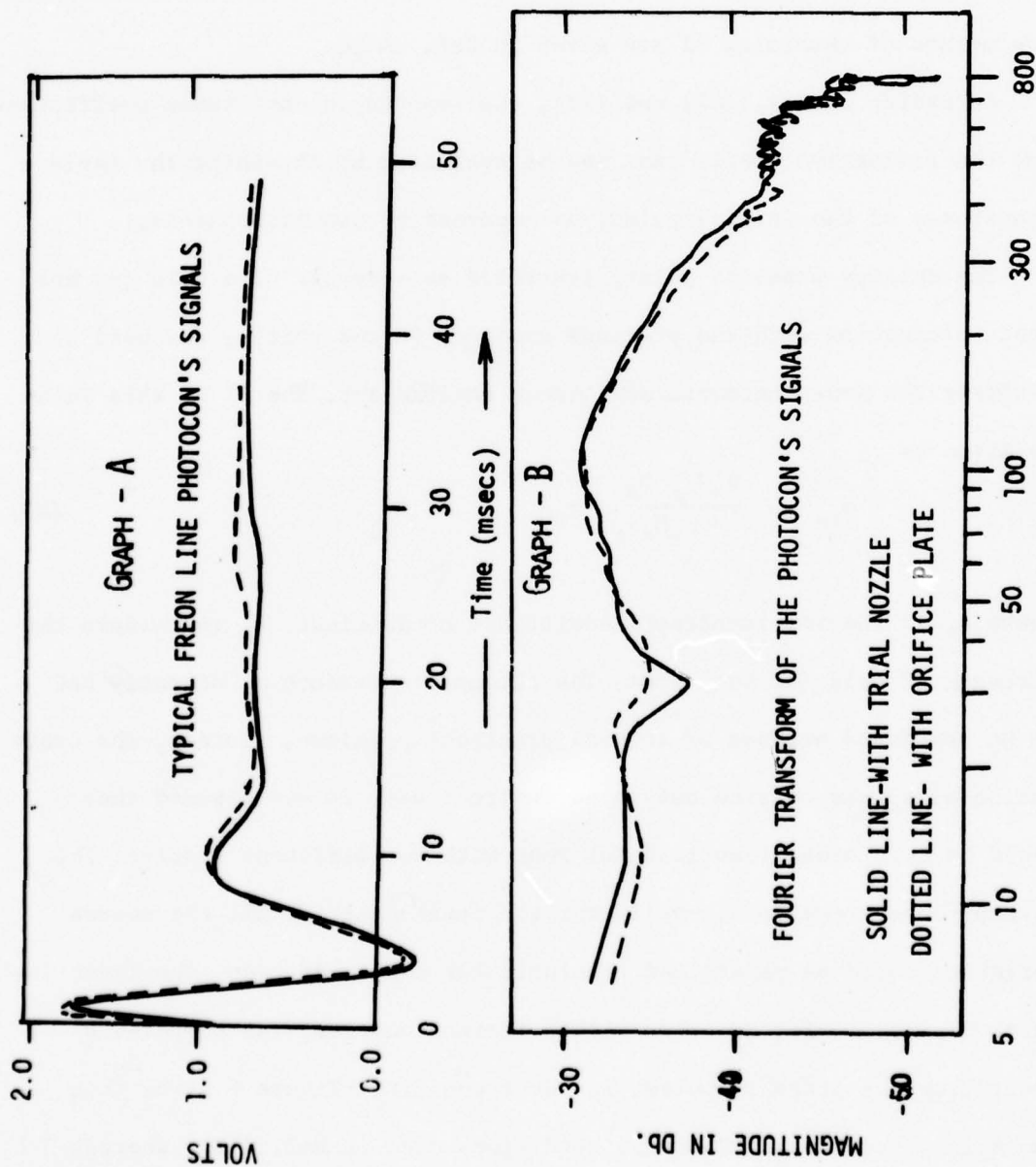
VOLTS

MAGNITUDE IN DB.

FIGURE 6. COMPARISON OF FREON LINE SIGNALS FOR TWO RUNS WITH DIFFERENT NOZZLES.

Fig. 7 gives the same for the present experiments. According to Fig. 6, the above assumption is perfectly valid for the experiments reported in Ref. (A2). However for the present experiments, as Fig. 7 indicates, the validity of the above assumption could not be completely established. The reason is discussed below.

In order to obtain $b_s$ in the present experiments, one run was made with an orifice plate, which simulates the quasi-steady or zero frequency case, and the other one with the conical test nozzle. The exhaust velocity with the orifice plate was about 1000 f/s as compared to a value of 70 f/s for the conical nozzle, as the conical nozzle had a diffuser at its downstream end. This amounted to a much higher static pressure in the entropy tube for the orifice plate as compared to that for the conical nozzle, thereby causing unequal pressure differences across the solenoid for the two runs. Some corrections, as explained in a later section, were incorporated to offset these different experimental conditions. Then with the above assumption, Eq. (A5) leads to the following expression for the non-isentropic admittance coefficient ($bs_t$) for the test nozzle.

$$\frac{b_{s_t}}{b_{s_o}} = \frac{\left(\frac{P_s}{\sigma}\right)_T}{\left(P_{s_\sigma}\right)_o} \quad \frac{1 - \gamma_a \, M_o \, a_{s_t}}{1 - \gamma_a \, M_o \, a_{s_o}} \tag{A6}$$

where $a_{s_o}$ and $b_{s_o}$ are the theoretical admittance coefficients at zero frequency and are given by

$$a_{s_o} = - \frac{\gamma_a - 1}{2 \gamma_a}$$

and

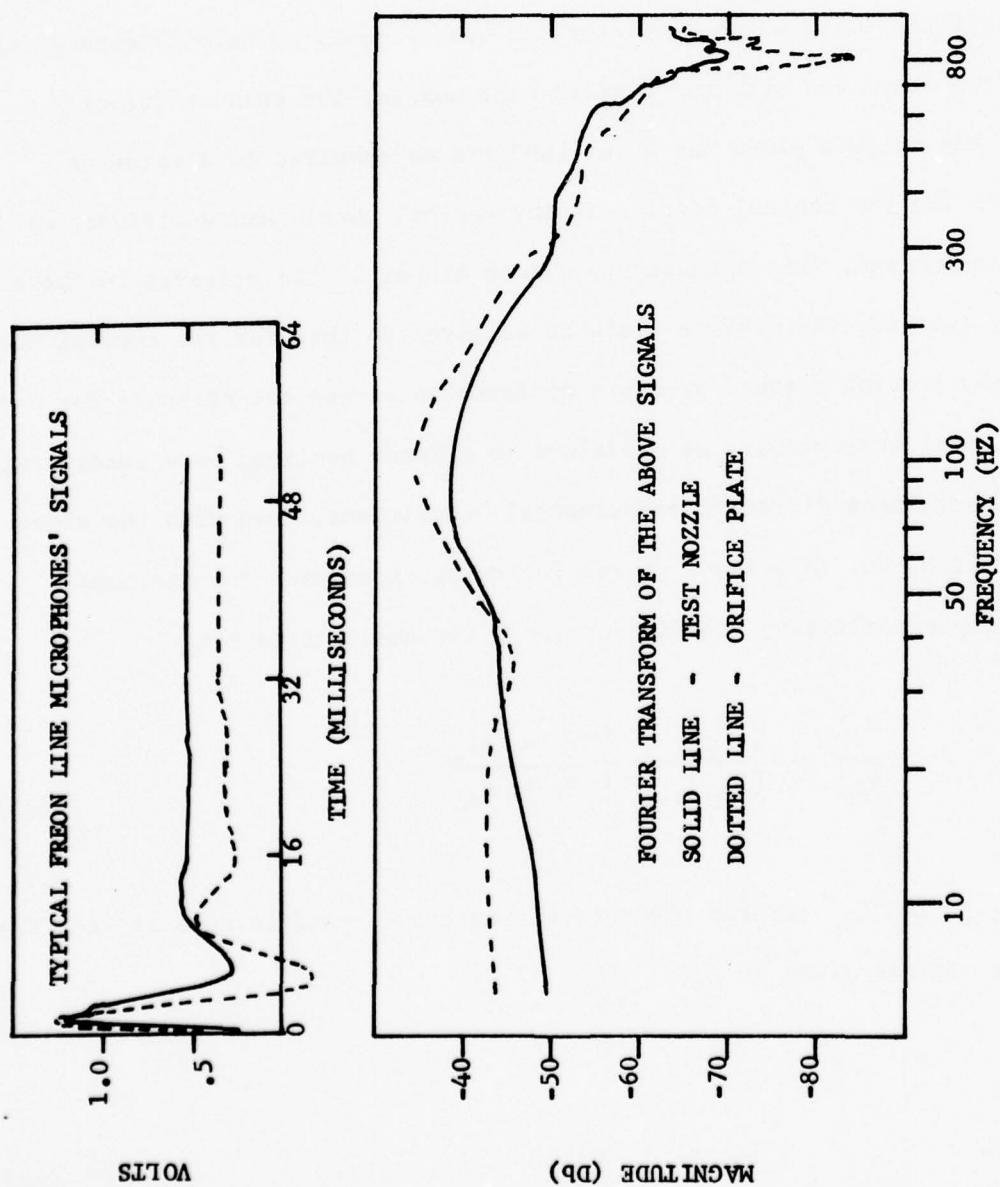$$b_{s_o} = - \frac{1}{2 \gamma_a} \tag{A7}$$

FIGURE 7. COMPARISON OF FREON LINE SIGNALS FOR RUNS WITH THE CONICAL TEST NOZZLE AND AN ORIFICE PLATE.

Thus the non-isentropic admittance coefficient may be evaluated by measuring the Laplace transform of the entropy pressure pulses for the orifice plate and the test-nozzle.

The transmittance coefficient or the transfer function relates the output and input signals for a given nozzle. It may be defined as the ratio of the appropriate transforms of output and input signals. For the isentropic transmittance coefficient the output is the isentropic pressure pulse, transmitted out of nozzle, whereas the input is the incident pressure pulse. Mathematically, it may be written as

$$T_{s_i} = \frac{p_{t_i}}{p_{s_i}} \tag{A8}$$

where $p_{t_i}$ is the transform of the transmitted isentropic pulse and $p_{s_i}$ is the transform of the incident pressure pulse. Now the pulse, monitored by the microphone at the nozzle entrance, contains both the incident pressure pulse ($p_{s_i}$) as well as the reflected pulse ($p_{s_r}$), i.e.

$$p_{s_2} = p_{s_i} + p_{s_r} \tag{A9}$$

where $p_{s_i}$ and $p_{s_r}$ are related through $R_s$ by the equation

$$p_{s_r} = R_s \, p_{s_i} \tag{A10}$$

Use of Eqs. (A9) and (A10) in (A8) gives

$$T_{s_i} = \frac{p_{t_i}}{p_{s_2}} \, (1 + R_s) \tag{A11}$$

Thus the isentropic transmittance coefficient may be evaluated by the appropriate transforms of the initial pulse, as monitored by the various microphones, in combination with $R_s$, which is given by Eq. (A3).

For the non-isentropic transmittance coefficient $(T_{s_\sigma})$, the output is the transmitted non-isentropic pressure pulse, whereas the input is given by $\sigma_s$, the strength of the cold (or hot) spot. With the aid of Eq. (A5), $T_{s_\sigma}$ can be written as

$$T_{s_\sigma} = \frac{p_{t_\sigma}}{p_{s_\sigma}} \frac{b_{s_t} \gamma M_o}{1 - \gamma M_o a_{s_t}} \tag{A12}$$

where $p_{t_\sigma}$ is the transform of the transmitted entropy pressure pulse. The evaluation of $b_{s_t}$ and $a_{s_t}$ for the test nozzle was discussed above. Then using the computed $a_{s_t}$ and $b_{s_t}$ values and the transforms of the entropy pressure pulse, the non-isentropic transmittance coefficient may be evaluated.

## Data Reduction and Analysis

The sequence of the experimental and theoretical steps leading to the evaluation of the acoustical properties of a given nozzle is given in Figs. 8 and 9. Figure 8 illustrates the experimental procedure leading to the evaluation of $a_s$, $R_s$, $b_s$, $T_{s_i}$ and $T_{s_\sigma}$. As shown in Fig. 8, the required transient pulses are generated either by freon injection or by spark discharge. These pulses, inside the tube and outside in an anechoic chamber, are monitored by various microphones and recorded on magnetic tape. The recorded data is digitised and properly averaged in the Fourier analyser (see Ref. (A2) for details). After separating the isentropic and the non-isentropic pulses, their Laplace transforms (LT) are obtained. These LT values are used in Eqs. (A2), (A3) and (A6) to yield the nozzle admittance coefficients. Similarly, the LT of the isentropic and non-isentropic transmitted pulses, in combination with the derived nozzle admittance values, is used in Eqs. (A11) and (A12) to obtain the transmittance coefficients.
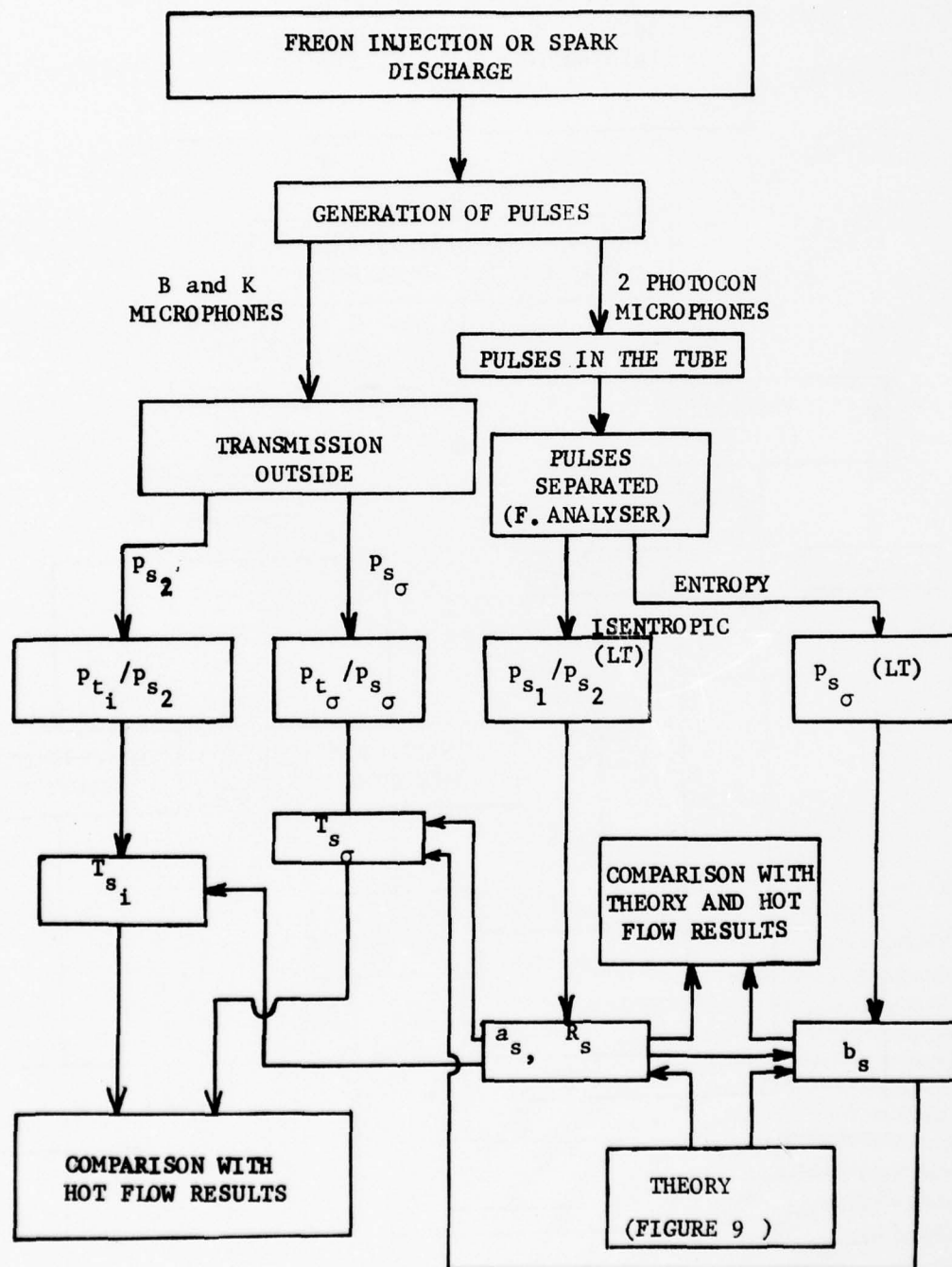
FREON INJECTION OR SPARK DISCHARGE

GENERATION OF PULSES

B and K MICROPHONES

2 PHOTOCON MICROPHONES

PULSES IN THE TUBE

TRANSMISSION OUTSIDE

PULSES SEPARATED (F. ANALYSER)

$p_{s_2}$

$p_{s_\sigma}$

ENTROPY

ISENTROPIC (LT)

$p_{t_i}/p_{s_2}$

$p_{t_\sigma}/p_{s_\sigma}$

$p_{s_1}/p_{s_2}$

$p_{s_\sigma}$ (LT)

$T_{s_\sigma}$

$T_{s_i}$

COMPARISON WITH THEORY AND HOT FLOW RESULTS

$a_s, R_s$

$b_s$

COMPARISON WITH HOT FLOW RESULTS

THEORY (FIGURE 9 )

FIGURE 8. SCHEMATIC OF THE EXPERIMENTAL PROCEDURE.
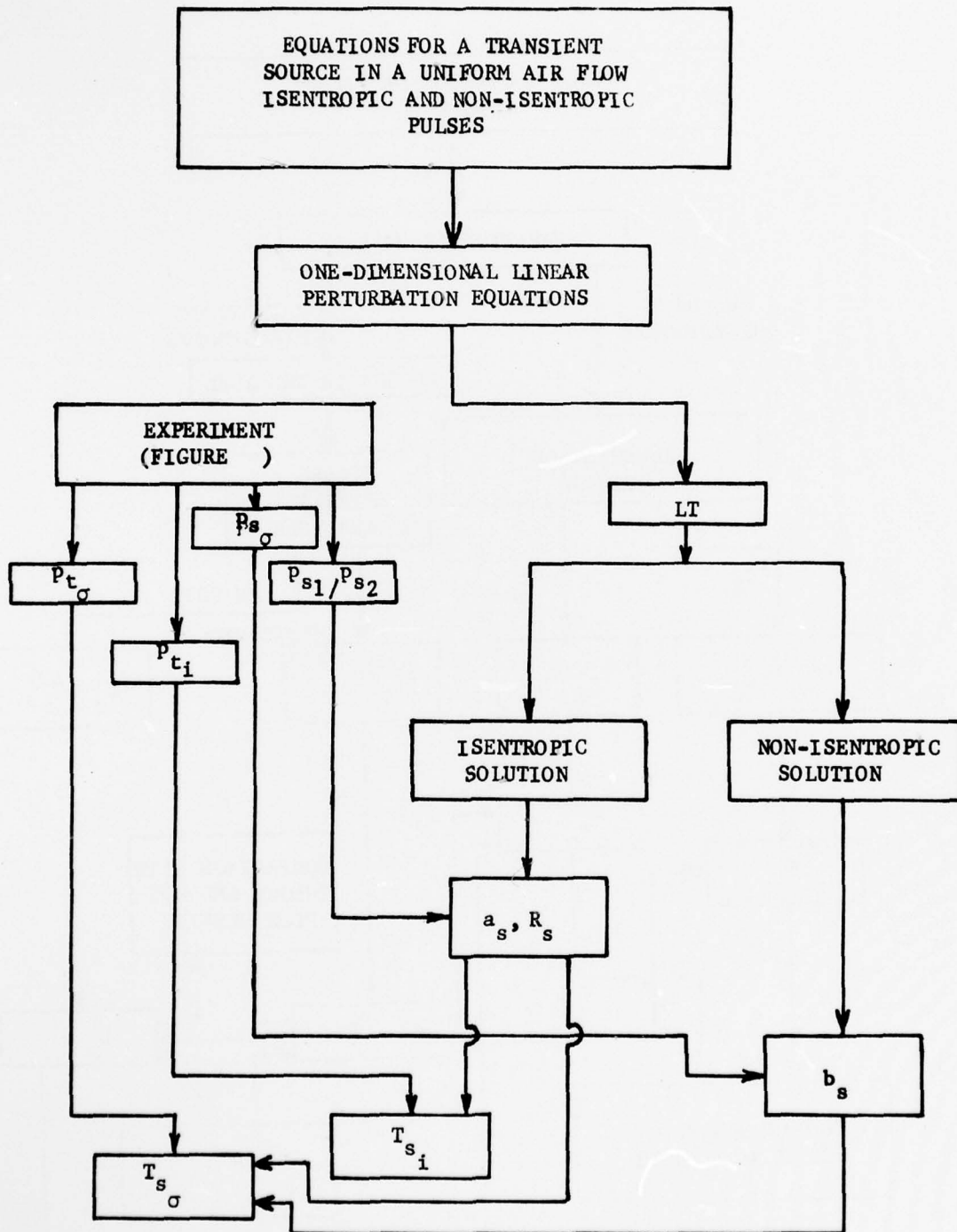
FIGURE 9. SCHEMATIC OF THE THEORETICAL PROCEDURE.

Figure 9 lists, briefly, the steps involved in the theoretical formulation, which uses the experimental results to yield the desired nozzle properties. The data acquisition, reduction and analysis procedure is illustrated in Fig. 10.

## Results and Discussion

The results obtained by using the experimental data and the theoretical relations are shown in Figs. 11-23. Wherever possible, the corresponding theoretical values, obtained independently, are also plotted. For these plots, a dimensionless frequency ($\beta$) has been used. It is defined by the relation

$$\beta = \frac{\omega}{d\bar{u}/dx} \tag{A13}$$

where $\omega$ is the frequency in radians per second and $\frac{d\bar{u}}{dx}$ is the steady state velocity gradient for a given nozzle. Since $\frac{d\bar{u}}{dx}$ is, in general, not constant in the nozzle, only an overall or an effective $\frac{d\bar{u}}{dx}$ can be used in Eq. (A13). The importance of using $\beta$ becomes obvious if it is mentioned that the quasi-steady or zero frequency case corresponds to $\beta \rightarrow 0$, rather than $\omega \rightarrow 0$. Essentially, the velocity gradient, an important parameter in the noise response studies, is thus incorporated in the above definition.

In the theoretical evaluation of nozzle admittance coefficients (see Refs. (A2)), $d\bar{u}/dx$ is assumed to be a constant. A nozzle, with a constant $\frac{d\bar{u}}{dx}$, is termed here as a linear nozzle. This simplifies the theoretical evaluation considerably. For a linear nozzle, Eq. (A13) reduces to

$$\beta = \frac{\omega \, x^*}{a^*} \tag{A14}$$

where $a^*$ is the speed of sound at the nozzle throat. $x^*$ is the distance between the throat and the location of zero $\bar{u}$. This location is easily calculable for a linear nozzle.
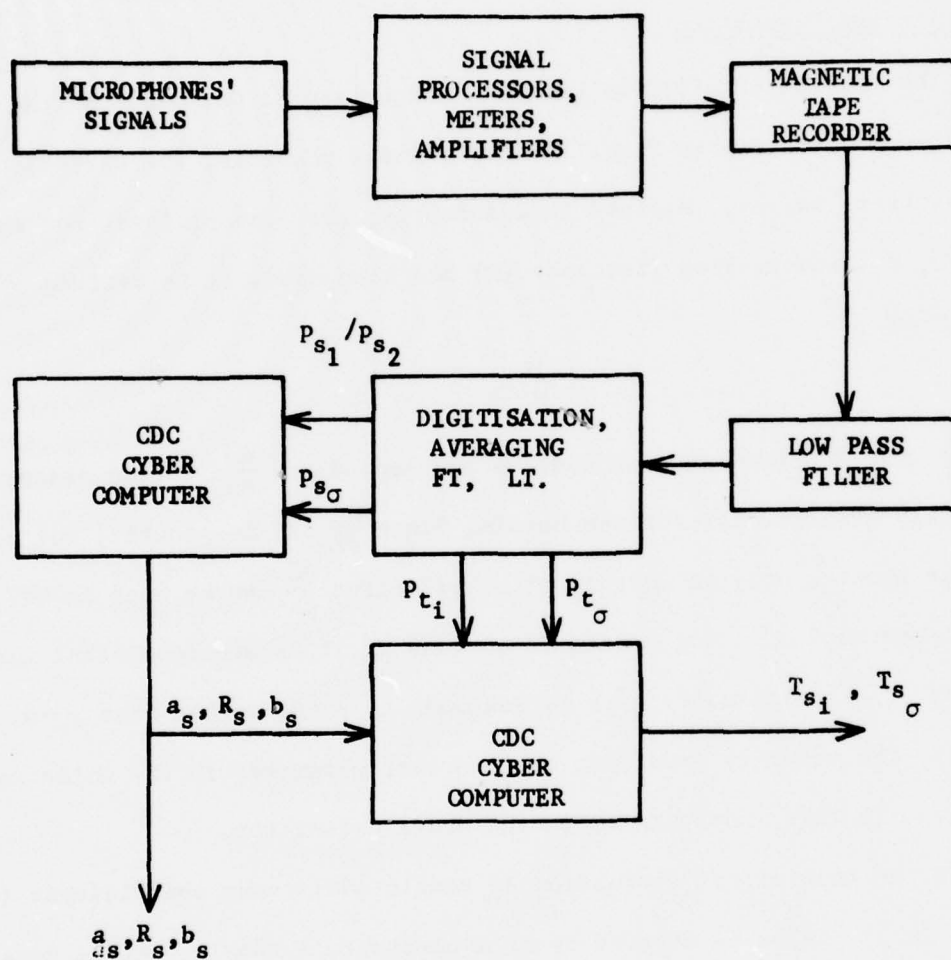
FIGURE 10. SCHEMATIC OF THE DATA ACQUISITION AND
REDUCTION PROCEDURE.

In the entropy tube experiments, it was required to simulate the conditions of the hot flow experiments, where a conical nozzle was employed. For the conical nozzle, it was assumed, as an approximation, that $x^*$ represents the nozzle length. This, in fact, defines an effective $d\bar{u}/dx$ in Eq. (A13). Then, for the hot flow experiments, where the results are obtained for a frequency range of 0-2000 Hz, the $\beta$ values range from 0 to 1.8. Before discussing any results, it should be pointed out again that for the entropy tube experiments, a conical nozzle was used, whereas the theoretical results were obtained for a linear nozzle. Whenever the experimental results are compared with the corresponding theoretical values, this difference in the experimental and theoretical nozzles must be borne in mind.

## Results From Freon Injection Experiments

As mentioned earlier, the evaluation of $p_{s_1}/p_{s_2}$ will determine $a_s$ and $R_s$. Hence, $p_{s_1}/p_{s_2}$, obtained experimentally as a function of $\omega_h$ (Hz) and $\beta$, is plotted in Fig. 11. Also shown in this figure, is the theoretically estimated $p_{s_1}/p_{s_2}$, (the procedure to obtain theoretical $p_{s_1}/p_{s_2}$ is described in Ref. (A2)). According to Fig. 11, the experimental and the theoretical $p_{s_1}/p_{s_2}$ agree reasonably well up to a frequency of 225 Hz. This corresponds to a $\beta$ value of about .50. This frequency limit was imposed by the nature of the initial pressure pulse, generated by the freon injection apparatus. For frequencies higher than 225 Hz, the smallest resolvable value in the Fourier analyser dominated the initial pulse components. Both the experimental and the theoretical $a_s$ values are plotted in Fig. 12. The corresponding reflection coefficients are shown in Fig. 13. The amplitude of $a_s$, obtained experimentally, shows an acceptable agreement with the theory for frequencies between 100 and 250 Hz. The reason for an unacceptable variance
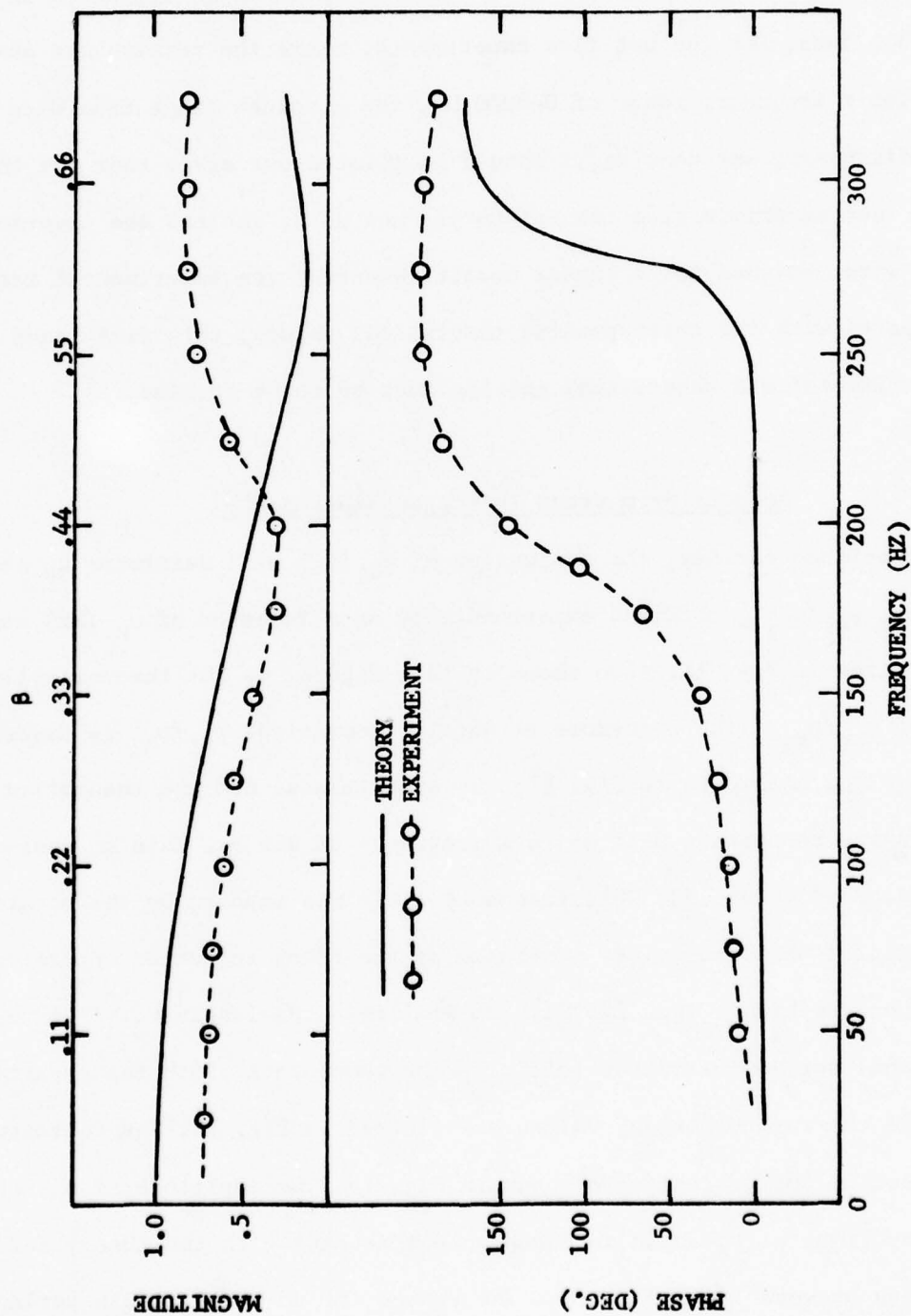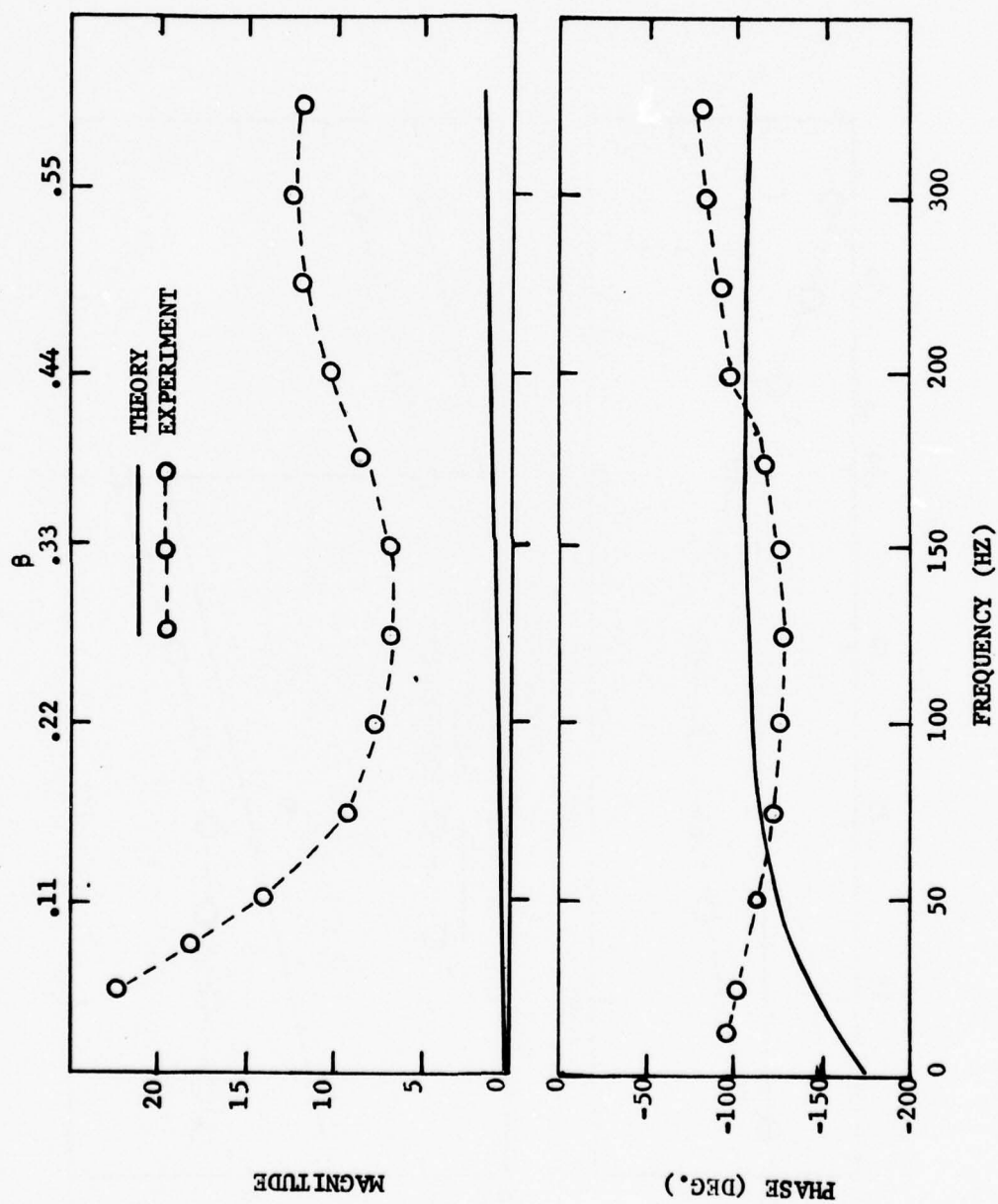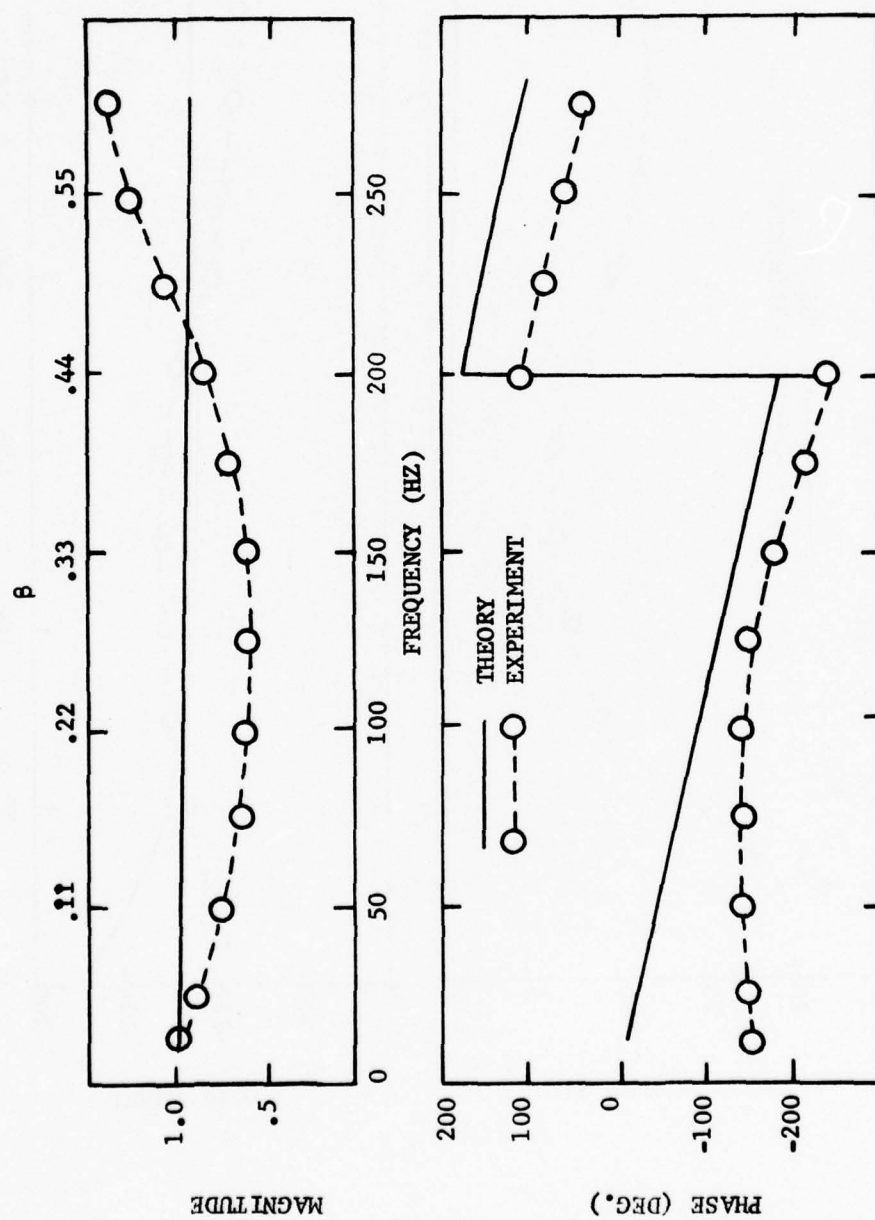
FIGURE 11. RATIO OF THE LAPLACE TRANSFORMS OF THE ISENTROPIC PRESSURE PULSE, AS MONITORED BY TWO DUCT MICROPHONES. FREON INJECTION CASE.

FIGURE 12. ISENTROPIC ADMITTANCE COEFFICIENT ($a_g$) FOR THE FREON INJECTION CASE

FIGURE 13. REFLECTION COEFFICIENT ($R_s$) FOR THE FREON INJECTION CASE.

at lower frequencies lies in the behavior of the second term in Eq. (A2). At low frequencies, $p_{s_1}/p_{s_2}$ is very close to unity. This gives an indeterminate form $\frac{0}{0}$ to that term in Eq. (A2). As a result, a small error in $p_{s_1}/p_{s_2}$ estimate gets magnified to a large number for $a_s$. Also, as Fig. 12 indicates, between 100 and 250 Hz, the quantitative agreement between experiment and theory is poor; the reason being the $\frac{1}{\gamma a M o}$ factor in Eq. (A2). For the present experiments, this factor has a value of about 116, which means that a small error in $p_{s_1}/p_{s_2}$ evaluation gets multiplied by a factor of about 116, thereby causing a poor quantitative agreement. However, the $a_s$ phase is not affected by this factor, and thus shows a better agreement with theory. The conclusions are further supported by the $R_s$ plots in Fig. 13. As the error magnification reasoning does not apply to the $R_s$ evaluation, Fig. 13 shows a much better accord between experiment and theory. As mentioned in the beginning of this section, another possible cause for the disagreement, between the experiment and theory, could be the fact that the theoretical and experimental nozzles were not matched exactly. It is not possible, with the theory used, to predict the error caused by this mismatch. However, in Ref. (A2), where the nozzles were matched, better results were obtained.

To estimate the non-isentropic admittance coefficient, freon injection runs were made with the orifice plate and the test nozzle. The corresponding $(p_{s_\sigma})_0$ and $(p_{s_\sigma})_T$, thus evaluated, were used in Eq. (A6) to obtain $b_{s_t}/b_{s_0}$. At low frequencies, $M_0$ and $a_{s_t}$ (or $a_{s_0}$) are both of the order of .1. Thus the term $\gamma_a M_0 a_{s_t}$ (or $\gamma_a M_0 a_{s_0}$), being small compared to unity, was neglected in Eq. (A6). As mentioned in a previous section, the underlying assumption (that $\sigma_s$ is same for runs with different nozzles) could not be completely satisfied in the present experiments. To offset the effect of unequal pressure differences across the solenoid for the orifice plate and the conical

nozzle, some corrections were included. These corrections were based on the shock tube relations, as given in Ref. (A4). The final corrected experimental $b_{s_t}/b_{s_o}$ as well as the corresponding theoretical values are shown in Fig. 14. According to this figure, the $b_{s_t}$ values for the conical nozzle are reasonably acceptable up to a frequency of 175 Hz ($\beta \approx .4$). Above this frequency, the smallest resolvable value in the Fourier anayser again dominated the entropy pressure pulse components.

Next, by using the experimental $p_{t_i}/p_{s_2}$ and the theoretical $R_s$ values in Eq. (A11), the isentropic transmittance coefficient was obtained. As shown in Fig. 15, the amplitude of $T_{s_i}$ increases with frequency, except between 150-250 Hz, where it seems to go through a minimum. This can be explained by a closer look at Eq. (A11) and Fig. (13). In the range 150-250 Hz, $R_s$ has a phase of about $180^o$, which means that the term $(1 + R_s)$ in Eq. (A11) is close to zero. Consequently, the $T_{s_i}$ magnitude is small. Actually, both $(1 + R_s)$ and $p_{s_2}$ should have been close to zero, thereby giving a 0/0 form to the right hand side of Eq. (A.11). But the error in the experimental evaluation of $p_{s_2}$ (though $p_{s_2}$ does have a small value, as indicated by Fig. 16) makes the value of $\dfrac{p_{t_i}}{p_{s_2}}$ to be finite and thus causes $T_{s_i}$ to be small. Moreover it is important to point out that the use of the experimental $R_s$ instead of the theoretical one seems to yield, as shown in Fig. 17, much more acceptable $T_{s_i}$ values in the troublesome frequency range. There is nothing strange about this behavior; the errors in the experimental evaluation of $(1 + R_s)$ and $p_{s_2}$ possibly cause the amplitudes of these two terms to be non-zero and thus improve the $T_{s_i}$ evaluation in that frequency range.

The results for the non-isentropic transmittance coefficient $T_{s_\sigma}$, for the freon case, are shown in Fig. 18. $T_{s_\sigma}$ was evaluated by employing the experi-
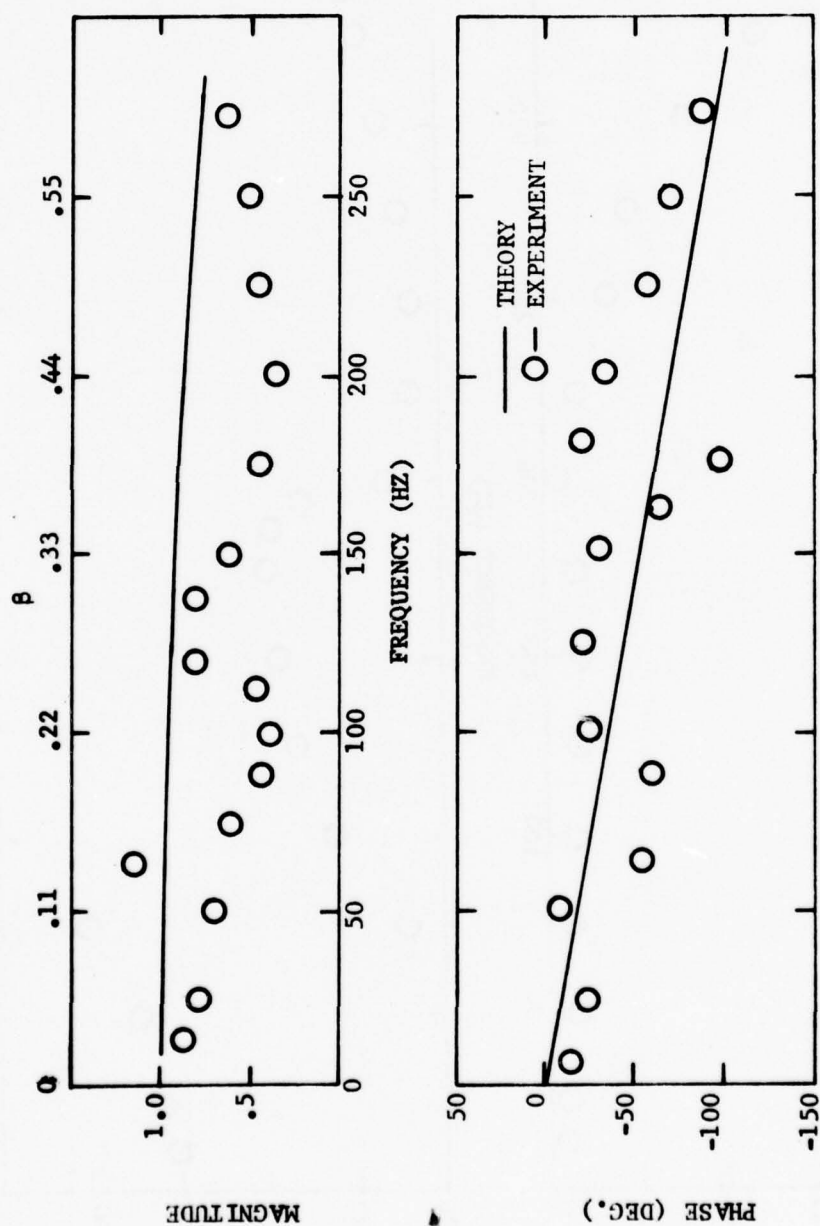
FIGURE 14. NON-ISENTROPIC ADMITTANCE COEFFICIENT $(b_{s_t}/b_{s_o})$ FOR THE FREON INJECTION CASE.
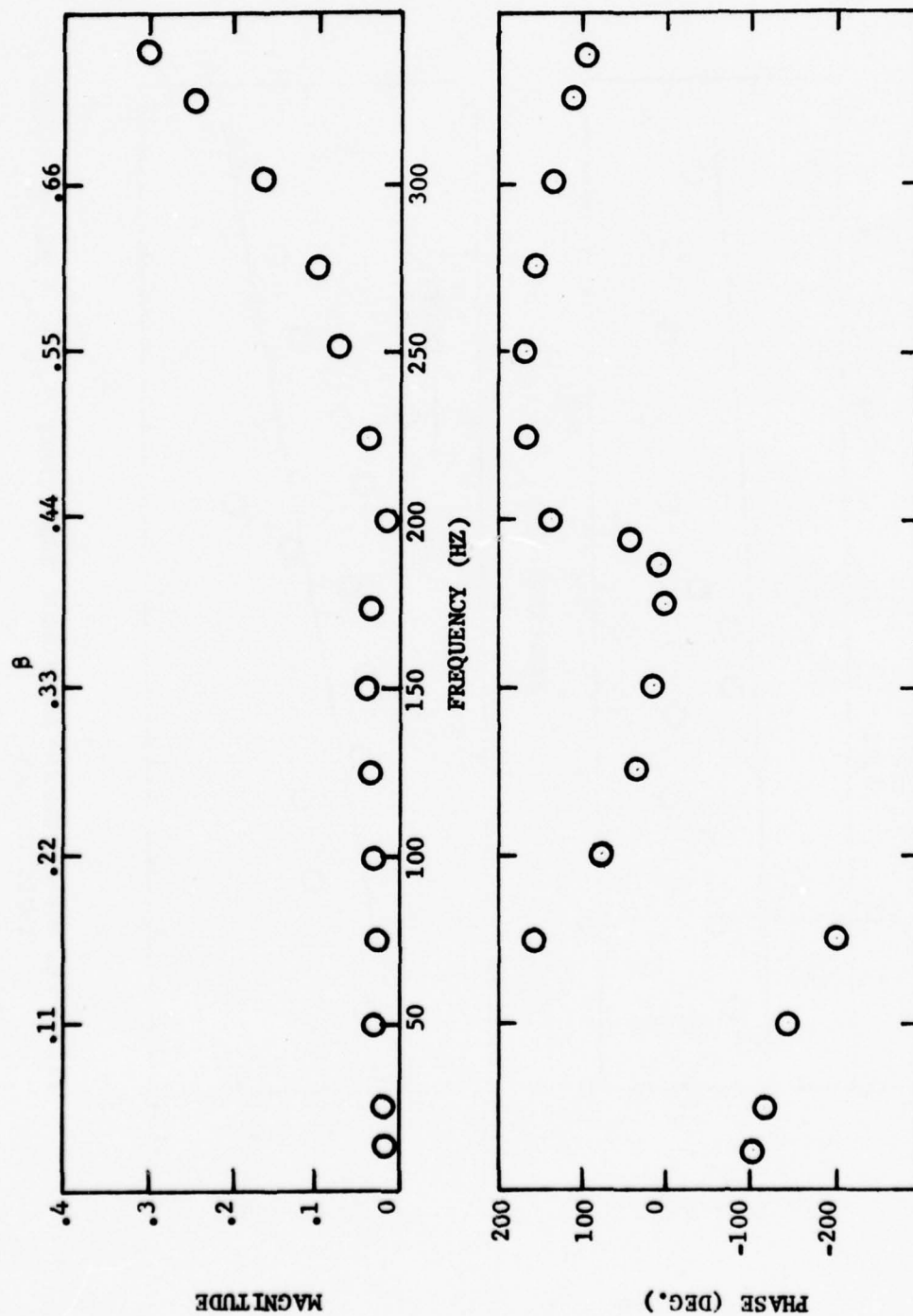
FIGURE 15. ISENTROPIC TRANSMITTANCE COEFFICIENT ($T_{s_1}$), OBTAINED BY USING THEORETICAL $R_s$. FREON INJECTION CASE.
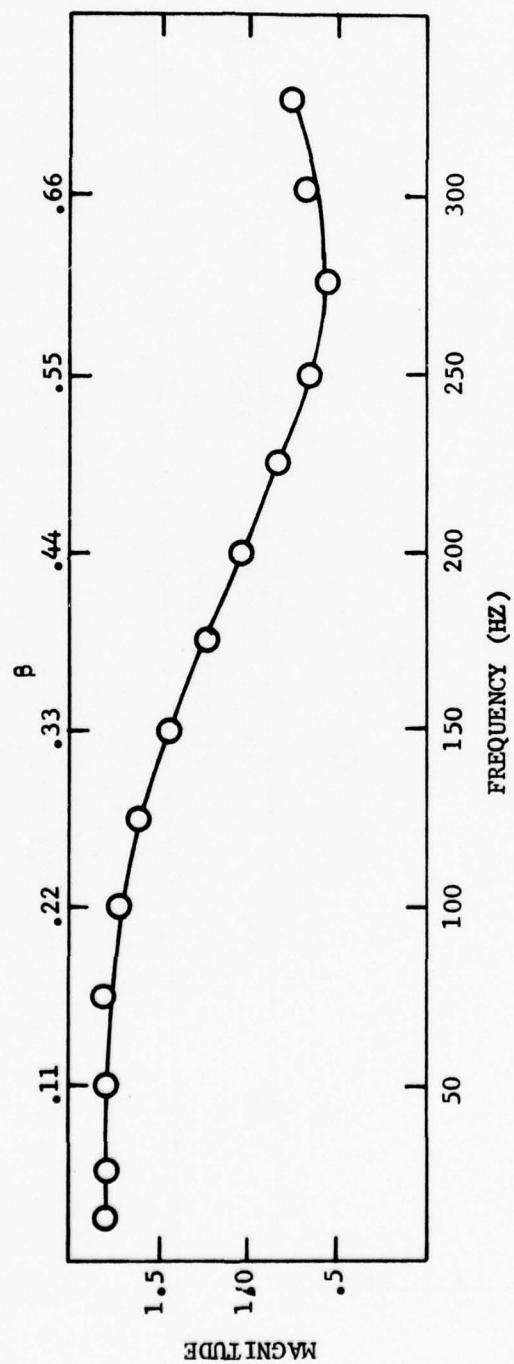
FIGURE 16. LAPLACE TRANSFORM OF THE ISENTROPIC PRESSURE PULSE FOR FREON INJECTION.
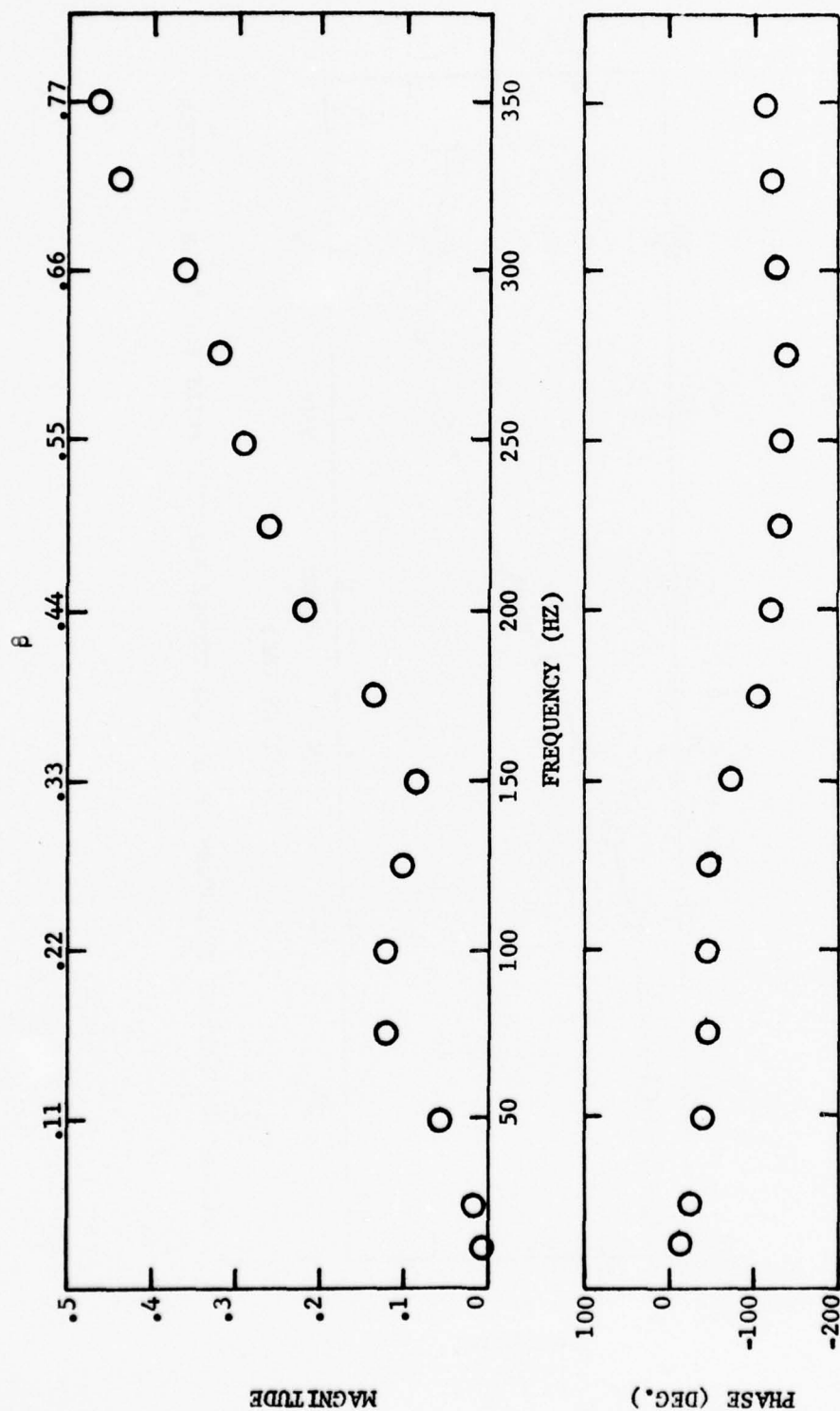
FIGURE 17. ISENTROPIC TRANSMITTANCE COEFFICIENT ($T_{s_i}$), OBTAINED BY USING EXPERIMENTAL $R_s$. FREON INJECTION CASE.
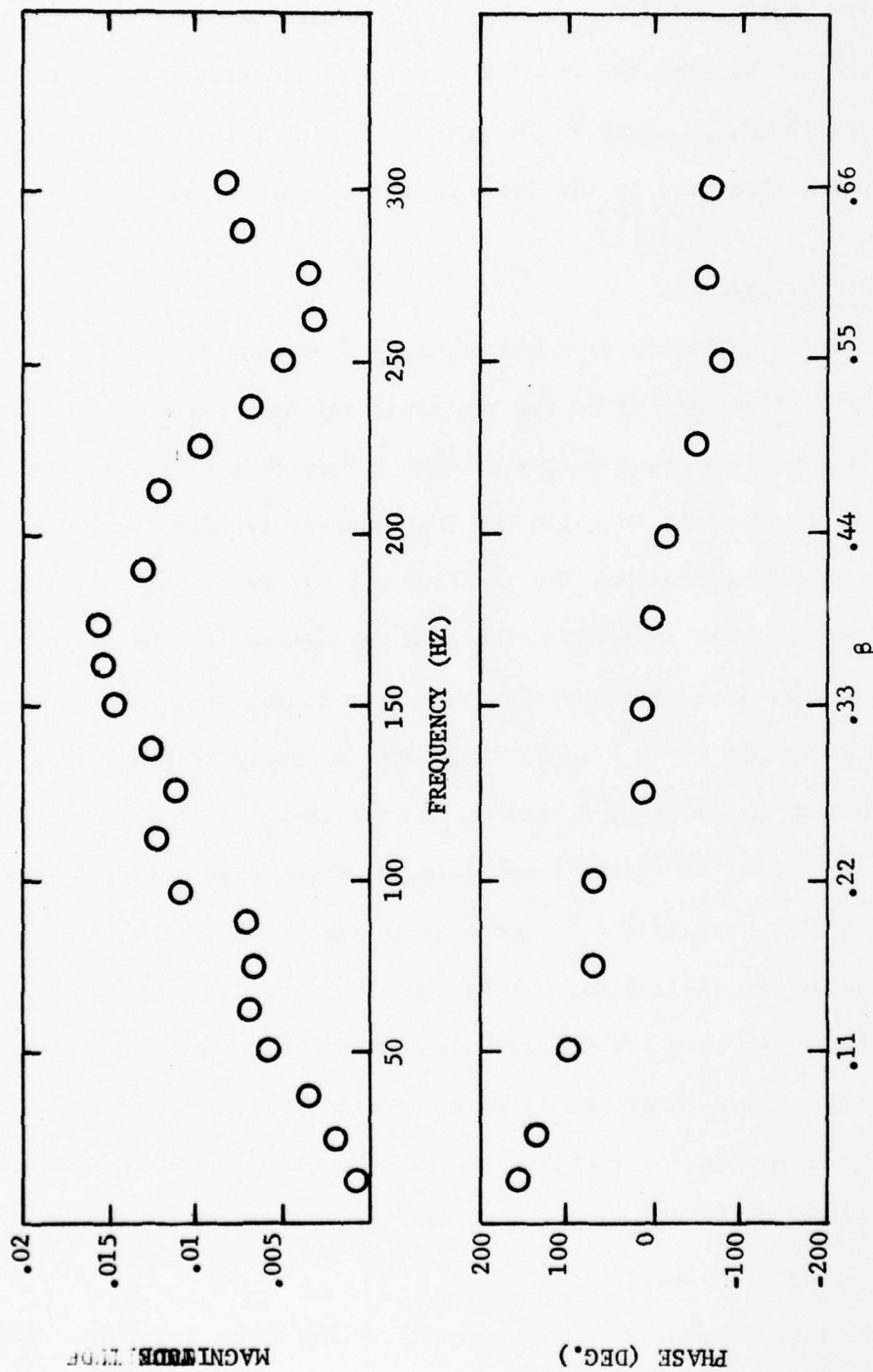
FIGURE 18. NON-ISENTROPIC TRANSMITTANCE COEFFICIENT ($T_{s_\sigma}$) FOR FREON INJECTION CASE.

mental $p_{t_\sigma}/p_{s_\sigma}$ and the theoretical $a_{s_t}$ and $b_{s_t}$ values (the reason for not using the experimental $a_{s_t}$ and $b_{s_t}$ is discussed in Ref. (A2)) in Eq. (A12). According to Fig. 18, the results seem to be acceptable up to a frequency of 175 Hz ($\beta \approx .4$), which is the upper limiting value for the entropy pressure pulse, generated by the freon injection apparatus.

Spark Discharge Data:

The freon injection data had an upper frequency limit of 225 Hz for the isentropic pulse and 175 Hz for the non-isentropic pulse. This frequency limit is apparatus dependent, i.e. with a reduction in the rise time of the pulse, it is possible to raise the frequency limit. The spark discharge provides a good illustration. The isentropic pressure pulse generated by the spark discharge has a shorter rise time as compared to the one obtained by freon injection. Consequently, the upper frequency limit for the spark case is about 350 Hz ($\beta \approx .75$). Therefore, as shown in Figs. 19-21, theory and experiment, for $\frac{p_{s1}}{p_{s2}}$, $a_s$ and $R_s$ evaluations, agree reasonably well up to 350 Hz. Again, as in the freon case, at frequencies close to zero, the experimental $a_s$ values are not acceptable because of the $\frac{0}{0}$ form of the right hand side of Eq. (A2). Also, between 50-350 Hz, the experimental $a_s$ is consistently higher than its theoretical counterpart, because the term $\frac{1}{\gamma a M_0}$, in Eq. (A2), has a large value. This has also been pointed out, when the freon results were discussed. Furthermore, in Ref. (A2), where experimental and theoretical conditions were matched exactly, the spark discharge method yielded better results.

Following the same procedure as used in the freon injection case, the isentropic transmittance coefficient $T_{s_i}$ was computed. Figure (22) shows the magnitude and phase of $T_{s_i}$, obtained by using the theoretical $R_s$ values.
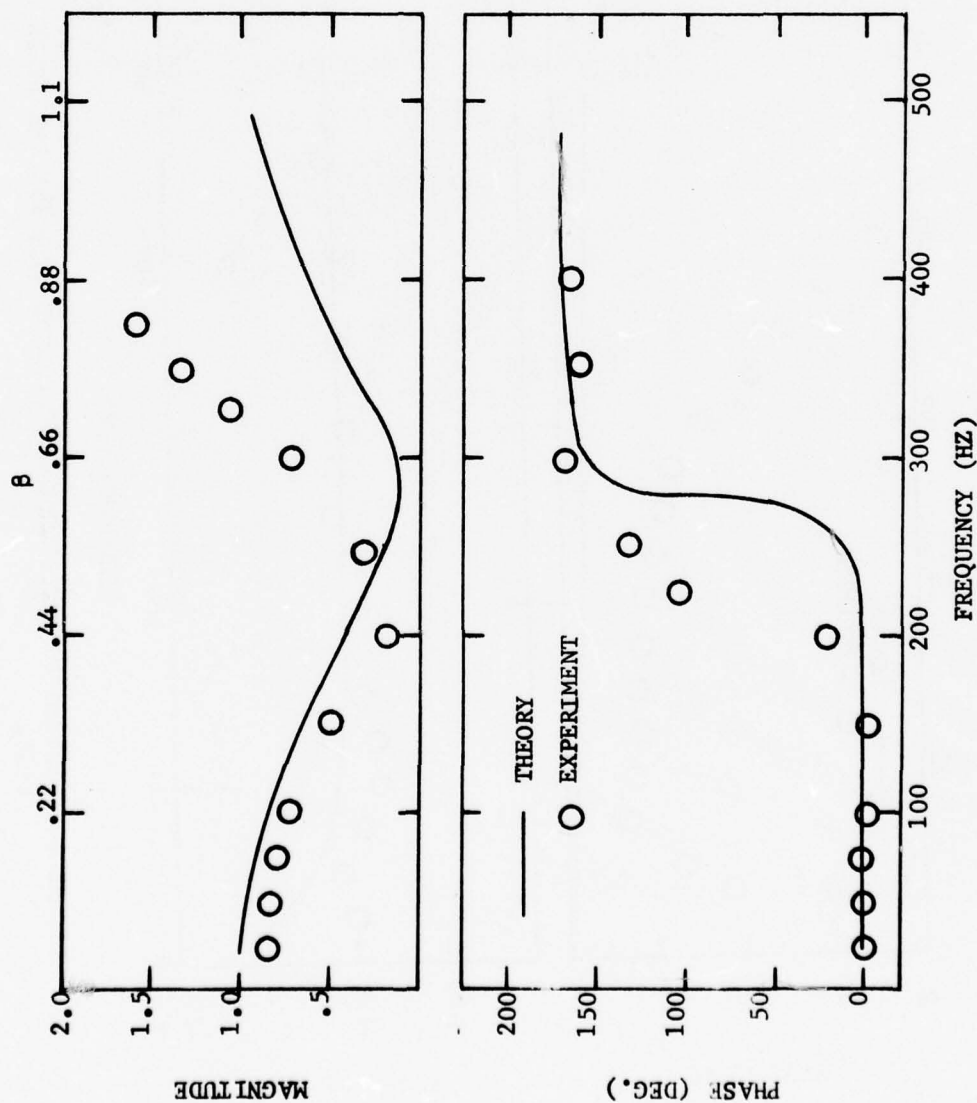
FIGURE 19. RATIO OF THE LAPLACE TRANSFORMS OF THE ISENTROPIC PRESSURE PULSE, AS MEASURED BY TWO DUCT MICROPHONES FOR SPARK CASE.
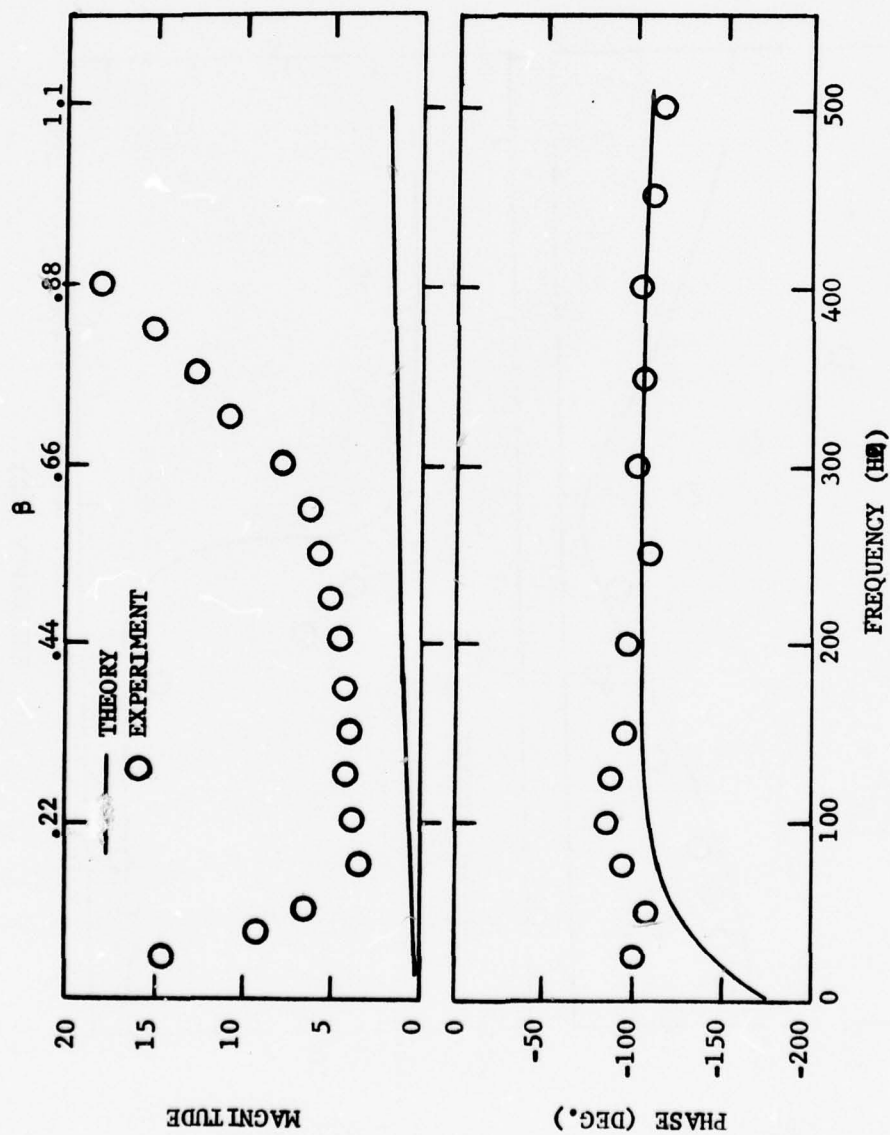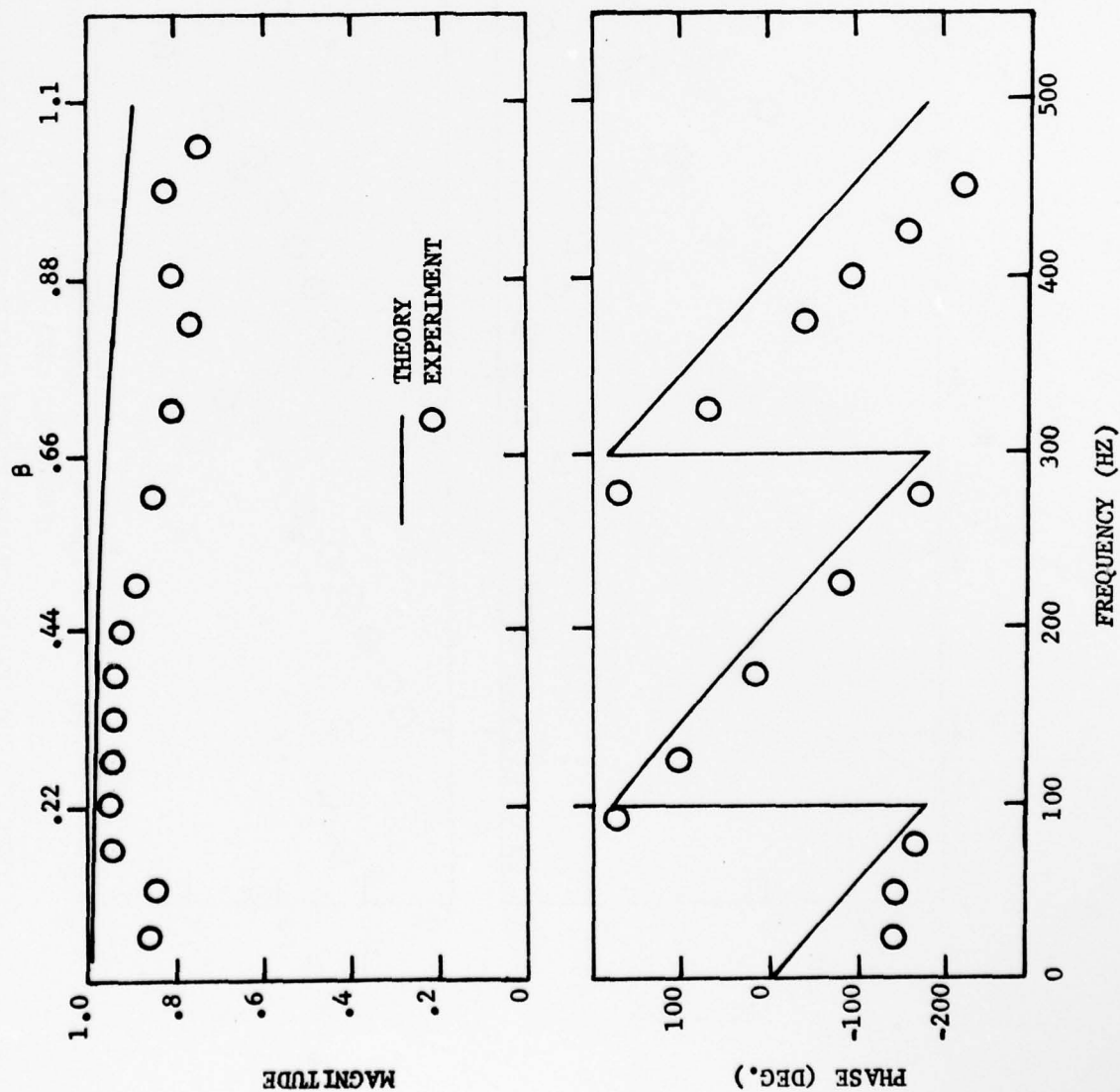
FIGURE 20. ISENTROPIC ADMITTANCE COEFFICIENT ($a_s$) FOR THE SPARK
CASE.

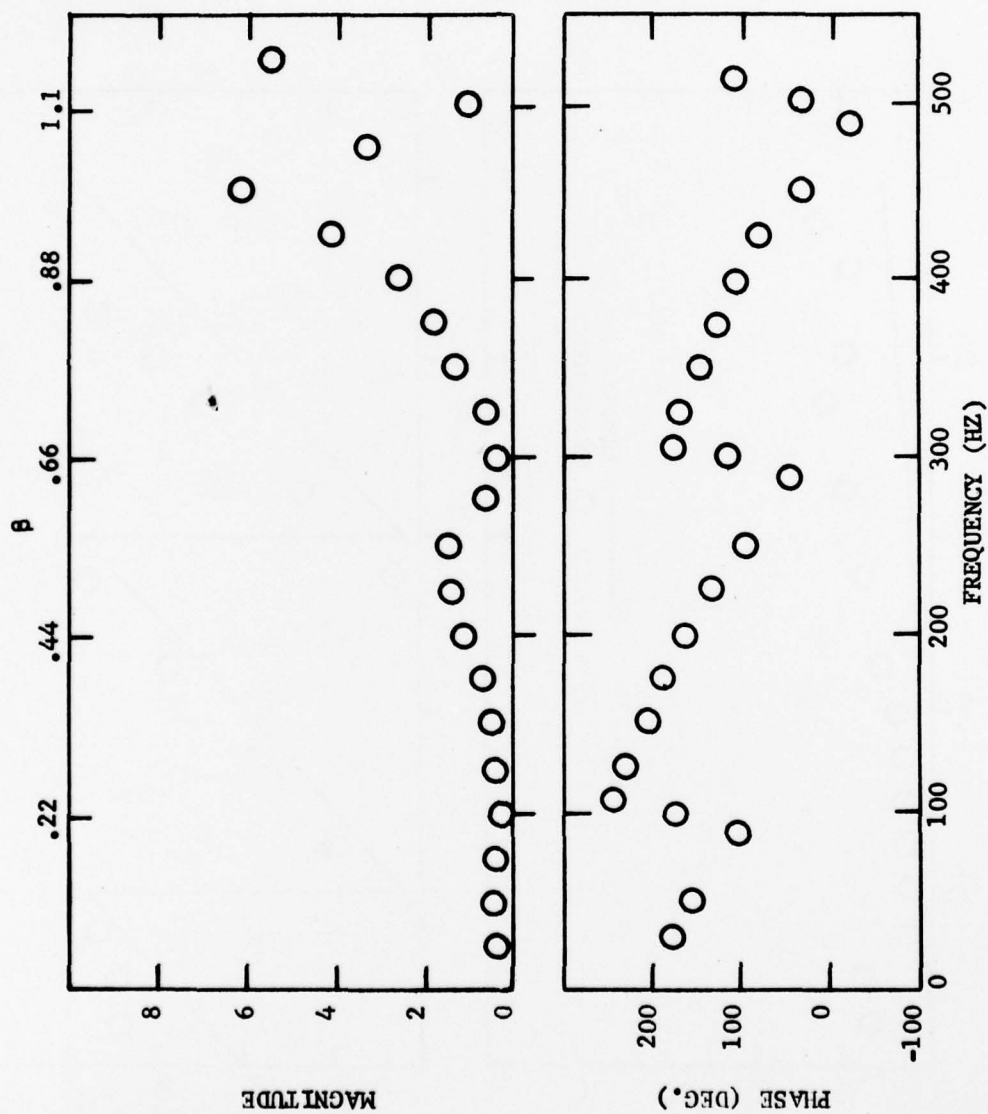FIGURE 21. REFLECTION COEFFICIENT ($R_s$) FOR THE SPARK CASE.

FIGURE 22. ISENTROPIC TRANSMITTANCE COEFFICIENT ($T_{si}$), OBTAINED BY USING THEORETICAL $R_s$. SPARK CASE.
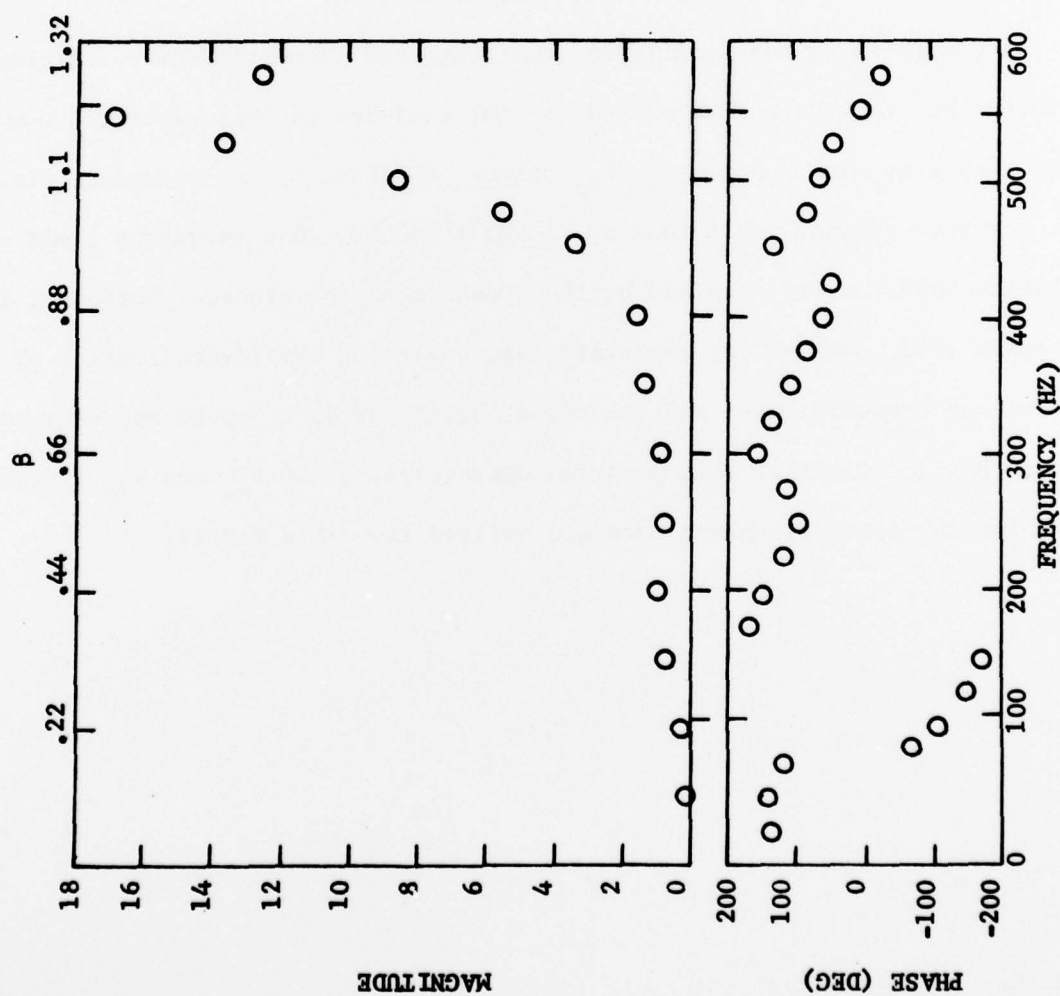
FIGURE 23. ISENTROPIC TRANSMITTANCE COEFFICIENT ($T_{s_i}$), OBTAINED BY USING EXPERIMENTAL $R_s$. SPARK CASE.

The upper acceptable frequency for $T_{s_i}$, with spark discharge, is about 500 Hz ($\beta = 1.1$) as compared to 350 Hz with freon injection. Again, as shown in Fig. (22), the $T_{s_i}$ magnitude becomes small at frequency values of 100, 300 and 500 Hz, where the $R_s$ phase is close to $180^\circ$. The reason for the objectionably small $T_{s_i}$ values at these frequency points becomes obvious if one follows the discussion of the preceding section. Moreover, as shown in Fig. (23), an improvement in the $T_{s_i}$ values at these three points seems possible if the experimental $R_s$ is preferred over its theoretical counterpart.

The estimates of non-isentropic admittance and transmittance coefficients by using the spark discharge method are not included in this report. A few trial runs were made and the $b_{s_t}/b_{s_o}$ values, obtained by the procedure discussed in a previous section, were good up to about 150 Hz. This frequency limit was no better than the one obtained by the freon injection process. Moreover, for the spark case, some of the uncertainties, regarding the identification of the entropy pressure pulse and the repeatability of data, could not be resolved within the time limit of this program. Consequently, the $b_{s_t}$ and $T_{s_\sigma}$ evaluations for the spark discharge case are omitted from this report.

## References

1. Crocco, L. and Sirignano, W. A., "Behavior of Super-Critical Nozzles Under Three-Dimensional Oscillatory Conditions," AGARDograph No. 117, NATO, 1967.

2. Aggarwal, S. K., "An Evaluation of Nozzle Response to Transient Disturbances," Ph.D. Thesis, Georgia Institute of Technology, Under Publication.

3. Strahle, W. C., Muthukrishnan, M., Neale, D. H. and Ramachandra, M. K., "An Investigation of Combustion and Entropy Noise," NASA CR-135220.

4. Liepmann, H. W. and Roshko, A., "Elements of Gas Dynamics," John Wiley and Sons, Inc. 1967.

## Appendix B

## Cooled Film Probe Results

### Basic Theory of Cooled Film Measurements

The main objective of the cooled film measurements is to obtain the impedance condition at the nozzle entrance. This requires the knowledge of pressure, temperature and velocity fluctuation details. The pressure and temperature fluctuations were measured through Photocon transducers and thermocouples, whereas the velocity fluctuations were to be obtained through cooled film measurements.

The cooled film anemometer is a device to make velocity fluctuation measurements in high temperature environments similar to those obtainable at normal temperatures with a hot wire or hot film anemometers. The normal hot wire or film is limited by the maximum operating temperature of the sensor. Since the actual measurement depends on the heat transfer mechanism, a non-cooled sensor must be operated at higher than environmental temperatures. The cooled sensor circumvents this problem by adding an internal heat sink so that its surface is actually below the temperature of the environment. In this manner it is possible to expose sensors to very high temperature environments, the only limitation being the maximum cooling rate that can be applied to the sensor.

The sensing element consists of a pyrex-u-tube, 15 mm diameter, through which a cooling fluid can be circulated. On one leg of this U-tube a platinum film of one micron thickness and 1.5 mm length is deposited and a gold coating on the rest of the tube serves as the

electrical contact. With the coolant circulating through the sensor, the platinum film is maintained at constant resistance (and hence constant temperature) by means of a bridge circuit, of which the sensor forms a part, and a feedback system which utilizes voltage and power amplifiers to maintain bridge balance. According to its manufacturers (TSI), the frequency response of this heat flux system is rated at 50 kHz.

Figure 1 shows the arrangement of the cooled film sensor and the coolant system. The basic heat transfer mechanism involved in the cooled film measurements is illustrated in Fig. 2. The heat transfer relation can be written as,

$$P + Q_E = Q_c \tag{1}$$

where

$P$ = electrical power input to the sensor = $\left( \dfrac{E}{2+R} \right)^2 R$ (2)

$E$ = Bridge voltage

$R$ = Sensor resistance

$Q_c$ = Heat transferred from the sensor surface to the cooling fluid

$Q_E$ = Heat transferred from the environment to the sensor surface. (2)

In the absence of any heat transfer between the film and the environment, the electrical power supplied to the film element is dissipated by the coolant circulating through the sensor. When this element is exposed to environmental conditions such that a power transfer between the environment and the element occurs, the power supplied to the element by the heat flux system is adjusted so that the power
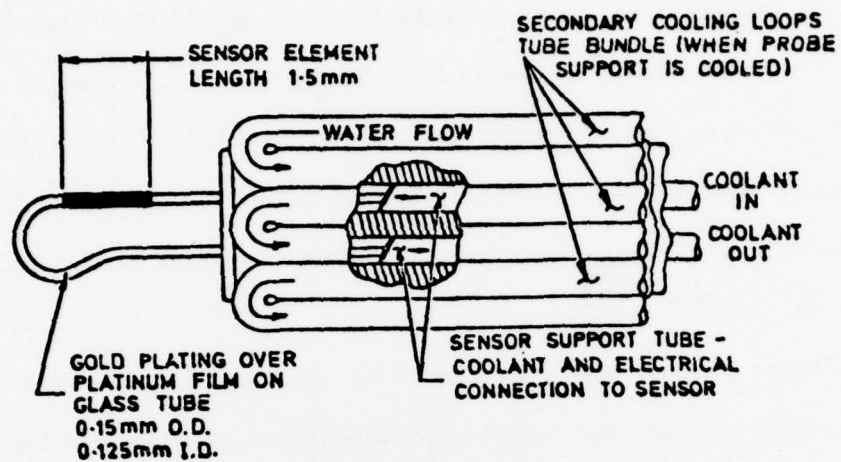
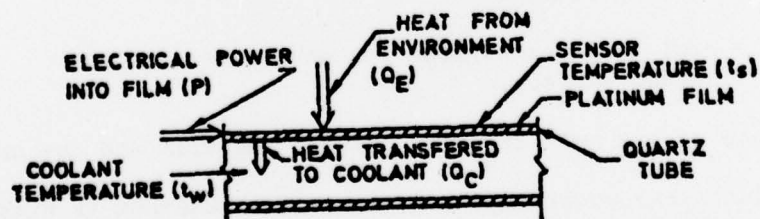Figure 1. Cooled Film Arrangement.



Figure 2. Heat Flow Schematic.

dissipation to the coolant is unaltered. In this way, the fluctuations in the bridge voltage are indicative of changes in the environmental conditions.

The cooled film sensor not only registers velocity fluctuations but also is sensitive to pressure and temperature fluctuations. Hence, the primary task is to relate the cooled film output to these fluctuations. This involves an empirical heat transfer relation by Ahmed[1]. This correlation is given by

$$N_{u_f} \left( \frac{\nu_e}{\nu_f} \right)^m = c + d \ (Re_f)^n \tag{3}$$

where $N_u$ is the Nusselt Number, $R_e$ is the Reynolds Number, $\nu$ is the kinematic viscosity, c, d, m & n are empirical constants and the subscripts e and f refer to environmental and film conditions. Writing Nusselt Numbers in terms of heat transfer rates and after substituting Eqs. (1) and (2) into Eq. (3), the resulting cooled film voltage fluctuations can be written as

$$\frac{E'}{\bar{E}} = A \ \frac{p'}{\bar{p}} + B \ \frac{u'}{\bar{u}} + C \ \frac{T'}{\bar{T}} \tag{4}$$

where A, B and C depend on the operating conditions for a typical case. In the present program, A = - 0.7 B = -0.7 and C = -4.79.

## Admittance Calculations

The admittance condition at the entrance to the nozzle, after averaging over cross-sectional area, is written as

$$\frac{1}{A_e} \int_{A_e} u dA + a_\omega p_o + b_\omega \sigma_\omega = 0 \tag{5}$$

where

$$u = \frac{u'_{o_\omega}}{\bar{c}} \ ; \quad p_o = \frac{p'_{o_\omega}}{\bar{p}_o} \ ; \quad \sigma_\omega = \frac{1}{A_e} \int_{A_e} t dA \ - \frac{\gamma-1}{\gamma} \frac{p_o}{\gamma} \tag{6}$$

$$t = \frac{t_\omega}{\bar{T}}$$

$A_e$ = cross sectional area

$a_\omega$, $b_\omega$ = Isentropic and Entropy admittance coefficients

The cooled film relation of Eq. (4), after a Fourier transform operation and area averaging, can be written as

$$R = \frac{1}{A_e} \int (A p_o + B u + C t) \, dA \tag{7}$$

Substitution of Eqs. (6) and (7) into Eq. (5) yields

$$R + \hat{a}_\omega p_o + \hat{b}_\omega J = 0 \tag{8}$$

where

$$\hat{a}_\omega = a_\omega B - b_\omega \frac{\gamma-1}{\gamma} B - A \tag{9}$$

$$\hat{b}_\omega = b_\omega B - C$$

and

$$J = \frac{1}{A_e} \int_{A_e} t dA$$

Equation (8) contains two unknowns $\hat{a}_\omega$ and $\hat{b}_\omega$. By performing cross spectral operations with any two of the quantities R, $p_o$ and J, two equations can be obtained for two unknowns. The equations used in the present

program are

$$S_{P_0 R} + \hat{a}_\omega S_{P_0 P_0} + \hat{b}_\omega S_{P_0 J} = 0$$

$$S_{JR} + \hat{a}_\omega S_{J P_0} + \hat{b}_\omega S_{JJ} = 0$$

(10)

where S refers to the cross spectral operation between the subscripted quantities. It is important to note that $S_{JR}$ and $S_{JJ}$, in Eq. (10), have been obtained after converting the single point measurements to an area averaged one, through the use of correlation area values. Equation (10) can be solved for $\hat{a}_\omega$ and $\hat{b}_\omega$ and the impedance coefficients $a_\omega$ and $b_\omega$ are then obtained through Eqs. (9).

## Results

The manufacturer's claims for this probe were shown to be totally false. From Eq. (4) and the stated A, B, and C coefficients it is seen that the probe acts best as a thermometer. Moreover, the combustor has extremely high temperature fluctuations so that a measurement was taken of a probe and a thermocouple placed very close to each other in the exhaust of the combustor. If the C values was indeed constant and the thermocouple was compensated, as it was, the transfer function between the two measurements should have been - 4.8. Shown in Fig. 3 is the transfer function. Clearly, a) even at low frequency the transfer function, while negative, is not large and b) serious frequency response starts at around 80 Hz.

Data reduction for the admittance coefficients was nevertheless attempted on a run with the admittance results of Fig. 4. The $b_\omega$ is
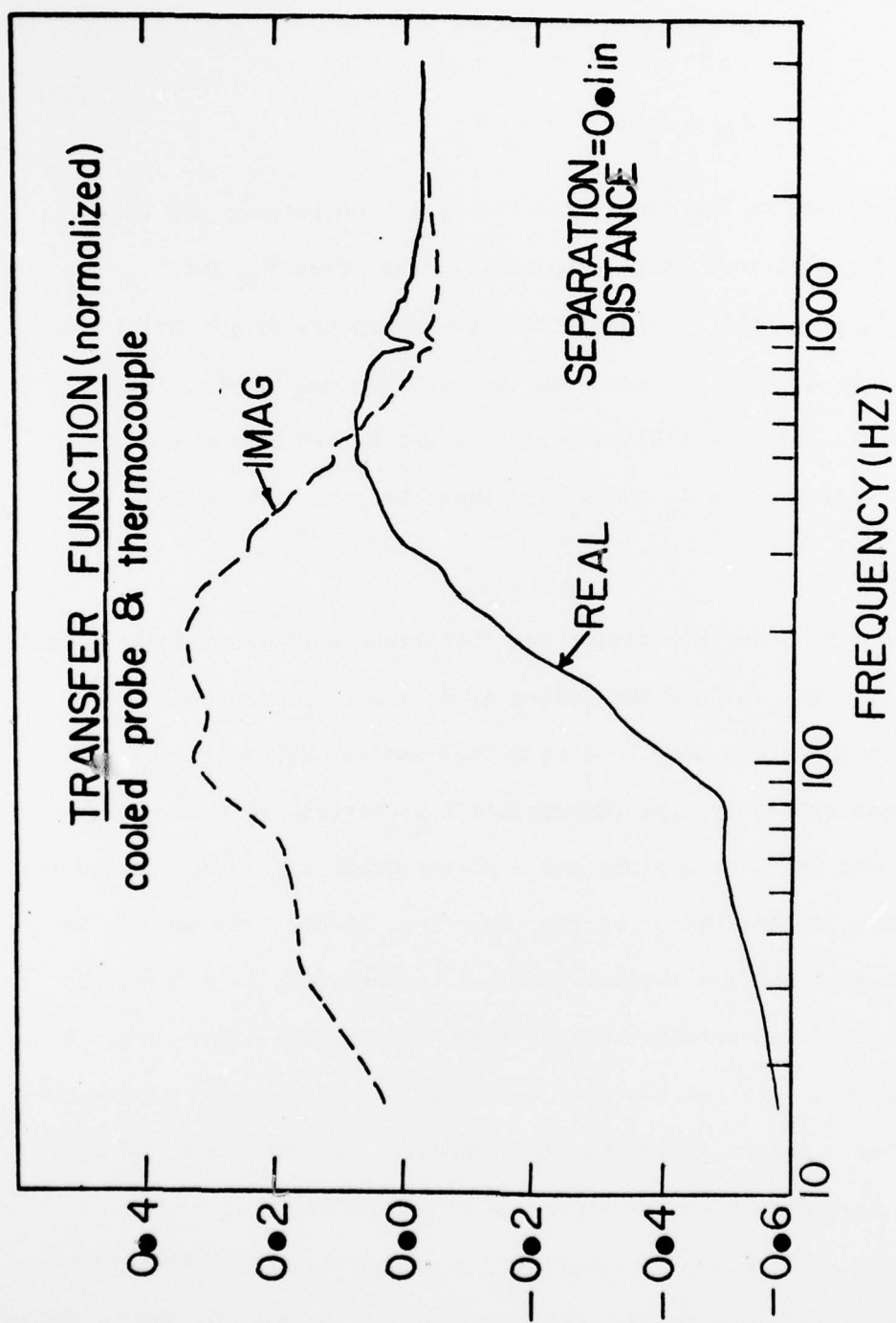
Figure 3. Transfer function between the cooled film probe and thermocouple.
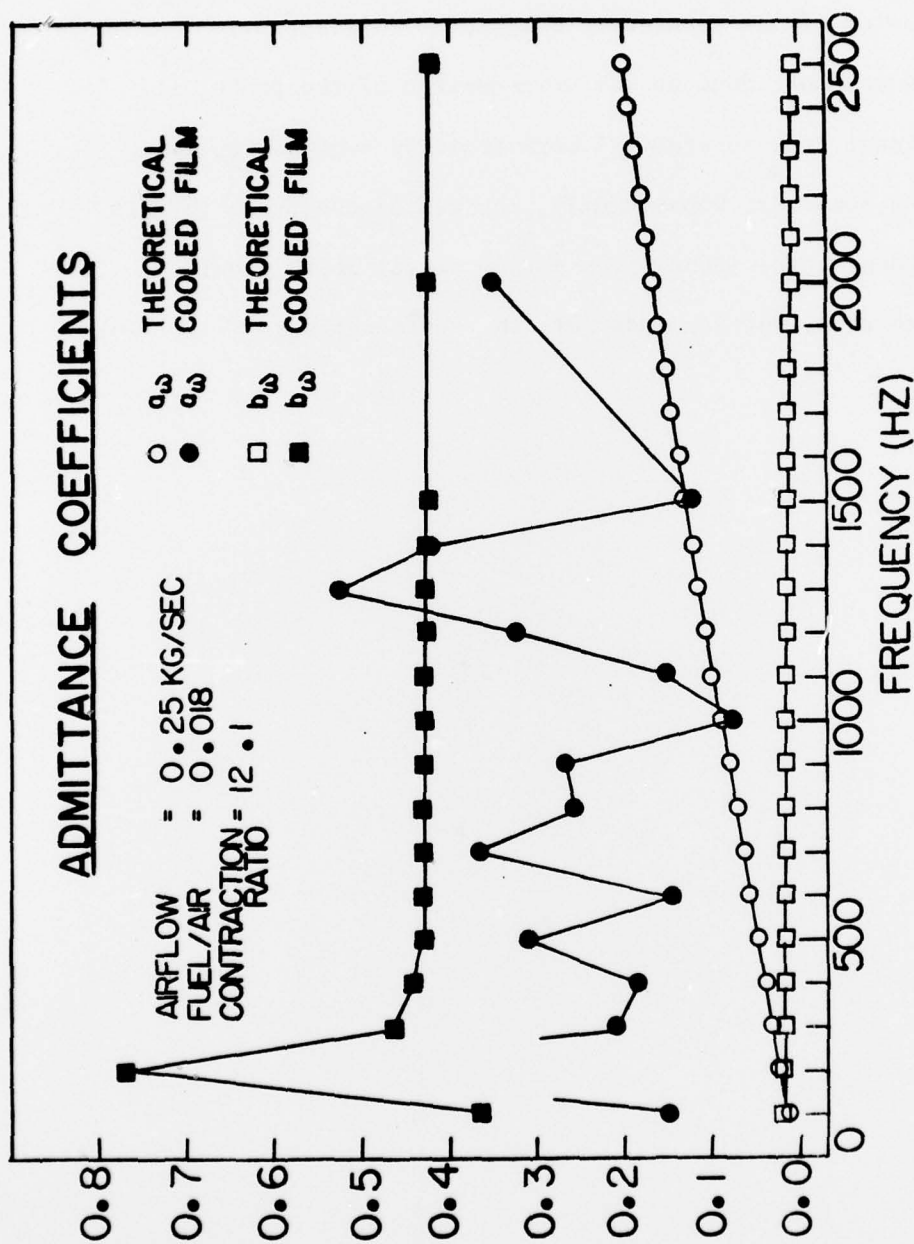
Figure 4. Admittance coefficients derived from the cooled film probe results compared with the theoretical results.

off by a factor of at least 10 when compared with theory and there is erratic behavior of the isentropic admittance coefficient.

While some work was done on the compensation of the probe, it soon become evident that substantial work would be required to fully characterize its behavior. Consequently, the use of the probe in this program was abandoned. The probe gives a good signal which should be useful in future work, but it needs full characterization.

References

1. Ahmed, A. M. "Forced Convection Heat Transfer to Cooled Cylinders at Low Reynolds Numbers and with Large Temperature Differences," McGill Merl TN 67-5, 1967.